Theses and Dissertations

Graduate School

2023

Synthesis and Application of Redox-Active Covalent Organic Frameworks in Rechargeable Batteries

Mohammad K. Shehab
Virginia Commonwealth University

Synthesis and Application of Redox-Active Covalent Organic Frameworks in Rechargeable Batteries

A dissertation submitted in partial fulfillment of the requirements for the degree of
Doctor of Philosophy at Virginia Commonwealth University

By

Mohammad K. Shehab

B.Sc., Yarmouk University, Irbid, Jordan, 2007

M.Sc., Yarmouk University, Irbid, Jordan, 2009

Director: Hani M. El-Kaderi

Professor, Department of Chemistry

Virginia Commonwealth University

Richmond, Virginia

May 2023

i

Acknowledgment

Firstly, I would like to express my deepest gratitude to my supervisor, Dr. Hani M. El-Kaderi, for his unwavering support, guidance, and encouragement throughout my Ph.D. journey. His expertise and invaluable insights have been instrumental in shaping the direction of my research and shaping the final outcome of this work. Dr. El-Kaderi has not been just an advisor and mentor but also a friend, a brother, and my role model. I could not have imagined having a better advisor and mentor for my Ph.D. study.

Besides my advisor, I would also like to extend my sincere thanks to the members of my thesis committee, Dr. Everett Carpenter, Dr. Xuewei Wang, and Dr. Ram Gupta, for their valuable feedback, suggestions and for providing me with the opportunity to learn from their wealth of knowledge. I am also thankful to Dr. Ram Gupta in the School of Chemical Engineering for the instrumental facilities provided. I wish to thank Dr. Carl Mayer and Dr. Dmitry Pestov for providing me with the proper instrumentation training to handle various characterization techniques during my research period.

I am deeply grateful to my former and current laboratory members of the El-Kaderi group for their support and encouragement, as well as for the stimulating and fun working environment they have provided.

I would also like to acknowledge the support of Dr. Maryanne Collinson, Dr. M. Sami El-Shall, and Dr. Julio Alvarez for guiding and working alongside the graduate students. I want to thank all the administrative staff, especially Rhea Miller, John Arnold, Michael Morris, and Edith Allin, for their help and willingness to assist me on various occasions.

Table of Contents

List of Figures

List of Tables

List of Schemes

List of Abbreviations

1D	One-Dimensional
2D	Two-Dimensional
3D	Three-Dimensional
AFM	Atomic Force Microscopy
ATR-IR	Attenuated Total Reflectance - Infrared
BILPs	Benzimidazole linked polymers
BET	Brunauer-Emmett-Teller
BJH	Barrett-Joyner-Halenda
COF	Covalent Organic Framework
COP	Covalent Organic Polymer
Cth	Theoretical Capacity
CV	Cyclic Voltammetry
DEGDME	Diethylene Glycol Dimethyl Ether
DMSO	Dimethylsulfoxide
EDLCs	Electrical Double-Layer Capacitors
EDS	Energy-Dispersive X-Ray Spectroscopy
ECs	Electrochemical capacitors
EESS	Electrochemical Energy Storage System
EIS	Electrochemical Impedance Spectroscopy
EV	Electric Vehicle
FWHM	Full Width at Half Maximum
GCD	Galvanostatic Charge Discharge
HKH	hexaketocyclohexane
HR-TEM	High Resolution Transmission Electron Microscopy
LIBs	Lithium-Ion Batteries
LSBs	Lithium Sulfur Batteries
MPCs	Metal porphyrin-based COFs
NLDFT	Non-Local Density Functional Theory
NMP	N-Methyl-2-pyrrolidone
NMR	Nuclear Magnetic Resonance
PI	Polyimide
PICs	Polyimide-based COFs
PI-Py-COP	Pyrene Polyimide Covalent Organic Polymer

PMDA	Pyromellitic Dianhydride
POP	Porous Organic Polymer
PSD	Pore Size Distribution
PVDF	Poly (vinylidene difluoride)
PXRD	Powder X-Ray Diffraction
Rct	Charge Transfer Resistance
Rel	Electrolyte Resistance
SEI	Solid Electrolyte Interface
SEM	Scanning Electron Microscopy
SIBs	Sodium-Ion Batteries
TAPE	1,1,2,2-Tetrakis(4-aminophenyl)ethene
TAPP	1,3,6,8-Tetra(4-aminophenyl)pyrene
TAB	1,2,4,5-Tetraaminobenzene
TBPy	1,3,6,8-Tetrabromopyrene
TGA	Thermal Gravimetric Analysis
TEM	Transmission Electron Microscopy
THF	Tetrahydrofuran
XPS	X-Ray Photoelectron Spectroscopy
Zw	Warberg Impedance

Abstract

SYNTHESIS AND APPLICATION OF REDOX-ACTIVE COVALENT ORGANIC FRAMEWORKS IN RECHARGEABLE BATTERIES

By: Mohammad K. Shehab

A dissertation submitted in partial fulfillment of the requirements for the degree of Doctor of Philosophy at Virginia Commonwealth University.

Virginia Commonwealth University, 2023

Director: Hani M. El-Kaderi, Professor, Department of Chemistry

The development of energy from non-renewable to renewable sources has been a significant trend in recent years. Non-renewable energy sources, such as fossil fuels, have long been the primary source of energy for human civilization. However, as the negative impacts of fossil fuel use on the environment and public health have become increasingly apparent, there has been a growing push to transition to renewable energy technologies. Rechargeable batteries are emerging during this transition and the main goal is to focus on exploring efficient, durable, and sustainable batteries for the energy storage application. Lithium-ion batteries (LIBs) are a type of rechargeable batteries that have become increasingly popular in recent years due to their high energy density, long cycle life, and low self-discharge rate. They are commonly used in a variety of applications, including portable electronics, electric vehicles, and renewable energy storage systems. However, LIBs manufacturing is expensive and falls short in sustainability due to the toxicity of the metal oxides used. Furthermore, lithium resources are limited and unequally distributed in the earth's crust.

On the other hand, some earth-abundant metals such as sodium, potassium, magnesium, and aluminum have been investigated as lithium alternatives in batteries. Among these options, rechargeable sodium-ion batteries (SIBs). The emergence of SIBs is driven by a need for more sustainable and cost-effective energy storage solutions. Unlike lithium, sodium is abundant and inexpensive, making it a more attractive option for large-scale energy storage applications such as electric vehicles and grid storage. Additionally, SIBs are also considered as a more environmentally friendly option as compared to LIBs.

SIBs have similar properties to LIBs, such as high energy density and long cycle life, but they still face some challenges such as the development of stable and efficient electrode materials. Despite these challenges, researchers are actively working on developing new materials and technologies to improve the performance and reduce the cost of SIBs.

One of the emerging concerns about commercial batteries is the use of the toxic inorganic metal oxide as a cathode to operate the battery which falls shorts in the sustainability. Therefore, organic materials are essential to address this issue since they are abundant, relatively inexpensive, and can be tailored to accommodate redox-active properties. Covalent organic frameworks (COFs) are made of organic materials, which makes them lightweight and easy to fabricate, and they also have a high thermal stability and mechanical strength. COFs are 2-dimentionals (2D) or 3-dimentionals (3D) extended organic frameworks in which the building units are connected with one another by strong covalent bonds. COFs can be very well candidate to replace the toxic inorganic metal oxide in metal-ion batteries due to high surface area and tunable pore size, which allows for efficient storage and transport of metal ions. Additionally, COFs can be tailored to accommodate redox-active properties.

The use of COFs in rechargeable batteries has the potential to address most of the monomeric organic salt in batteries such as the dissolution in the electrolyte, low surface area, low conductivity, and poor electrochemical performance. COFs have attracted attention in energy storage due to their crystalline polymeric frameworks for restraining dissolution in the electrolyte, π-conjugated skeletons for charge transport, and abundant uniform nanopores for ionic transportation.

This dissertation demonstrates the use of new crystalline COFs as an efficient cathode for rechargeable SIBs and discusses the energy storage mechanism and gives insights about the outstanding energy and power densities followed by research perspectives and future directions available for research. Our approach has the potential to make batteries more sustainable and less toxic. In addition to suitability and toxicity, the ability of the COFs' design to control the pore shape and size allows for the use of naturally abundant and cost-effective metals with comparable electrochemistry to lithium, such as sodium, potassium, and aluminum, which is essential to solving the scarcity problem of lithium. Our studies indicate that the ability to tailor COFs at the molecular level endows the battery with high power density, high specific capacity, and great gravimetric capacity because of the dense redox-active sites in the skeleton of COFs and the low molecular weight of the organic repeating units. We have successfully synthesized crystalline, porous Aza-COF, polyimide-based COF, and benzimidazole-linked polymers and investigated their potential in SIBs. Their crystallinity, porosity, and conductivity helped a rapid surface-controlled Faradic process, facile sodium ions diffusion into the bulk electrode, and the accessibility of abundant redox-active sites. Therefore, the aforementioned COFs showed outstanding electrochemical performance as electrode materials in LIB and SIBs, and

supercapacitors, making COFs a promising material for developing sustainable and efficient electrochemical energy storage devices.

Chapter 1. Introduction

1.1. Rechargeable Batteries

Nowadays, there is a tendency toward green, sustainable, and environmentally benign energy storage technologies owing to the depletion of natural resources and their negative impacts on climate change. The grid energy storage utilizes various technologies such as pump hydro, compressed air, fly wheel and electrochemical energy storage systems (EESS).[1,2] Rechargeable batteries, also known as secondary batteries, are a type of battery that can be recharged and used multiple times. They are designed to have a longer lifespan compared to primary batteries, which are designed to be used once and then discarded and are often more expensive. There are several types of rechargeable batteries, including nickel-cadmium (NiCad), nickel-Metal Hydride (NiMH), Lithium-ion (Li-ion), and Lithium Polymer (LiPo) batteries. Each type of rechargeable battery has its own unique set of properties, such as energy density, capacity, and self-discharge rate, and the choice of battery type depends on the specific requirements of the application. Among the various available energy storage systems in the market, rechargeable lithium-ion batteries (LIBs) still represent one of the most highly regarded electrochemical energy storage systems since their commercialization in the 1990s as they have been the dominant power source for portable electronic devices and electric vehicles due to their high energy density, long cycle life, and low self-discharge rate.[3] In LIBs, the traditional positive electrodes (cathodes) employed are mainly derived from metal-containing inorganic compounds composed of cobalt, iron, tin, or manganese ($LiCoO_2$, $LiMn_2O_4$, and $LiFePO_4$) coupled with graphite as the negative electrode (anode). The cathode operates based on reversible redox reactions that relay on the valence state changes of the transition metal component upon Li^+ insertion (e.g., Co^{3+}/Co^{4+})[4], while the anode functions by

accommodating electrons in π-bonds of graphite upon Li^+ intercalation between the graphitic layers (shown in Figure 1.1).[5]
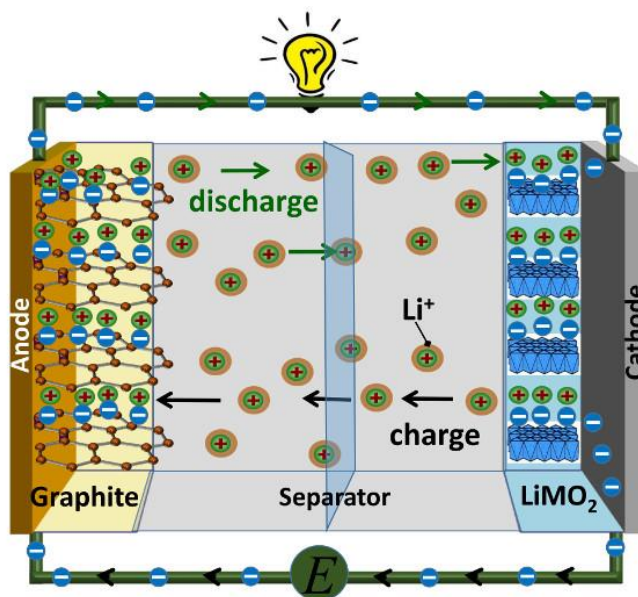
Figure 1.1 Schematic presentation of the commercial Lithium-ion Battery. Adapted from reference[6] with permission from © 2018 Multidisciplinary Digital Publishing Institute (MDPI).

However, rechargeable batteries made from active inorganic materials such as $LiCoO_2$ and $LiFePO_4$ can fall short of sustainability, metal extraction, battery disposal, and CO_2 emission. In fact, $72\,kg\,kW\,h^{-1}$ of CO_2 is emitted for the production of Li-ion batteries, materials, and recycling.[7]

1.2. Organic vs Inorganic electrodes

Unlike inorganic materials, organic materials have a lower environmental impact and greater safety as compared to inorganic metal oxide electrodes. Organic materials have such advantages like low cost, high natural abundance, environmentally friendly, low atomic weights of the elements which give rise to high gravimetric capacities.[8–15] Furthermore, because of their excellent structural flexibility and versatility, organic materials can be designed at the molecular level to afford multiple redox-active sites (N=N, C=O, and C=N), lower HOMO-LUMU gap, higher

2

surface area, uniform pore size, and high order π-conjugate aromatic frameworks, which qualify them to be utilized in the rechargeable batteries applications.[16,17] As a result, various organic materials have been tested as an electrode, including traditional conducting polymers[12], organic radical compounds[18], organic carbonyl compounds[19], organosulfur compounds[20], and organic carbon/nitrogen compounds including polymeric Schiff base[21], Azo compounds[22], indigo carmine[23], or pteridine.[24] However, dissolution in the organic electrolyte, low electronic conductivity, little redox stability, and many defects in the π-conjugated frameworks (amorphous) are the inherent problems of organic compounds.[25,26] To overcome these hurdles, it has been suggested that downsizing the active material to the nanoscale increases the electronic conductivity. Also, incorporating the conductive material to a backbone (C black) while using polymeric materials with extended π-conjugation can lower the solubility of the composite in the organic electrolyte. Finally, embedding redox-active sites with a crystalline porous conjugated framework could enhance the ion diffusion, ion mobility and thereby increase the electronic conductivity.[27,28]

1.2.1. Carbonyl (C=O) bond reaction

The carbonyl reaction is based on the reversible electrochemical reaction between lithium ions and carbonyl groups in a conjugated organic framework. Many classes of carbonyl compounds, including anhydrides, carboxylates, quinones, and imides, have been addressed. In order to achieve metal ion storage, all of these kinds of materials are redox-active at the carbonyl core (Figure 1.2).[29]

C₆O₆ — C_6O_6

TM

TT

656 mAhg⁻¹, 50 mAg⁻¹ — 656 mAhg^{-1}, 50 mAg^{-1}
100 cycles

122 mAhg⁻¹, 0.1 C — 122 mAhg^{-1}, 0.1 C
20 cycles

387 mAhg⁻¹, 0.1 C — 387 mAhg^{-1}, 0.1 C
20 cycles
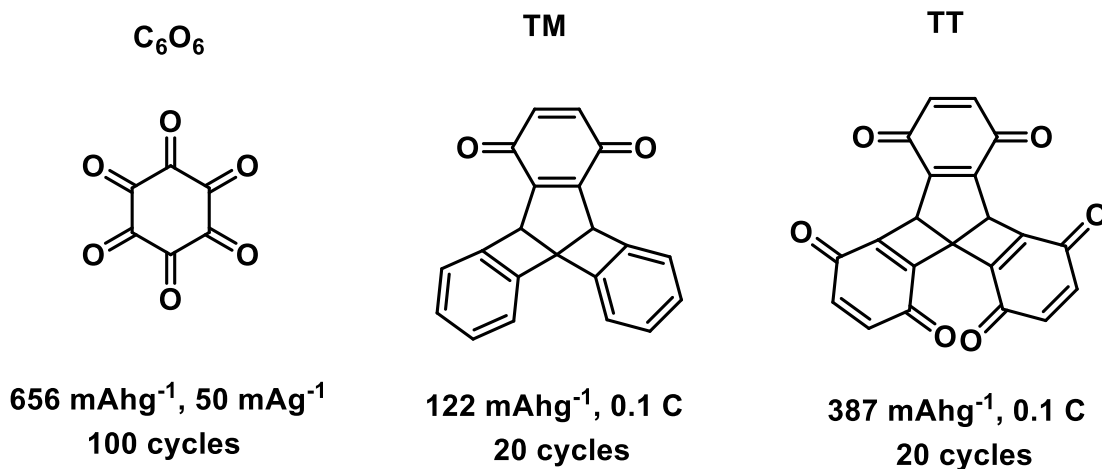
Figure 1.2 Structures of some carbonyl functionality studied for metal-ion batteries.[29] (TM) is triptycene mono-benzoquinone and (TT) is triptycene tribenzoquinone.

Anhydrides – are another type of carbonyl group in which electrons can interact with the carbonyl sites during the charge/discharge process. Most anhydrides investigated as electrodes are highly conjugated structures that facilitate charge transfer along the framework. In anhydride, charge storage can be distributed between the ion diffusion mechanism and surface redox reaction. (Figure 1.3)[30]
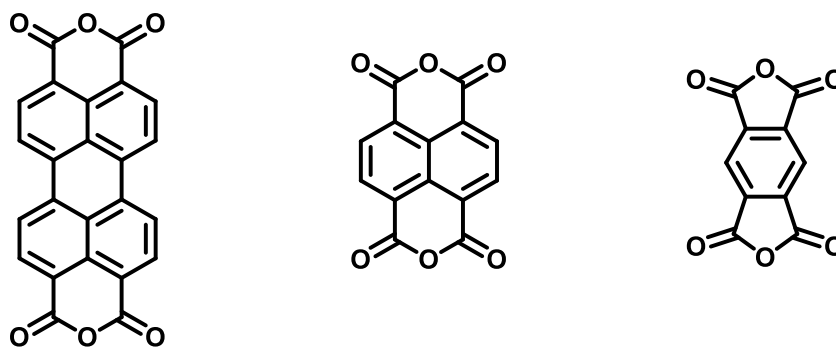
Figure 1.3 Structures of some anhydrides functionality studied for metal-ion batteries.[31–33]

Carboxylates – Carboxylate salts especially sodium and lithium have shown to be an effective anodic material in sodium-ion batteries (SIBs) and LIBs respectively because of the low reaction potential, high capacity, and facile structure tunability. Furthermore, the polarity of the carboxylate salt is essential to avoid the dissolution in the electrolyte. (Figure 1.4)[17]
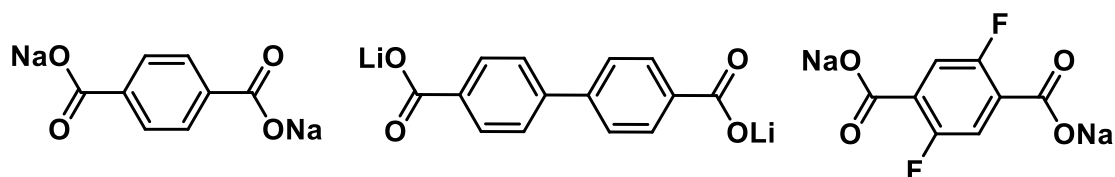
Figure 1.4 Structures of some carboxylates functionality studied for metal-ion batteries.[17]

Quinones – Quinones are a class of organic compounds that have been investigated for use in rechargeable batteries as active materials for both the positive electrode (cathode) and the negative electrode (anode). Quinones have high redox potentials and can participate in reversible oxidation-reduction reactions, which are desirable properties for battery-active materials. In cathodes, quinones have been shown to offer high energy density and good cycle stability, making them attractive for use in high-energy density batteries, such as LIBs.[34] In anodes, quinones have been shown to offer high capacity and good rate performance, making them attractive for use in fast-charging batteries. For example, hydroquinone has been reported as an anode material for LIBs with high capacity and good rate performance. (Figure 1.5)[35]
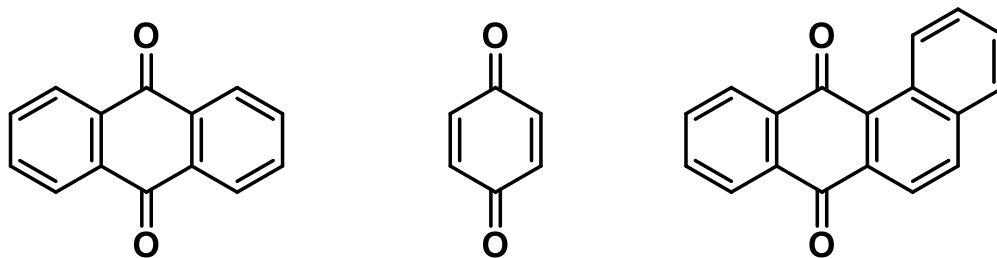
Figure 1.5 Structures of some quinones functionality studied for metal-ion batteries.

Imides – Imide refers to a class of organic compounds that contain a functional group (-NH-) derived from a carboxylic acid. On the other hand, polyimides are polymers made from imide monomers. Due to the high solubility in aprotic electrolytes, small imide compounds have not proven successful in metal ion batteries. As a result, it is found that the prolonged π-conjugations in these structures work well to increase the H-bonding contacts while reducing the solubility. Besides being utilized as an electrode active materials, polyimides are used Also as separators between the anode and cathode to prevent short circuits.[36] They are known for their excellent chemical stability, high thermal stability, and high mechanical strength. These properties make polyimides ideal for use in high-temperature applications.[37,38] (Figure 1.6)
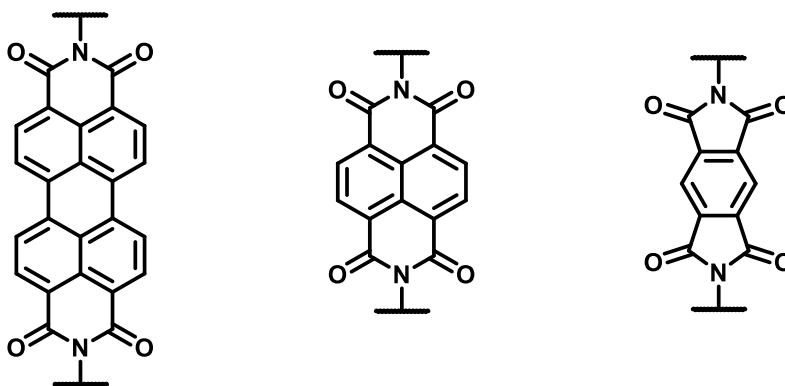
Figure 1.6 Structures of some polyimide functionality studied for metal-ion batteries.

6

1.2.2. C=N bond reaction

Organic materials containing the C=N functional group have been explored as potential materials for use in batteries, particularly as electrode materials in LIBs. The C=N bond can contribute to forming a stable and conductive network in the polymer, which is important for its performance as an electrode material. The organic electrodes containing C=N bond reactions encompass Schiff bases and pteridine compounds.

Schiff bases – Schiff bases are a vast group of compounds characterized by the presence of a double bond linking carbon and nitrogen atoms, Schiff bases consist of a standard conjugated repeat unit of –N=CH–Ar–HC=N–, where Ar refers to an aromatic moiety.[21] amongst the synthesis methods of Schiff bases, the simple condensation reaction from aldehydes and amines is the preferred as it releases water as a byproduct.[39] Several Schiff bases have been successfully realized as anode materials for SIBs. (Scheme 1.1)
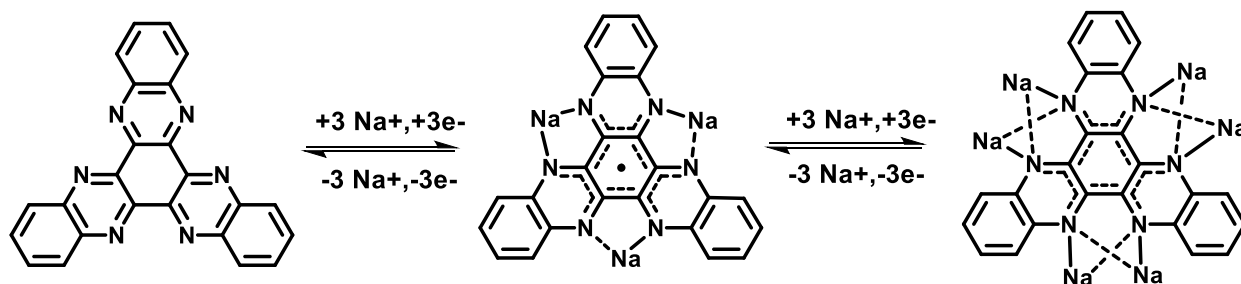
Scheme 1.1 Sodium charge/discharge mechanism of a Schiff base studied for SIBs.[39,40]

Pteridine derivatives – Pteridines are a class of organic compounds that contain a pteridine ring, which is a nitrogen-containing heterocyclic ring composed of four pyridine-like nitrogen atoms. The presence of C=N bond in the ring give them potential to be used as electrodes. (Scheme 1.2)[24]
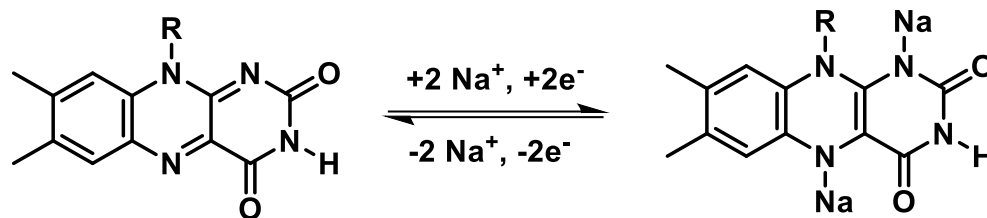
Scheme 1.2 Sodium charge/discharge mechanism of a pteridine derivative studied for SIBs.[24]

1.2.3. Azo (N=N) bond reaction

Azo bond (N=N) reaction is the latest evolving redox active site introduced and studied for LIBs and SIBs. The azo group in the aromatic azo compound, the double bond in the azo group is converted to a single bond during the sodiation process, and the single bond is converted back to the double bond during the desodiation process. Each nitrogen atom reacts with one Na-ion and one electron during the sodiation/desodiation process. This reversible process enables the electrochemical activity of azo compound in SIBs.[22] (Scheme 1.3)
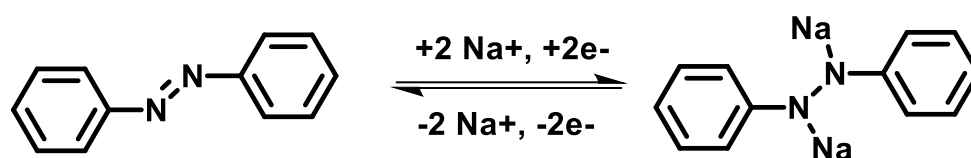
Scheme 1.3 Sodium charge/discharge mechanism of an azo compound studied for SIBs.[22]

Table 1.1 Comparison of the sodium-storage performance of different organic materials as SIB electrodes. (AM = active material)

Organic Material	Rate (Ag⁻¹)	Sp. Capacity (mA h g⁻¹)	Capacity retention (current density, cycles)	Notes	AM : C : binder (binder)	Ref
Na-PBQS	0.05	268	68% (0.05 A g⁻¹, 100)	Quinone based polymer	6:3:1 (PTFE)	41
PTPAn	0.05	98	97% (0.5 A g⁻¹, 200)	Polytriphenylamine	6:3:1 (PTFE)	42
	2	88				

Name	Rate	Capacity	Retention	Description	Ratio	Ref
PAQS	0.18	220	185 mA h g-1 (1.6 A g^{-1}, 200)	Poly(anthraquinonylsulfide)	4:5:1 (PTFE)	42
	6	160				
PPy/FC	0.05	135	85% (0.05 A g^{-1}, 100)	Polypyrrole based	8:1:1 (PTFE)	43
	1.6	75				
PI-2	0.05	137	92.7% (0.025 A g^{-1}, 400)	PTCDA based polymer	6:3:1 (PVDF)	44
	10	50				
HA/Na	0.02	208	80% (0.04 A g^{-1}, 200)	Humic acid polymer	85:10:5 (PTFE)	45
	0.4	40				
P(AN-NA)	0.05	195	89% (0.05 A g^{-1}, 50)	Copolymer, C fibre as conducting agent	7:1:1:1 (PTFE)	46
	0.2	165				
Ppy/DS	0.05	115	82% (0.05 A g^{-1}, 50)	Polypyrrole based	8:1:1 (PTFE)	47
	0.8	85				
Amorphous OPr	0.02	96	66% (0.02 A g^{-1}, 50)	Oligopyrene based	8:1:1 (PVDF)	48
	0.5	10				
PDS	0.05	99	70% (0.05 A g^{-1}, 100)	Poly(diphenylaminesulfonic acid sodium), C fibre + C black as conducting agent	5:4:1 (PTFE)	49
	0.4	43				
PI	0.1	126	90% (0.1 A g^{-1}, 50)	PTCDA-based	6:3:1 (PVDF)	50
	0.8	90				
PI	0.05	184	83% (0.05 A g^{-1}, 20)	NTCDA-derived	6:3:1 (PTFE)	37
	0.1	71				
PNTCDA	0.14	140	90% (0.07 A g^{-1}, 500)	NTCDA-derived polyimide	3:5:2 (PVDF)	51
	2.52	84				
PNFE	0.1	134	91.2% (1 A g^{-1}, 1000)	NTCDA derived PI	6:3:1 (PTFE)	52
	1.8	95				
PNTCDA	1	138	70% (1 A g^{-1}, 50000)	NTCDA derived PI	6:3:1 (PTFE)	53
	100	28				
PNP@CNT	0.1	125	88% (1 A g^{-1}, 500)	NTCDA derived PI	6:3:1 (PTFE)	54
	2	92				
PI	0.05	122	70% (0.05 A g^{-1}, 100)	Sulfonyl based PI	6:3:1 (PVDF)	55
P11	0.05	165	92% (0.05 A g^{-1}, 150)	Anthraquinone-based polyimide	4:4:2 (PVDF)	56
PI2	0.05	192	95% (0.05 A g^{-1}, 150)	Anthraquinone-based polyimide	4:4:2 (PVDF)	56
PAQI	0.05	197	93% (0.05 A g^{-1}, 150)	Poly(anthraquinonyl imide)	4:4:1 (PVDF)	38
	1	65				
PI-1	0.5	176	83.1% (5 A g^{-1}, 1000)	Polyimide-based	5:3:2 (PVDF)	57
	5	102				
PI-2	0.5	95	62.4% (5 A g^{-1}, 1000)	Polyimide-based	5:3:2 (PVDF)	57
	5	69.4				
PBT	0.04	500		Polybithiophene based, C nanofibre as conducting agent	2:1	58
PTMA	0.1 C	206	92% (0.5 C, 100)	CNT encapsulated PTMA, CNT as conducting agent	63:30:7 (PVDF)	59
	5 C	190				
O5-Na	0.013	240	97.5% (0.03 A g^{-1}, 25)	Oligomeric Schiff bases	8:2	60
	1.3	50				
P3	0.026	190	53% (0.026 A g^{-1}, 25)	Polymeric Schiff bases	1:1	21

BPOE	0.01	200	80% (1 A g^{-1}, 7000)	Bipolar organic porous framework	7:2:1 (CMC)	[61]
	5	50				
PDCzBT	0.02	145	119 mA h g^{-1}, (0.05 A g^{-1}, 200)	Conjugated microporous polymer	6:3:1 (PTFE)	[62]
	0.1	99				
BPPF	0.1	38		Bipolar organic porous framework	7:2:1 (CMC)	[63]
	2	22				
o-PDA	0.1	433	100% (0.05 A g^{-1}, 1024)	Polydopamine derived	8:2 (no binder)	[64]
	3.2	122				
PANS	0.05	133	96.7% (0.1 A g^{-1}, 200)	Sulfonated polyaniline	8:1:1 (PTFE)	[65]
	0.08	76				
PAQS/P(AN-NA)	0.05	160	80% (0.05 A g^{-1}, 50)	All organic battery	7:2:1 (P(AN-NA)) 4:5:1 PAQS (PTFE)	[66]
	0.8	120				
Ppy	0.02	100	78.5% (0.4 A g^{-1}, 1000)	Polypyrrole nanospheres	8:1:1 (PVDF)	[67]
	0.32	69				
s-Ppy	0.2	188	65% (1.8 A g^{-1}, 500)	Submicron polypyrrole	7:2:1 (PVDF)	[68]

1.3. Covalent Organic Frameworks (COFs)

Covalent organic framework (COFs) are two-dimensional or three-dimensional crystalline porous organic polymers with extended structures in which building blocks are linked by strong covalent bonds in repeating units forms.[69] COFs can be structurally predesigned, synthetically controlled, and functionally managed distinguishes them from other polymers. The polycondensation processes offer synthetic techniques to build the predesigned primary and high-order structures, and the topological design diagram provides geometric guidance for the structural tiling of extended porous polygons (Figure 1.7).[70] COFs have attracted attention in energy storage due to their crystalline polymeric frameworks for restraining dissolution in the electrolyte, π-conjugated skeletons for charge transport, and abundant uniform nanopores for ionic transportation.[71,72] Due to their structural diversity, uniform porosity, thermal stability, and smart structural assembly, COFs have been used extensively in different areas such as gas separation[73,74], drug delivery[75], catalysis[76], pseudocapacitors[77,78], proton conduction[79], and energy storages[80–82] in the past decade.

In the field of batteries, COFs were integrated as a cathode with lithium for LIBs. LIBs are considered the dominant power supply for portable electronics, electric vehicles, and grid-scale energy-storage systems because of the high energy density and stable cycling performance.[83] However, the cost and the uneven distribution geographically of lithium resources make it crucial to look for alternatives to replace lithium as an anode.[84,85] Since redox-active organic materials have their ability to undergo reactions with different metals, some earth-abundant metals such as sodium (SIBs)[19,80,81], potassium (PIBs)[86], magnesium (MIBs)[87], aluminum (AlIBs)[88] can be potential alternatives for lithium. For instance, a very recent study by Wang et al. demonstrated the use of a pyrazine-functionalized polymer in Na^+, $Mg^{2+,}$ and Al^{3+} batteries which exhibit remarkable stability during cycling even at high C-rates (50,000 cycles at 25 C).[89] Rechargeable SIBs have attracted considerable attention for large scale electrical energy storage and smart grid, owing to the abundance, low cost of Na sources, and comparable performance with LIBs.
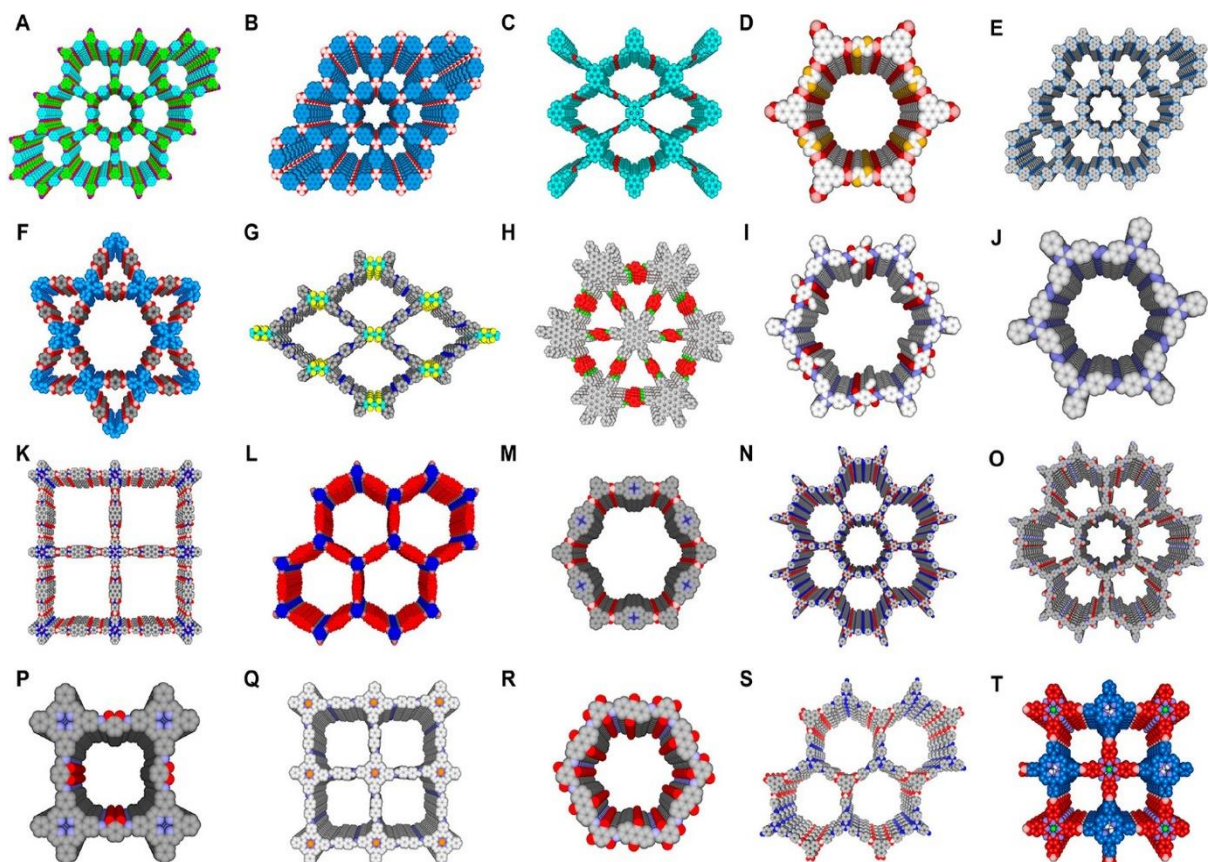
Figure 1.7 Examples of 2D COFs with layered stacking structure. Adapted from reference[90] with permission from © 2020 American Chemical Society.

1.3.1. Benzimidazole linked polymers (BILPs)

BILPs are extended heterocyclic aromatic organic compound polymers that contain benzimidazole (BI) groups as crosslinking units. El-Kaderi pioneered the synthesis of porous benzimidazole-linked polymers (BILPs), which form highly cross-linked frameworks through imidazole ring formation upon condensation reactions between aryl aldehydes and diamine-functionalized building blocks.[91] More recently, there were a few successful attempts to crystallized BILPs using polyphosphoric acid or by Debus–Radziszewski multicomponent reactions.[92–94] BILPs exhibit a micro and mesoporous nature and high surface area with high chemical stability. Besides, the presence of the sp^2 and sp^3 N sites makes BILPs great for gas storage and separation. On the other hand, deprotonating the N-H hydrogen to form the ionic BILP (IBILP) delocalizes the negative

12

charge on the imidazole ring and makes the entire network conjugated for fast charge transport. Also, the negative charge can be used as a nucleophile for SN^2 reaction for pores functionalization.[92] For instance, BILP-based hexamine (Aza-BILP, Figure 1.8) is an excellent candidate for metal ion batteries, and it can be synthesized by a condensation of aryl-hexamine monomers and terephthalaldehyde to afford a decorated nine aza bonds (-N=C-) undergo reversible redox reactions which is essential for the metal ion interaction with the active sites. Based on materials modeling studies, Aza-BILP has a pore diameter of 33 Å and in the field of energy storage, bigger pore size means bigger channels for the metal ions to pass through and thereby higher ion mobility rate for more power density. Furthermore, bigger pores endow a chance for bigger metal ions to be utilized, such as Na^+ and K^+. On the other hand, incorporating more redox-active sites increases the theoretical specific capacity. The synthesis of different BILPs and their applications in the field of gas capture and storage were reported in the literature.[74]
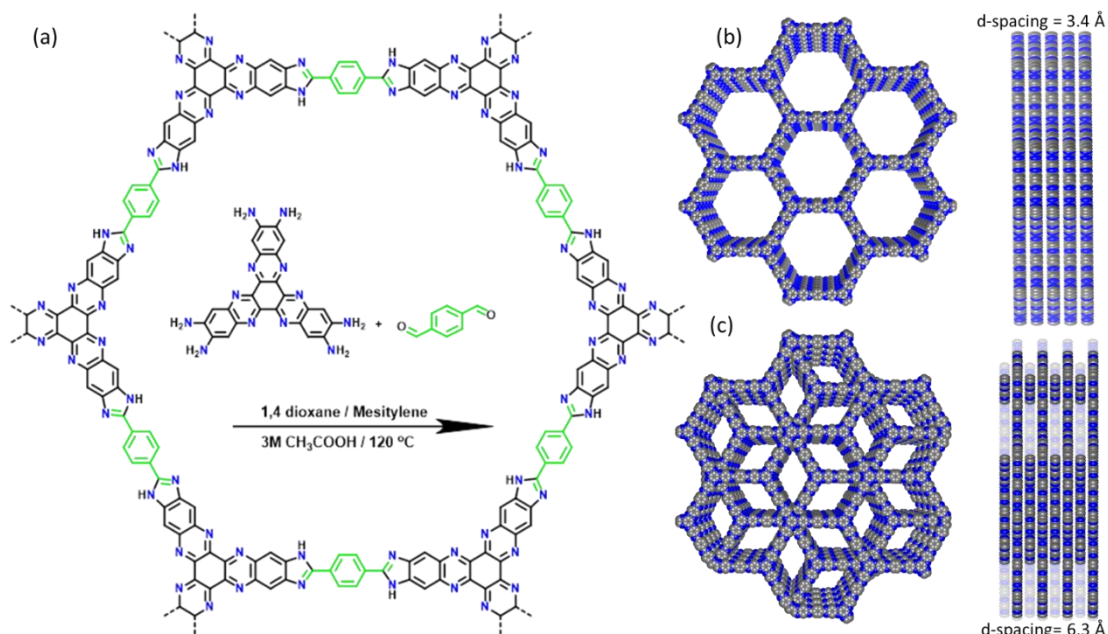
Figure 1.8 Aza-BILP (a) the chemical reaction scheme (b) the modeled Aza-BILP with AA stacking front and side view with interlayer spacing distance of 3.4 Å(c) the modeled Aza-BILP with AB stacking front and side view with interlayer spacing distance of 6.3 Å.

13

1.3.2. Polyimide-based COFs (PICs)

Polyimide linked polymers are a type of covalent organic framework containing imide group in the framework repeating unit. PICs which are known for high thermal stability, excellent mechanical properties, and good chemical resistance and are utilized widely in the semiconductor and electronics industry.[95] The most widely used procedure for polyimide synthesis is a two-step poly(amic acid) process. This involves reacting a dianhydride and a diamine at ambient conditions in a mixture of solvents (i.e. NMP, mesitylene) and isoquinoline catalyst to yield the poly(amic acid) intermediate, which is followed by the thermal cyclization at high temperature to produce the final polyimide.[75,95] However, this approach lead to amorphous materials and a lack of crystallinity. To enhance the crystallinity of the PCs, post synthetic linker exchange was recently used by linker exchange approach using an imine-linked COF as a template.[30] (Figure 1.9)
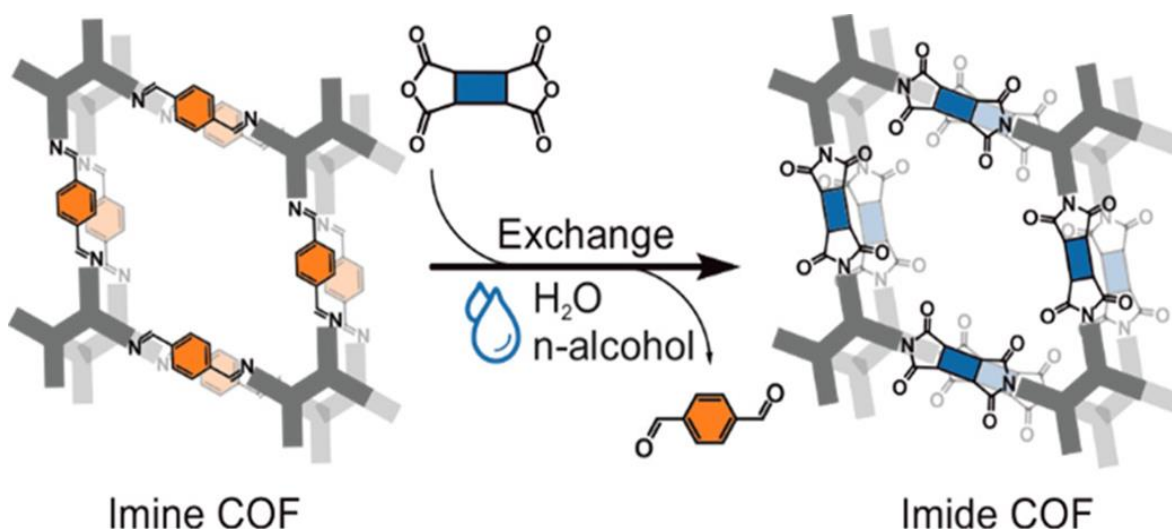
Figure 1.9 The synthesis of polyimide based COFs using post synthetic linker exchange approach, Adapted from reference[96] with permission from © 2022 American Chemical Society.

1.3.3. Metal porphyrin-based COFs (MPCs)

Porphyrin-based covalent organic frameworks (COFs) (Figure 1.10) are a subclass of porous materials made up of organic building blocks that have porphyrin units that are covalently linked together. Organic compounds called porphyrins have a core metal atom mainly cobalt or nickel and are made up of four pyrrole rings joined by methine bridges. Besides the porosity and the highly ordered frameworks which can be afforded by COFs, the metal presence in the core of porphyrin-based COFs endow extra advantages for enhancing the catalytic activity. For instance, cobalt porphyrin-based COFs was used for catalytic carbon dioxide reduction in water.[97]
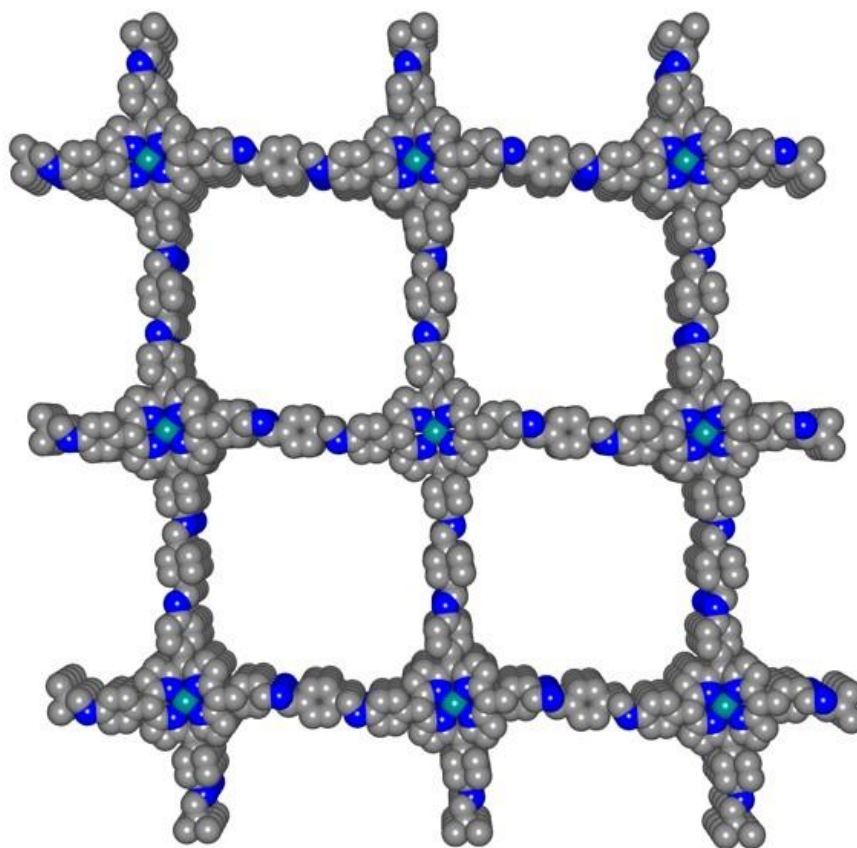
Figure 1.10 Cobalt porphyrin-based COF where gray is carbon, blue is Nitrogen and green is cobalt. (Hydrogens were removed for clarity). Adapted from reference[97] with permission from © 2015 Science.

1.4. Electrochemical energy storage

1.4.1. Metal-ion batteries

Metal-ion batteries are a type of rechargeable battery that use the movement of metal ions, typically lithium, between the anode and cathode to produce an electrical current. The anode is typically made of graphite, while the cathode is made of metal-containing materials like metal oxides. Metal-ion batteries are a versatile and widely used type of rechargeable battery, offering high energy density and low self-discharge rates. They are used in a variety of applications, from portable electronic devices to electric vehicles and backup power supplies. Examples of metal ion batteries include the LIBs, SIBs, the nickel-metal hydride battery, and the zinc-air battery. To date, LIBs offer the largest energy density and longest life among all rechargeable battery technologies owing to the versatile chemistry and research being carried out on both anodic and cathodic materials.[83] However, the cost and the uneven distribution geographically of lithium resources make it crucial to look for alternatives to replace lithium as an anode.[84,85] Rechargeable SIBs have attracted considerable attention for large scale electrical energy storage and smart grid, owing to the abundance, low cost of Na, and comparable performance with LIBs. However, the larger ionic radius of Na^+ ions make the intercalative storage of ions in graphite difficult (Table 1.2). As a result, the use of non-graphitic material such as meso-carbon or hard carbon has evolved to be promising alternative anodic materials for SIBs.[98]

Table 1.2 Characteristics of Li versus Na.[99]

	Li	Na
Atomic weight	6.9 g mol^{-1}	23 g mol^{-1}
Ionic radius	76 pm	102 pm
Melting point	180.5 °C	97.8 °C
E° vs SHE	-3.0 V	-2.7 V
Abundance	20 mg kg^{-1}	23.6 x 10^3 mg kg^{-1}
Price, carbonates	~$5000 per ton	~$150 per ton
Distribution	70% in South America	Everywhere

The working principle of metal ion batteries is based on the ion and electron movements between the cathode and the anode. Organic composite can be utilized as a cathode, which serves as a working electrode. During discharging (Figure 1.11 a), M$^+$ ions are extracted from the anode, moved through a microporous membrane by the electrolyte and inserted into the cathode while the electrons travel through the external circuit; the membrane is a permeable separator to ions during charge/discharge process and serves as a physical barrier between the anode and the cathode to avoid short-circuiting. On the other hand, during charging (Figure 1.11 b), the reverse process occurs where the M$^+$ ions are being extracted from the cathode and re-inserted in the anode with the electrons moving through the external circuit. Ideally, the anode and cathode materials should be able to withstand repeated cycles of sodium storage without degradation.[11]
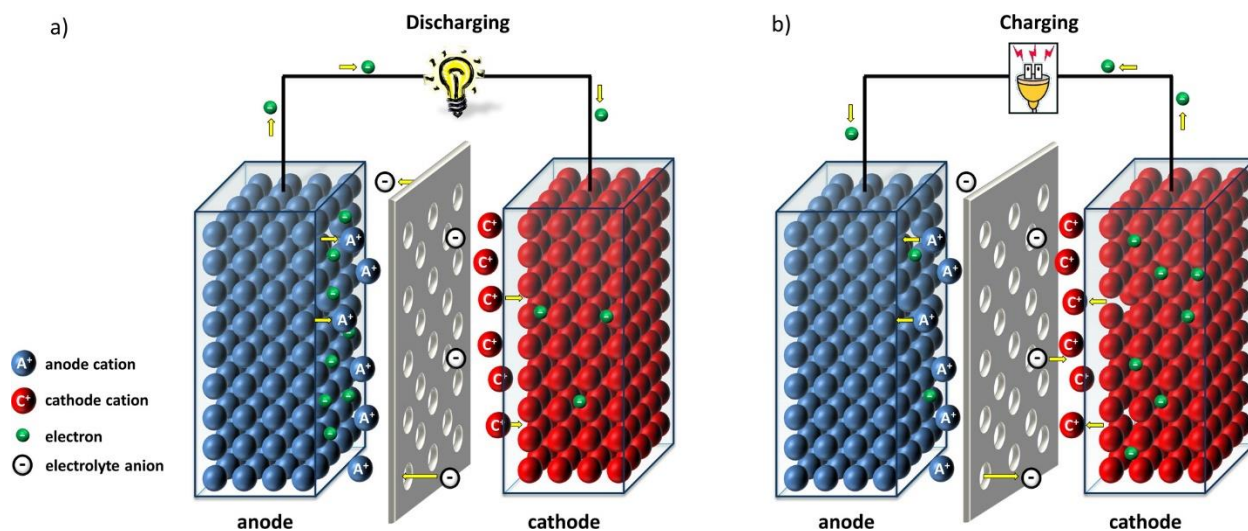
Figure 1.11 Schematic representation of the (a) discharging and (b) charging process of a metal-based secondary battery (rechargeable batteries). Adapted from reference[11] with permission from © 2016 American Chemical Society.

1.4.2. Lithium-sulfur batteries (LSBs)

Another approach of using metals (Li and Na) in batteries is their use in lithium-sulfur and sodium sulfur batteries. Lithium-sulfur batteries are a type of rechargeable battery that use lithium as the anode (negative electrode) and sulfur as the cathode (positive electrode) in the battery (Figure 1.12). One of the main advantages of lithium-sulfur batteries is their high theoretical energy density (2567 W h kg^{-1}). That is because of the high energy storage capacity of sulfur, which is a lightweight and abundant element. Another advantage of lithium-sulfur batteries is their low cost. Sulfur is abundant and relatively cheap, compared to other materials used in batteries, such as cobalt or nickel. This makes lithium-sulfur batteries a potentially cost-effective option for large-scale energy storage systems. Lithium-sulfur batteries also have a low environmental impact, as sulfur is non-toxic and can be easily recycled. Additionally, the production of lithium-sulfur batteries generates fewer greenhouse gas emissions compared to other types of batteries.
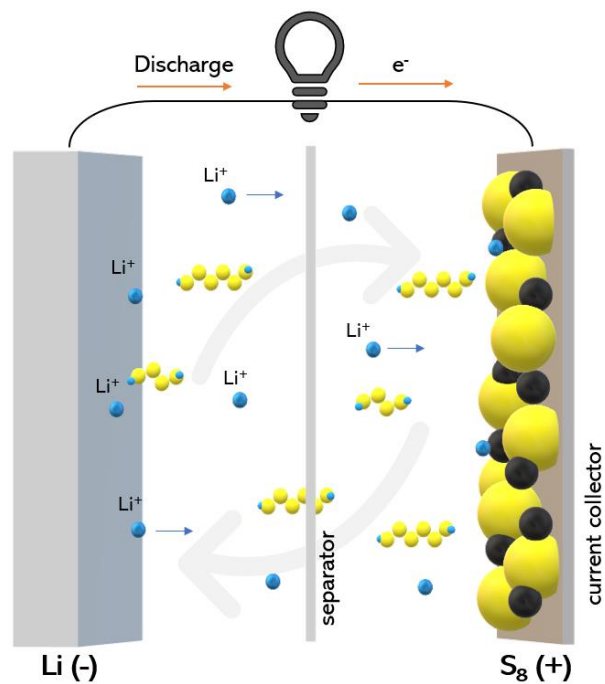
Figure 1.12 A typical lithium-sulfur battery with a lithium as anode and sulfur as a cathode.

Despite their advantages, lithium-sulfur batteries have some challenges that need to be overcome before they can be widely commercialized. One of the main challenges is the phenomenon of shuttle effect results from the dissolution of the soluble polysulfide in the electrolyte which can shuttle between the electrodes during the charge−discharge process in what is called the "sulfur shuttle mechanism", which hampers the battery cyclability.[100] Furthermore, other LSBs challenges should be kept in consideration such as volumetric expansion, growth of lithium dendrites, and side reaction between lithium and the electrolyte which generates gaseous byproduct[101] (Figure 1.13).
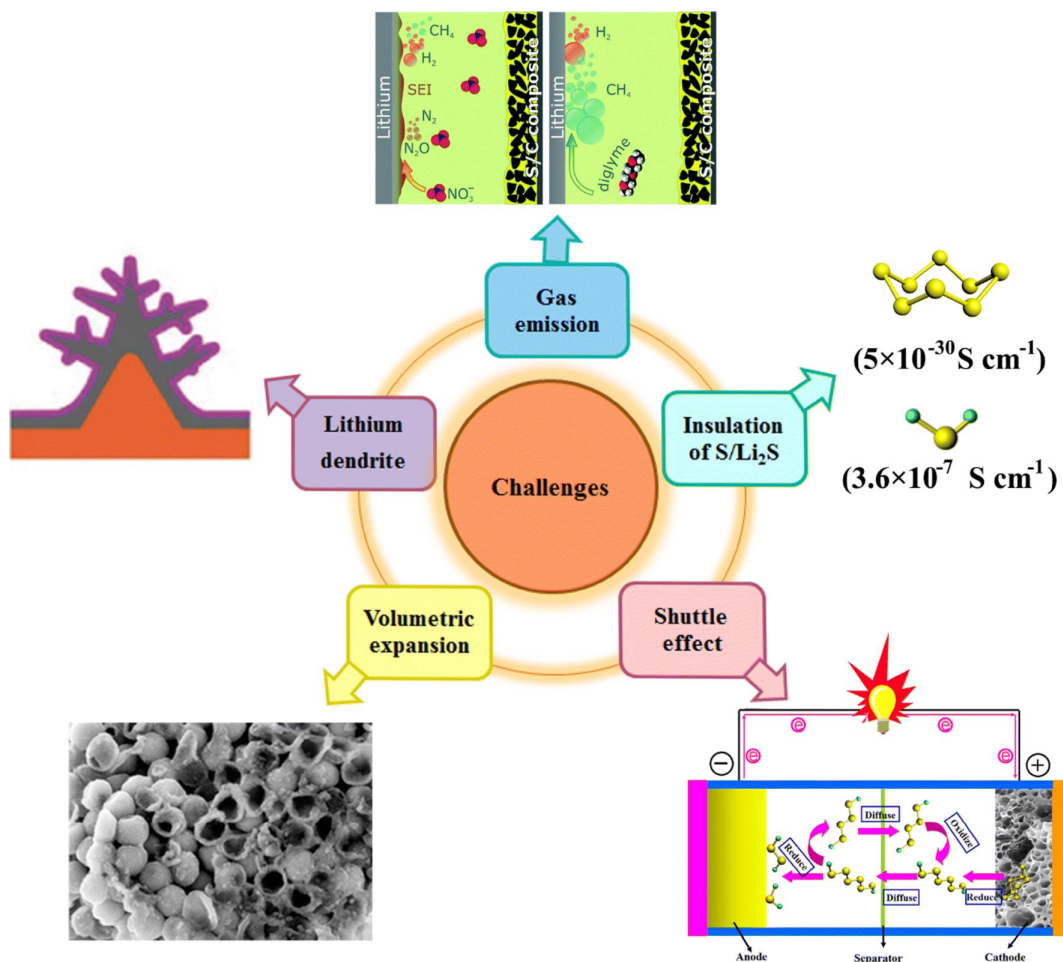
Figure 1.13 The challenges of the modern LSBs. Adapted from reference[101] with permission from © 2018 Springer.

1.4.3. Electrochemical capacitors (ECs)

ECs, also known as supercapacitors, represent an important class of energy-storage systems because they offer attractive parameters, such as high-power density, fast charge/ discharge capacities and excellent cycling lives that exceed tens of thousands of cycles.[102] According to their energy storage mechanism, supercapacitors can be classified as electrical double-layer capacitors (EDLCs) and pseudocapacitors. EDLCs store energy based on non-Faradic charge accumulation along the double layer formed at the electrode-electrolyte interface. Therefore, higher surface area materials are required to accumulate more charges on the electrical double layer (EDL) and,

thereby, more energy storage. On the other hand, pseudocapacitive materials can store charge in either Faradaic electron transfer, by accessing two or more redox sites of the electrode materials or via non-Faradaic charge storage in the EDL present at the surfaces of these materials. Energy storage involving pseudocapacitance occupies a middle stage between EDLCs that store energy in the double-layer on a high surface area conductor and batteries, which depend predominantly on Faradaic electron transfer to redox site centers.[103,39] (Figure 1.14)
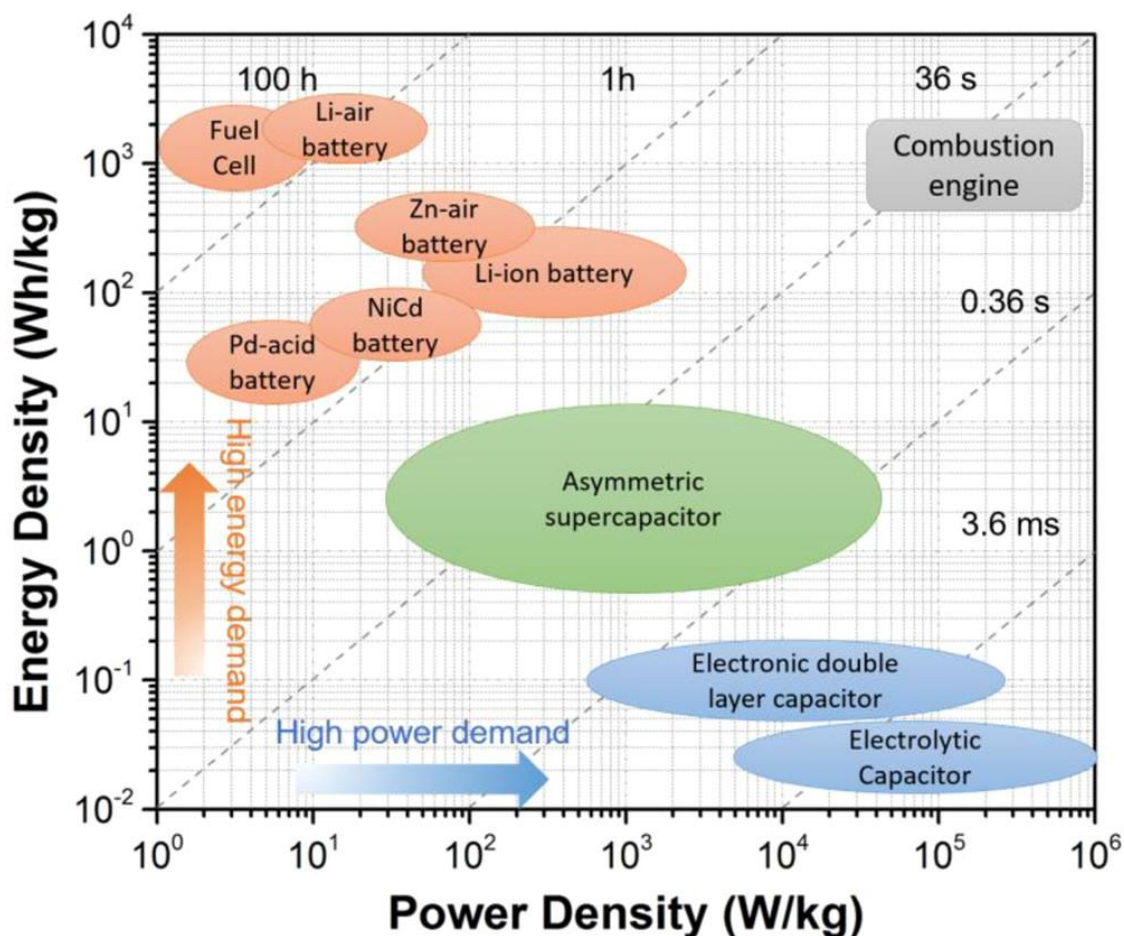
Figure 1.14 Ragone plot illustrating the performances of specific power vs specific energy for different electrical energy-storage technologies. Times shown in the plot are the discharge time, obtained by dividing the energy density by the power density. Adapted from reference[104] with permission from © 2018 American Chemical Society.

1.4.4. Energy storage mechanism

Energy storage mechanism information can be obtained by running cyclic voltammetry (CV) measurements at different sweep rates (v). In general, increasing the sweep rate magnifies the current peak (i) and broadens cyclic voltammogram as described in the equation below. However, the reversibility of the redox peaks still existed.

$$i_p = av^b$$

For the diffusion-controlled process, the peak current varies as $v^{0.5}$ (b = 0.5), which is the battery-like behaving process. However, for the surface-limiting redox, the peak current varies directly as v (b = 1), which is a capacitive-like behaving process.[103] when b is a middle area between 0.5 and 1, the pseudocapacitive behavior is dominated for a fast surface-controlled Faradic process.[105] Several cyclic voltammograms at different sweep rates were used to calculate the b-values at the current maxima in the anodic and cathodic systems. (Figure 1.15)
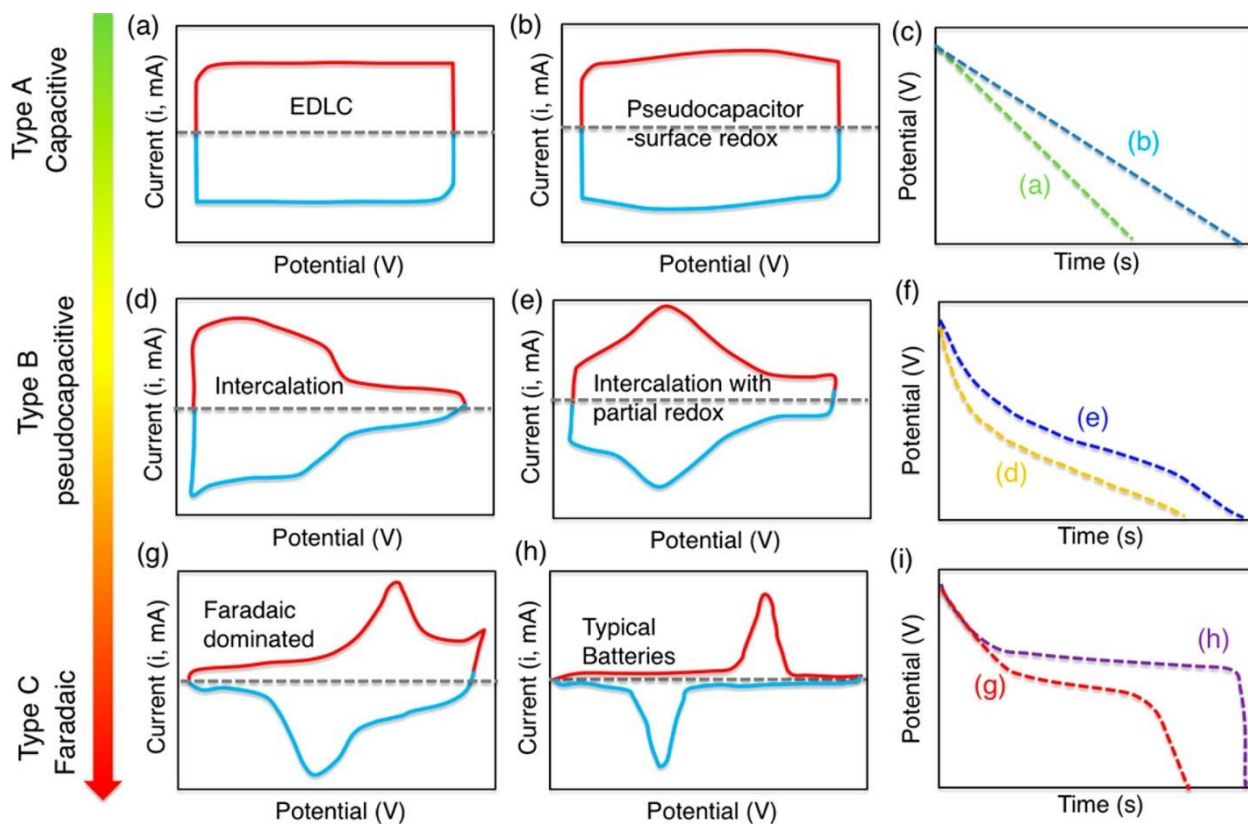
Figure 1.15 (a, b, d, e, g, h) Schematic cyclic voltammograms and (c, f, i) corresponding galvanostatic discharge curves for various kinds of energy-storage materials. A pseudocapacitive material will generally have the electrochemical characteristics of one, or a combination, of the following categories: (b) surface redox materials, (d) intercalation-type materials, or (e) intercalation-type materials showing broad but electrochemically reversible redox peaks. Electrochemical responses in (g–i) correspond to battery-like materials. Adapted from reference[103] with permission from © 2018 American Chemical Society.

Furthermore, the contribution of each diffusion and capacitive processes in the total energy storage can be calculated quantitatively using the following equation:

$$i(V) = k_{Cap.}v + k_{Dif.}v^{0.5}$$

Where i(V) is the current at fixed potential, $k_{Cap.}$ and k_{Dif} are adjusted capacitive and diffusion parameters, $k_{Cap}\,v$ is the capacitive contribution and $k_{Dif}\,v^{0.5}$ is the diffusion contribution. By rearranging the above equation, $k_{Cap.}$ (slope) and $k_{Dif.}$ (intercept), can be easily calculated. As a

result, it is possible to specify the current fraction arising from the ion diffusion (Faradaic current) and the current fraction arising from the capacitive process (non-Faradaic current) at certain potentials.

1.4.5. Electrochemistry parameters and notions

Below, we present some of the electrochemistry parameters and notions used to describe the performance and operating conditions of energy storage systems.

Specific capacity (mA h g^{-1}) typically refers to the amount of charge that a battery or other energy storage device can hold per unit of mass. In rechargeable batteries, specific capacity can be expressed in either charged or discharged specific capacity. The theoretical specific capacity of any active materials can be calculated using the following equation.

$$Theoretical\ specific\ capacity = \frac{NxF}{txM.wt}$$

Where, N = number of electrons transferred or the number of redox active sites per repeating unit in a periodic framework (COFs, MOFs), F = Faraday constant (96485 A s mol^{-1}), t is the time in seconds, and M = molecular weight of the repeating unit of the active materials.

Current density describes the amount of electric current flowing through a unit area of a material. It is typically having units of milliamperes per gram (mA g^{-1})

Current rate is a measure of the rate at which a battery is charged or discharged relative to its capacity. It is typically denoted by the symbol C-rate defined as the measurement of current in which the battery is charged or discharged at. For instance, A fully charged battery with a capacity of 10 Ah should be able to deliver at 1 C 10 Amps for one hour and 5 Amps for two hours at 0.5 C.

Scan rate Scanning rate in cyclic voltammetry (CV) describes how quickly the applied voltage varies throughout an experiment. Typically, the scan rate is given in millivolts per second (mV/s) or volts per second (V/s) units. In CV experiments, the choice of the scan rate is crucial since it can change the characteristics and shape of the resulting CV curve. A wider and more distorted CV curve is often produced by a faster scan rate, while a narrower and more defined curve is produced by a slower scan rate.[103]

Coulombic efficiency is a measure of the efficiency of a battery or electrochemical system during charging and discharging cycles. It is expressed as a ratio of the amount of charge delivered during discharge (in Coulombs) to the amount of charge required to fully charge the battery (also in Coulombs). Mathematically, Coulombic efficiency is expressed as:

$$\text{Coulombic efficiency} = \frac{\text{discharged capacity}}{\text{charged capacity}} \; x \; 100\%$$

A battery's Coulombic efficiency can provide important details about its performance and health over time. While a high Coulombic efficiency can suggest a well-designed and well-maintained battery, a decreasing Coulombic efficiency over multiple charging and discharging cycles can indicate the beginning of deterioration or damage to the battery.

Rate capability usually refers to the ability of a system or material to maintain its performance or functionality at higher current rates of operation.

Specific energy is a measure of the amount of energy that a battery or other energy storage device can store per unit of mass of the active materials. It is expressed in units of watt-hours per kilogram (W h kg^{-1}).

Specific power is a measure of the power output of a battery or other energy storage device per unit mass of the active materials. It is typically measured in units of watts per kilogram (Wkg⁻¹).

Specific capacitance is the ability of a material to store electrical charge per unit mass. Usually, materials with porous structures and high surface area, such as activated carbon, are known to demonstrate high specific capacitance. It is expressed by units of Farad per gram (F g⁻¹)

$$Specific\ Capacitance = \frac{2\ x\ discharge\ current\ x\ discharge\ time}{mass\ of\ active\ material\ x\ discharge\ potential}\ (For\ coin\ cell\ )$$

1.5. Research Challenges

Experimental specific capacities for polymeric materials are found to be inferior to theoretical capacities as a result of synthetic constraints, lack of solid-state architectural tunability, and limited conductivity. Excluding conductive polymers, organic materials are not conductive, and their use in electrodes requires additives like conductive carbon to improve electron transport and ensure high utilization of the redox-active material, which is required for high-rate performance (power density). Such limitations limit the accessibility of the redox-active sites and slow down cation diffusion kinetics impeding the effective use of organic materials as electrodes in batteries. Therefore, addressing these challenges by developing new organic materials with improved textural and electronic properties is essential for the future development of the field. In light of this, crystalizing COFs with a core of rich C=N redox active sites was a priority at which crystallinity is considered as one of the most critical metrics of product quality along with homogeneity, degree of structural order, and eventually, the degree of π-electron conjugation.[106] This kind of structural order, with a lower number of defects, can help in swift reversible dynamic imine condensation reaction and facilitate the accessibility of sodium ions to all redox-active sites during sodiation and desodiation and thereby increase the electronic conductivity.[107,108]

Furthermore, amorphous COFs decrease the surface area significantly due to a lack of structural order and definite channels. Although the difficulty of high synthesis order and high crystalline COF using the conventional polycondensation method, we successfully synthesis a number of highly crystalline COFs with the high Brunauer-Emmett-Teller (BET) ($SA_{BET} = 550\text{-}1250 \ m^2 \ g^{-1}$) by carrying the reaction under an evacuated ampule.

Conductive redox-active COFs were proven to be efficient, inexpensive, green, and durable electrode materials for SIBs in order to find a replacement for state-of-the-art commercial LIBs. Also, the synthesis was tailored to produce COFs having high porosity, a large number of condensed redox-active sites, and low molecular weight per repeating unit to enhance the gravimetric capacity. Besides its conductivity, COFs can be designed to have a high surface area, built-in redox-active sites, and large pore diameters which can accommodate bigger metal ions (i.e., K^+, $Mg^{2+,}$ and Al^{3+}) than the conventional ions (Li^+ and Na^+), which open the door for new and more sustainable battery technologies. In addition, the crystalline nature of COFs allows for a better understanding of the sodium storage mechanism, which remains one of the major impediments facing the commercialization of SIBs.

1.5.1. Specific Objectives

The research project aims to develop novel materials for electrochemical energy storage applications. This involves synthesizing unique amine and aldehyde building blocks that can be used to build conductive COFs with versatile applications. To enhance the ionic mobility through the pores, the project focuses on crystallization COFs with high surface area. Another important aspect is the design of COFs with dense redox active sites per repeating unit to improve their efficiency as electrode materials for energy storage devices such as LIBs, SIBs and supercapacitors. Additionally, highly conductive benzimidazole linked polymers (BILPs) are

being designed as an alternative electrode material for SIBs, LIBs and supercapacitors. The project also involves designing metal-based porphyrin building blocks that can be incorporated into a COF for use in lithium and sodium sulfur batteries applications. Overall, the research aims to contribute to the development of more efficient and versatile materials for electrochemical energy storage.

Chapter 2. Characterization of Materials for Energy Applications

Many different characterization techniques were used to examine the compatibility of materials for battery applications as discussed in this chapter.

2.1. Nuclear Magnetic Resonance (NMR)

NMR is a powerful analytical method used to investigate the magnetic characteristics of atomic nuclei. The NMR is based on the idea that some atomic nuclei have magnetic moments that can interact with an external magnetic field. In NMR, a sample is exposed to a powerful magnetic field, which aligns the sample's atomic nuclei with the field. Next, to excite the nuclei to a higher energy state, a second magnetic field that is applied perpendicular to the first one is used. When the second magnetic field is turned off, the nuclei revert to their original energy state and release a measurable electromagnetic signal. The signal can be analyzed to provide information about the sample's chemical and physical properties. Two of the most often employed NMR types in chemistry and biochemistry are proton NMR (^{1}H NMR) and carbon-13 NMR (^{13}C NMR) in which the selection is based on the type of nucleus being investigated and the particular application. For instance, NMR is frequently employed to investigate chemical composition, functional groups and molecular conformation.

2.2. Attenuated Total Reflectance Infrared Spectroscopy (ATR-IR)

Attenuated Total Reflectance Infrared (ATR-IR) is a spectroscopic non-destructive technique used to examine the molecular composition of a material. In ATR-IR, the sample is placed on a high refractive index made material like germanium or silicon which is in contact with an internal reflection element. In order to excite the molecules in the sample, the infrared light penetrates the sample causing the light-absorbed molecules to vibrate. The distinctive absorption spectra that are

created by the molecules' vibrations can be utilized to identify the functional groups that are present in the sample. Without the need to prepare a KBr pellet, the ATR-IR approach enables the immediate examination of liquid samples or low solubility solid samples such as powders, coatings, and polymers.

2.3. Powder X-ray Diffraction (PXRD)

Powder X-ray diffraction (PXRD) is a robust analytical method that is commonly employed in materials science, chemistry, and physics to determine the crystal structure and phase of materials. It is a non-destructive method that includes exposing a powdered sample to X-rays. Depending on how the atoms are arranged in the crystal lattice, the arrangement of the X-rays causes varying angles of scattering. In a PXRD experiment, a powdered sample is inserted in the path of a monochromatic X-ray beam, which is subsequently diffracted by the crystal lattice. The intensity of the diffracted X-rays at various angles is recorded by a detector, which also collects the diffraction pattern. According to Bragg's Law, the resulting diffraction pattern is a series of peaks that correspond to the different crystal planes that diffract the X-rays. PXRD analysis of polymeric materials can offer important details about their solid-state structure, including the degree of crystallinity, phase composition, and several other molecular-level details. The aforementioned factors play significant roles in the assessment of a polymer's overall behavior in storing and transporting charge within the framework of this research, making PXRD a crucial instrument in this research work. The crystal structure of COFs can be identified using PXRD, which is essential for understanding their characteristics and possible applications. COFs often have a crystalline structure that can be described by Bragg's Law. The lattice parameters, which reflect the size and orientation of the crystal unit cell, as well as the position and strength of the diffraction peaks, which can be used to identify the crystal structure, can be found from the diffraction pattern

obtained by PXRD. Furthermore, PXRD can help to predict the interlayer spacing between the crystal planes. PANalytical Empyrean Diffractometer with Cu K radiation (1.5418 Å) was used for PXRD characterization reported in this thesis. All measurements were performed under natural lighting. In order to process the data, X'pert HighScore Plus was used.

2.4. Thermal Gravimetric Analysis (TGA)

Thermal gravimetric analysis (TGA) is an analytical method used to examine the weight and thermal changes that occur in a material as it is subjected to a controlled temperature program in a specific environment. TGA is frequently used in materials science, chemistry, and engineering to determine the thermal stability, kinetics of decomposition, and composition of a sample. In TGA, a small sample of the substance is put in a crucible and heated at a constant rate while a highly sensitive balance continuously measures the sample's weight. Purging the chamber with gases like air, nitrogen, or oxygen will control the atmosphere around the sample. Upon heating, the sample undergoes different physical and chemical changes, which are reflected in the weight gain or loss. The results provide valuable information about the thermal stability, purity, and composition of a sample.

2.5. Scanning Electron Microscopy (SEM)

Scanning Electron Microscopy (SEM) is a type of electron microscope that produces images of a sample by scanning the surface with a focused beam of electrons. The sample is usually coated with a thin layer of carbon or metal to enhance conductivity and reduce charging effects. When the electron beam interacts with the sample, different signals are produced including back scattered electrons, secondary electrons, and distinctive X-rays. These signals are detected by different detectors and used to make an image about the surface morphology, topography and composition of the sample in a variety of scientific disciplines, including materials science, biology, and

geology. High-resolution images with magnifications ranging from a few to over a million can be obtained using SEM. Furthermore, SEM can be also used for elemental analysis using energy-dispersive X-ray spectroscopy (EDS) or wavelength-dispersive X-ray spectroscopy in addition to imaging (WDS). These techniques endow the identification and quantification of the element existing in the sample. In this work, the samples were prepared by mounting the material on sticky carbon tape attached to aluminum sample holder. Platinum was utilized to coat the samples with a pressure of 1 x 10^{-5} mbar for one minute before SEM imaging. SEM characterization was done using Hitachi SU-70 FE-SEM.

2.6. High-Resolution Transmission Electron Microscopy (HRTEM)

HRTEM is an effective method used to acquire precise images and structural data of materials at the atomic level. A thin sample of a material is contacted by a high-energy electron beam, and the resulting interactions produce images that show the internal structure of the material with atomic resolution. In HRTEM, a number of electromagnetic lenses are used to focus the electrons onto a thin sample after they have been accelerated to extremely high speeds. The atoms in the sample interact with the electrons as they move through it, causing the electrons to scatter and diffract. A detector then detects and records the scattered electrons in order to create an image of the sample. Numerous applications of HRTEM can be found in many different fields of engineering and science, including biology, nanotechnology, and materials science. It can be used to investigate the electronic properties of materials as well as the crystal structure, defects, interfaces, and surface structures of various materials. HRTEM is also used to visualize the sample morphology, crystal structure, particle size and the arrangement of atoms in nanoparticles, nanowires, and other nanoscale structures.

2.7. X-ray Photoelectron Spectroscopy (XPS)

X-ray Photoelectron Spectroscopy (XPS) is a surface analysis technique used to study the chemical composition of materials. In XPS, a sample is irradiated with X-rays, which cause electrons to be ejected from the material's surface. By measuring the energy and quantity of electrons released from the sample, the chemical composition of the substance and the oxidation state of each element can be determined. In materials science, chemistry, and physics, XPS is commonly employed to study a variety of materials, such as metals, semiconductors, polymers, and biomaterials. It is a useful tool for understanding the atomic and molecular level characteristics and behaviors of materials. XPS is a powerful measurement tool because it not only reveals what elements exist, but also what other elements they are bonded to. All the XPS data reported in this dissertation were collected using PHI VersaProbe III Scanning XPS Microprobe. Data analysis was performed using CasaXPS processing software.

2.8. Raman Spectroscopy

Raman spectroscopy is a non-destructive technique used in analytical chemistry to study the vibrational modes of molecules. Raman spectroscopy depends on the inelastic scattering of photons, or Raman scattering. It uses a source of monochromatic light, typically from a laser in the visible, near infrared, or near ultraviolet range, though X-rays can also be used. The laser light interacts with molecular vibrations, phonons or other excitations in the system, resulting in the energy of the laser photons being shifted up or down. The energy shift reveals details about the vibrational, rotational and other low-frequency modes in a material. Infrared spectroscopy usually provides comparable but additional data. The sample plot of Raman spectrum is the intensity of the Raman scattered light as a function of the frequency shift from the incident laser light. The spectrum gives information about the structure and chemical composition of the sample, as each

molecule has a distinct Raman spectrum associated to its vibrational modes. Numerous fields, including chemistry, biology, material science, and physics, use Raman spectroscopy. It has applications in the characterization of nanomaterials, the detection of explosives and pollutants, the study of protein conformational changes, and the analysis of drugs. In this work, Raman spectra were taken using Thermo Scientific DXR Smart Raman Spectrometer with laser excitation wavelength source of 532 nm, and laser power was 5 mW.

2.9. Surface Area and Porosity Measurements

Surface area and porosity measurements are important physical properties used to characterize materials. They are commonly used in fields such as chemistry, materials science, and engineering to understand the properties and behavior of materials. Measurements of surface area involve calculating the total surface area of a substance. Both the external surface and any pores or internal surfaces are included in this calculation. Several methods, including gas adsorption, mercury intrusion, and nitrogen sorption, can be used to calculate surface area. Depending on the kind of material being measured and the level of accuracy desired, a specific technique will be employed. The Brunauer-Emmett-Teller (BET) method is a widely used method for calculating a material's surface area. The BET method is based on the idea that a monolayer is formed when a gas molecule is adsorbed onto a surface. Calculating the surface area involves measuring the amount of gas adsorbed at various pressures. The BET method involves exposing the sample to a gas, typically nitrogen or argon, at various pressures and temperatures. The pressure and volume of the gas are measured as it is adsorbed onto the sample. The information is then plotted on a graph of the relative pressure (x-axis) versus the amount of gas adsorbed (x-axis). An adsorption isotherm is the name given to the resulting curve. Also, pore size distribution of the materials can be obtained by the BET method. Using mathematical models like non-local density functional theory (NLDFT)

and the Barrett-Joyner-Halenda (BJH) methods, it is possible to determine the size and number of pores by measuring the amount of gas adsorbed at various pressures. N_2 isotherms were collected using 3Flex Surface Characterization Analyzer (Micrometrics) after degassing the samples at 120 °C for 24 hours under vacuum.

2.10. Electrochemical study and measurements

The electrode composite was prepared by mixing the active material, conductive carbon (Ketjen Black or Super P), and binder (sodium alginate or poly polyvinylidene difluoride (PVDF)). The three components were pulverized to increase polymer nucleation. Then, a slurry is made by mixing the components with either milliQ water or N-methyl-2-pyrrolidone (NMP). The solvent is added and left under stirring for 12 h until achieving the honey-texture homogeneous slurry. The resulting slurry was cast onto an aluminum-current collector using a doctor blade and dried at 60 °C overnight in a vacuum oven. The dried material was then cut into circular discs of 15 mm diameter to afford an areal mass loading of $0.6-1.14$ mg cm^{-2}.

Due to the fact that coin cells are small, easy to assemble, and feasible for testing small amounts of novel active materials, coin cells have been used for initial work to examine high-performing materials, in addition to modifying the compositions, fabrication parameters, and cycling conditions in laboratories for the past 30 years.[109,110] The prepared electrode was used as the working electrode and tested in sodium or lithium metal half-cell. The cathode composite was assembled in a CR2032-type coin cell with a sodium or lithium metal as the anode. The metal was cut into circular discs (thickness = 0.6 mm) to be used as a counter and reference electrode. 1.0 M $NaPF_6$ in diethylene glycol dimethyl ether (DEGDME) was used as the electrolyte solution (30 μL mg^{-1} of active material), while polypropylene (Celgard 3501, LLC, Corp., USA) was used as the separator between the electrodes. The cell caps and spacers were made from SS 304, while spring

was made from SS 301, providing loading forces of up to 12 pounds at a deflection of 1 mm.[109,110] Electric crimper (MTI Corp.) was used to compress the battery's components and to make the battery. The entire battery assembly process, as shown in Figure 2.1, was done in an Argon-filled glovebox with an oxygen level below 1 ppm. The following electrochemical tests will be conducted to evaluate the cathode performance in the half coin cells.
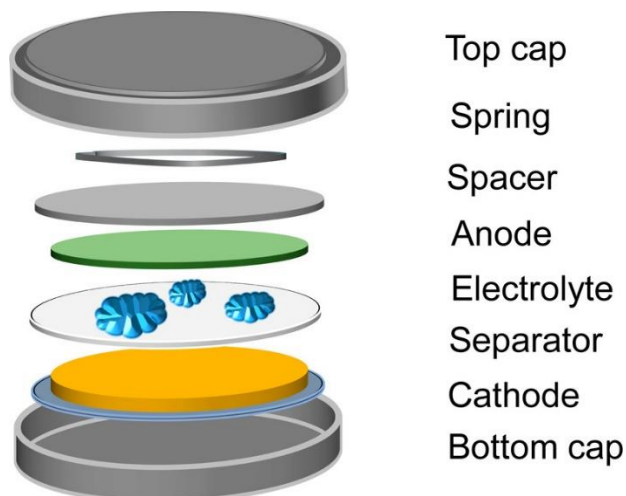
Figure 2.1 Schematic representation of a coin cell assembly. Adapted from reference[109] with permission from © 2017 American Chemical Society.

2.10.1. Cyclic Voltammetry (CV)

Cyclic voltammetry is an electrochemical method used to investigate the redox properties of a chemical species. Cyclic voltammogram of an electrochemical cell is a plot of the potential vs the current at specific scan rate. This technique will be used to determine the mechanism of the redox reactions (charge/discharge) occurring in the cell and provide insights into reversibility and electron transfer kinetics of the redox reactions. Also, the oxidation and reduction potential data will be used to determine the potential window for the future characterizations of electrodes under coin cell settings. Furthermore, CV at different scan rates can help identifying the electrochemical

storage mechanism to be capacitive (capacitor-like), diffusive (battery-like) or in between (pseudocapacitor-like). In this work, CV was carried out on CHI600 C electrochemical workstation.

2.10.2. Galvanostatic Charge and Discharge Cycling (GCD)

Galvanostatic charge and discharge cycling is an electrochemical technique that is frequently used in battery research to evaluate and characterize the performance of various battery types. It can offer useful details about the battery's capacity, voltage profile, and cycling stability, all of which are crucial for the development of high-performance batteries with long lifespans for a variety of applications, including portable electronics and electric vehicles. In this technique, a constant current (i) will be applied to the battery, and the potential (V) of the cell will be measured as a function of time (t) for several cycles, which can be used to determine the specific capacity of the cell. Potential vs. specific capacity curve and specific capacity vs. cycle number will be used to represent the reversibility of the cell. For rate capability studies, specific capacity determination for an electrode material will be carried out at different current rates (C-rate). A plot of specific capacities vs. current rates demonstrates the rate capability of the cell, which requires faster charging and discharging of a battery. GCD cycling was carried out on a 8-channel battery analyzer (MTI Corp.) at room temperature.

2.10.3. Electrochemical Impedance Spectroscopy (EIS)

EIS is a powerful technique to study the electrical properties of electrochemical systems, including batteries, fuel cells, and sensors. EIS can offer important information about the electrochemical and electrical properties of a system, including its resistance, capacitance, and inductance. It can also provide information about the kinetics of electrode reactions, and the diffusion coefficient of species in solution. The Nyquist plots derived from EIS studies can demonstrate reaction

mechanisms, electrode kinetics at the electrodes, and changes at the electrode surface during cycling, and solid electrolyte interface (SEI) layer formation. Equivalent circuit models are often utilized to analyze EIS spectra which allow the numerical elucidation of the electrochemical systems in terms of electrochemical components such as electrolyte resistance, charge transfer resistance, and Warburg resistance. EIS was carried out in the frequency range from 1 MHz to 0.01 Hz with an amplitude of 5 mV on CHI600 C electrochemical workstation.

Chapter 3. Exceptional Sodium-Ion Storage by Aza-Covalent Organic Framework for High Energy and Power Density Sodium-ion Batteries

3.1. Introduction

Covalent organic frameworks (COFs) are highly ordered cross-linked organic polymers consisting of chemically diverse building units held together by strong covalent bonds.[69,111] The chemical composition and textural properties of COFs are precisely tailored, making them excellent platform applications in important fields like gas capture and storage [112], drug delivery[75], catalysis[76], and electrochemical energy storage.[113,114] For instance, COFs have shown great promise in pseudocapacitors[77,78] and rechargeable batteries[80–82]; they have highly cross-linked networks that preclude their dissolution in electrolytes while their porous nature and π-conjugated backbones ensure sufficient charge transfer and provide rapid ion transport and accessibility to dense redox-active sites. Another important attribute of COFs is their ability to reversibly accommodate large ions in their pores, making them very attractive electrode materials in sustainable batteries. In contrast to lithium-ion, the larger ionic size of sodium and potassium ions, for example, limits the use of conventional electrode materials like graphite and inorganic transition metal oxides. As such, the development of new electrode materials capable of integrating abundant and multivalent metals into rechargeable batteries is highly desirable to address the high demand for energy storage materials and their sustainability.[86]

Despite the intense research efforts aimed at finding new effective rechargeable batteries, lithium ion batteries (LIBs) remain central for powering electric vehicles and portable electronics and, to

some extent, represent a convenient storage media for grid-scale energy applications because of their well-established manufacturing processes, long-term durability, and high specific energy.[83] Nevertheless, new battery technologies are deemed vital to address the limited resources of lithium and its geographical distribution and relatively high cost.[84,85] Some earth-abundant metals such as sodium[19,80,81], potassium[86], magnesium[87], and aluminum[88] have been investigated as lithium alternatives in batteries. Among these options, rechargeable sodium-ion batteries (SIBs) have the potential to address many of the aforementioned issues of LIBs because sodium metal is much cheaper than lithium and widely accessible. As such, large-scale production of efficient and durable SIBs would have great implications in the automotive industry and large-scale stationary energy storage technologies.[115] However, SIBs suffer from sluggish kinetics of ion transport, limiting their performance, especially their high rate capability, which requires fast charge/discharge rates. Attempts have been made to advance SIBs using organic materials because of many advantages like low cost, high natural abundance, environmentally friendly, lightweight, which give rise to high gravimetric capacities.[8–15] Furthermore, because of their excellent structural flexibility and versatility, organic materials are precisely constructed to host densely packed redox-active sites of different redox potential as part of their skeleton.[16,17] As a result, various organic materials have been tested in electrodes, including traditional conducting polymers[12], organic radical compounds[18], organic carbonyl compounds[19], organosulfur compounds[20], and organic carbon/nitrogen compounds including polymeric Schiff base[21], and azo compounds[22], among others. However, dissolution in organic electrolytes, low electronic conductivity, little redox stability, and many defects in the π-conjugated frameworks are the inherent problems of organic compounds.[25,26] Many of these challenges could be addressed using

40

the reticular chemistry of COFs.[116] This strategic synthetic methodology enables embedding dense redox-active sites into porous and crystalline π-conjugated frameworks.[27,28]

Herein, we report the synthesis of crystalline Aza-COF and its use as a cathode in half-cell SIBs. We demonstrate how the reticular chemistry of COFs allows for exceptional energy and power densities in SIBs. The crystallinity and porosity of Aza-COF facilitate rapid and reversible accessibility of sodium ions and electrons to dense phenazine redox-active sites during sodiation and desodiation. The Aza-COF-based electrode exhibits a very high average specific capacity and cycling stability combined with remarkable energy and power densities, making Aza-COF a very promising electrode material for SIBs.

3.2. Experimental section

3.2.1. Materials

All chemical reagents were obtained from commercial suppliers and utilized as received. Hexaketocyclohexane octahydrate (HKH·8H$_2$O, Fisher Scientific, 97%), 1,2,4,5-benzenetetramine tetrahydrochloride (TAB·4HCl, Sigma Aldrich, technical grade), N-methyl-2-pyrrolidinone (NMP, ACS grade, Alfa Aesar, 99%), conductive carbon black (Super P, Alfa Aesar, 99+%), sodium alginate (Alfa Aesar, high viscosity), sodium hexafluorophosphate (NaPF$_6$, Alfa Aesar, 99+%), diethylene glycol dimethyl ether (DEGDME, Sigma Aldrich, anhydrous 99.5%). Aza-COF was prepared according to literature.[25,79]

3.2.2. Synthetic Method

3.2.2.1. Synthesis of Aza-COF

A crystalline Aza-COF conjugated microporous polymer was synthesized via an acid-catalyzed polycondensation reaction according to the literature (Scheme 3.1).[1] A 50 mL Schlenk flask was charged with 1,2,4,5-benzenetetramine tetrahydrochloride (TAB·4HCl, 485.3 mg, 1.71 mmol),

41

hexaketocyclohexane octahydrate (HKH.8H$_2$O, 355.4 mg, 1.14 mmol) and a half-inch stir bar. 7

ml N-methyl-2-pyrrolidone (NMP) followed by five drops of sulfuric acid were added while

stirring over 15 minutes under nitrogen. The reaction mixture was kept under stirring at room

temperature for an extra 30 minutes before being heated with stirring to 185 °C for 5 days. The

black precipitate was filtered and washed with water (30 mL × 3) and acetone (30 mL × 5). The

powder was purified by Soxhlet extraction with methanol for three days and then dried in a vacuum

at 150 °C for 21 hours to give Aza-COF as a black powder (280 mg, yield 92%).
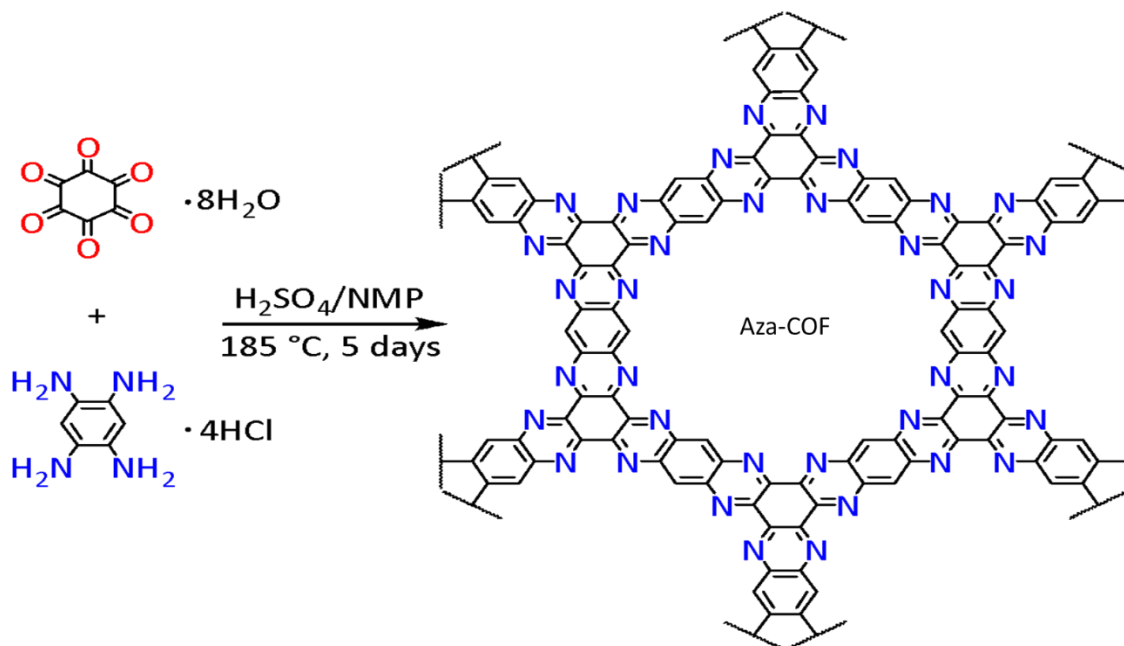
Scheme 3.1 Synthesis of Aza-COF.

3.2.3. Physical and Spectral Characterization

Infrared transmittance spectra were collected by attenuated total reflection infrared spectroscopy

(ATR-IR). Porosity measurements were collected on a 3Flex surface characterization analyzer

(Micrometrics) using nitrogen adsorption/desorption isotherms at 77 K. Aza-COF was degassed

at 150 °C for 24 h under vacuum (1 x 10^{-6} bar). PHI VersaProbe III scanning XPS microprobe was

used to run X-ray photoelectron microscopy (XPS). For Raman spectroscopy studies, a laser with

5 mW power was used to excite the samples at 532 nm using Thermo Scientific DXR Smart Raman. Scanning electron microscopy (Hitachi SU-70 FE-SEM) was used to get images at high magnification. To enhance the conductivity of Aza-COF, platinum at a pressure of 1×10^{-5} mbar was used to coat the samples for one minute before imaging. Coin-cell de-crimping device (MTI) was used to dismantle the coin cell in an argon-filled glovebox. Then, cathodes were carefully separated and kept under N_2 until ready for testing.

3.2.4. Coin Cell Assembly

The cathode composite was prepared using 60 wt % active material (Aza-COF), 30 wt % carbon black, and 10 wt % binder (sodium alginate). The three components were pulverized and mixed with doubled deionized water (DDW) as a solvent. A slurry containing all components mentioned above was cast into a thin film using a doctor blade on an aluminum foil (the current collector). The cathode was assembled in a CR2032-type coin cell with a sodium metal used as the anode, reference, and counter electrode. The electrolyte solution was prepared from $NaPF_6$/DEGDME (1.0 M). A polypropylene membrane was used as the separator between the electrodes. An electric crimper (MTI Corp.) was utilized to assemble all battery components in a coin cell inside an argon-filled glove box.

3.2.5. Electrochemical Measurements

The electrochemical analyses of all coin cells were examined and obtained at ambient temperature. Eight channels battery analyzer (MTI Corp.) was used for long-term cycling stability, galvanostatic charge/discharge, and rate capability measurements. On the other hand, an electrochemical workstation (CHI 600C) was used to get data of the electrochemical impedance spectroscopy (EIS) and the cyclic voltammetry (CV).

3.3. Results and Discussion

The use of molecular hexaazatrinaphthalene (HATN) and its integration into polymeric networks for battery and supercapacitor applications have been documented in literature. It is worth noting that the electrical conductivity and theoretical specific capacity of the polymeric networks are directly affected by the connectivity between the HATN building units (Figure 3.1 a). We envisioned that both parameters could be addressed using highly conjugated and phenazine-rich frameworks like Aza-COF.[25,79] Thus, Aza-COF was selected for this study because of its extended π-conjugated nature and readily accessible to abundant redox-active sites. Aza-COF was synthesized by the condensation of HKH·8H$_2$O and TAB·4HCl in NMP using H$_2$SO$_4$ as a catalyst at 185 °C (Scheme 1). The connectivity between the building blocks was confirmed by ATR-IR (Figure 3.1 b).
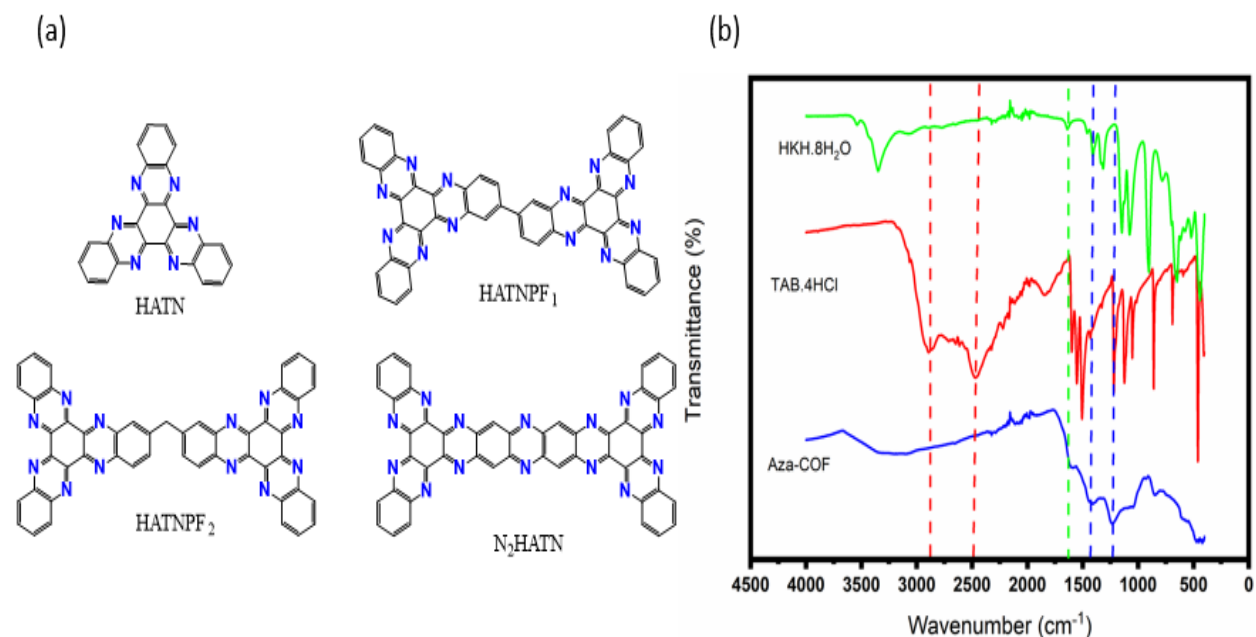
Figure 3.1 (a) Selected HATN-based frameworks b) ATR-IR spectra comparing the building blocks and the Aza-COF.

Aza-COF forms 2D sheets stacked in eclipsed conformation (Figure 3.2 a, b).[106,117,118] The resulting material is crystalline, as evidenced by powder X-ray diffraction (PXRD) and high-resolution transmission electron microscopy (HRTEM), as depicted in Figure 3.2 c and d. The PXRD pattern contains strong diffraction peaks at 5.29° and 26.7° that can be ascribed to the (100) and (001) planes, respectively, with π-π interplanar spacing distance (d-spacing) of 3.42 Å between the 2D sheets (Figure 3.2 b). This was further supported by HRTEM, which reveals a layered material with a d-spacing of 3.42 Å in line with reported experimental data and predictions from framework modeling studies (Figure 3.2 d).[106,117,118] According to porosity measurements, Aza-COF is microporous with the surface area of $SA_{BET} = 240$ m^2 g^{-1} and pores about 13 Å according to NLDFT calculations.[118]
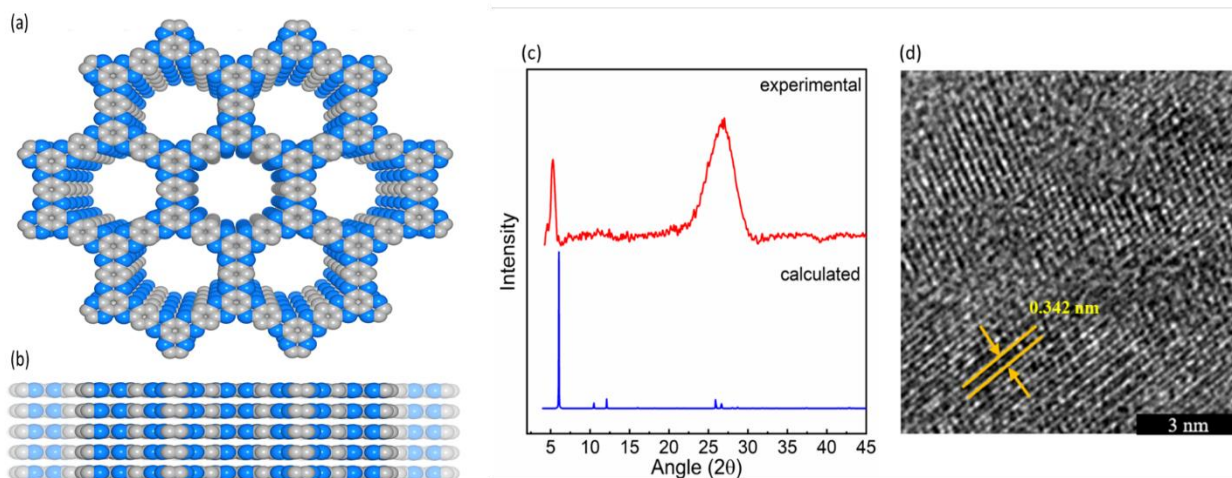
Figure 3.2 (a) Space-filling model showing high phenazine decoration of the channels; gray (C), blue (N), hydrogens were omitted for clarity, (b) side view with theoretical d-spacing of 3.43 Å, (c) PXRD, and (d) HRTEM image of pristine Aza-COF (inset bar = 3 nm).

To evaluate the performance of Aza-COF in SIBs, galvanostatic charge/discharge studies (6 cycles at 0.1 C) were conducted using a voltage window of 0.01 to 3.0 V vs. Na/Na$^+$ taking into consideration the sodium standard electrode potential ca. -2.7 V vs. SHE). The electrode exhibited

a superior charge specific capacity in the first cycle at 581 mA h g^{-1} and a discharge capacity of 523 mA h g^{-1}. The charge and discharge capacities represent 96.3% and 86.7% of the theoretical capacity (603 mA h g^{-1}), respectively, based on a six-electron redox reaction, as shown in Figure 3.3 a. The first charge specific capacity at 581 mA h g^{-1} is the highest compared to the other five charge cycles, which showed reversible stability with capacities ~545 mA h g^{-1} (90% of the theoretical capacity). On the other hand, the discharge capacities for all six cycles were between 517 and 523 mA h g^{-1}. This notable hysteresis, especially in the first charge/discharge cycle capacity (581/523 mA h g^{-1}), could be attributed to side reactions on the electrode's surface, like electrolyte reduction on the negative electrode and the formation of the solid electrolyte interface (SEI) layers. The SEI layers are typically composed of inorganic and organic sodium salts, making the cyclable Na$^+$ ions partially immobilized in the SEI products, leading to capacity degradation.[119]
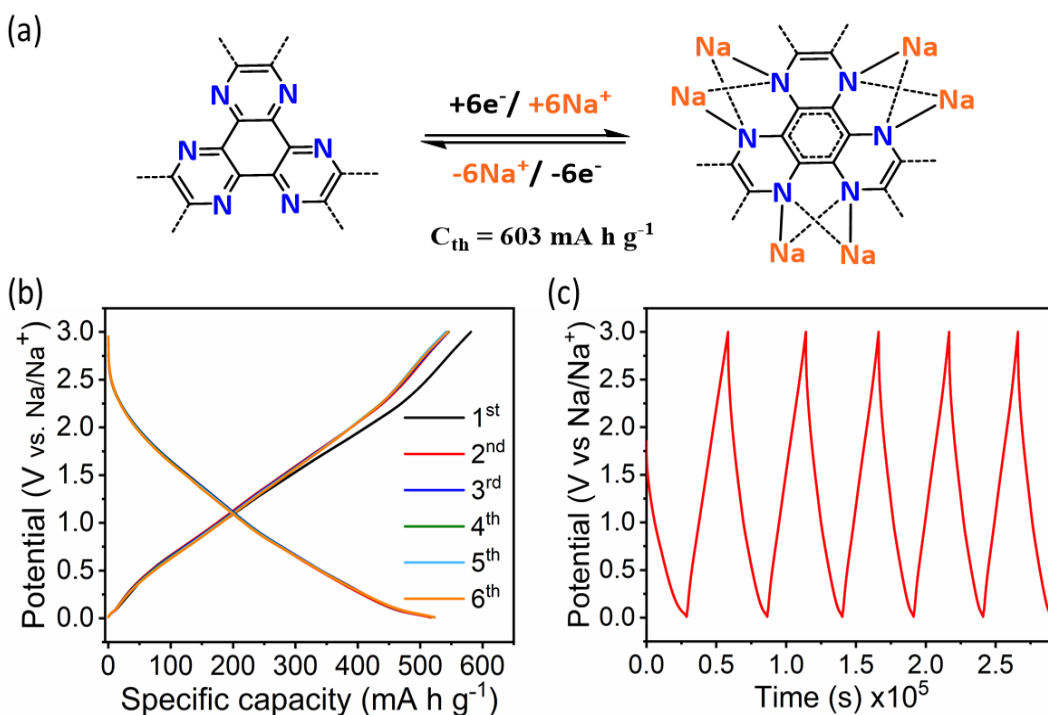
Figure 3.3 (a) Redox mechanism of the aza-sites, (b) Galvanostatic charge/discharge profiles for the first six cycles of Aza-COF vs. Na/Na$^+$ battery at 0.1 C, and (c) time vs. potential profile.

46

Aza-COF galvanostatic cycles showed two reversible curves at around 0.06-0.01 V/0.06-0.13 V, and 2.14-0.304 V/0.3-2.7 V (Figure 3.3), which concurred with the curves of the CV (Figure 3.4). The first charge/discharge slope belongs to the sodium insertion into the pores and contributes less than 5 mA h g^{-1} toward the total specific capacity. However, the second slope originates from redox reactions involving pyrazine sites of the framework.
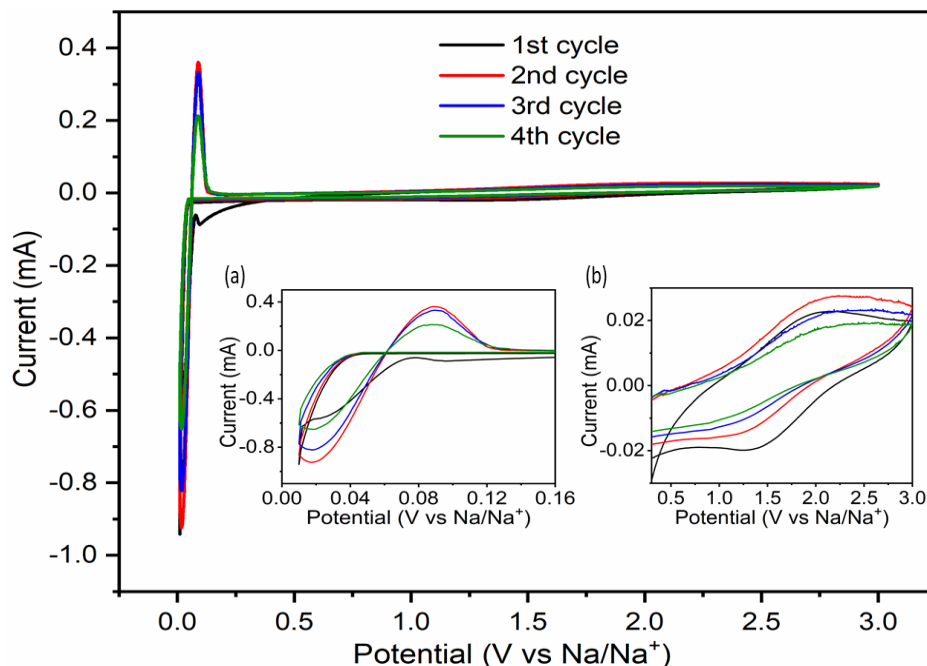
Figure 3.4 Cyclic voltammograms of Aza-COF electrodes in 1M NaPF$_6$/ DEGDME at a sweep rate of 0.1 mV s^{-1} before being cycled. Inset: (a) is the zoom-in region of the potential range between 0.01 and 0.3 V, while inset (b) is the zoom-in region of the potential range between 0.3 and 3.0 V.

CV peaks represent the reversible sodiation (reduction) and de-sodiation (oxidation) processes at the phenazine active sites (Figure 3.4, inset b). However, a distinct peak at 0.02 V (Figure 3.4, inset a) points to the sodium ion incorporation in the pores of the Aza-COF framework. An Inconsistent curve was formed by the first cycle, which could be attributed to SEI thin layer formed on the anode surface during the first discharge, which then harmonized with other peaks upon further cycling.

The reactivity of Aza-COF with sodium was probed using density functional theory (DFT) calculations. A locally modified version of Q-Chem was used to perform all calculations.[120] All structures were optimized using B3LYP hybrid functional[121,122] combined with 6-31G(d) basis set. Subsequent vibrational frequency calculations were further performed to confirm all geometries corresponding to true ground state stationary points and evaluate the contributions from thermal corrections to Gibbs free energy. On top of those optimized geometries, the solvation free energies were obtained using M05-2X hybrid meta functional[123] and 6-31+G(d,p) basis set with the experimental electrolyte solvent DEGDME employing the SMD implicit solvation model.[124] Seven parameters were set for this solvent in SMD: dielectric constant = 7.36;[125] SolN = 1.4273; SolA = 0.00; SolB = 0.48; SolG = 36.846592; SolC = 0.00; SolH = 0.00. Parameters SolA = 0.00 and SolB = 0.48 were based on tetrahydrofuran, which has a similar dielectric constant (7.43) as DEGDME. The sodiation redox potential was measured according to the following formula:[19,40]

$E_{redox} = -(G_f - G_i - G_{Na})/(nF)$ where G_f, G_i, and G_{Na} are the sum of thermal and solvation Gibbs free energies for the final, initial sodiated states of the complex, and for the Na atom, respectively; n represents the number of electrons transferred in the sodiation process, while F is the Faraday constant. The binding energy ΔE (in eV) in the sodiation process was estimated using the formula:

$\Delta E = E_{mNa} - (E_{(m-1)Na} - E_{Na})$ where E_{mNa}, $E_{(m-1)Na}$, and E_{Na} are the solvation free energies for a sodiated complex with m, $m - 1$ Na atoms, and Na atom, respectively. The more negative binding energy points out to the stronger binding between the Na atom and the aza site.

There are six electroactive phenazine N atoms (three pairs) in the HATN molecule, at which two Na atoms can coordinate strongly with each N pair. In other words, each HATN molecule can coordinate with up to six Na atoms. The redox potentials for the first three Na atoms with HATN are 2.18 V, 1.78 V, and 2.08 V, respectively, with an average of 2.01 V. The redox potentials for the

rest of the three Na atoms with HATN are 1.16 V, 1.24 V, and 1.14 V, respectively, with the average

of 1.18 V. The binding energies for the first three Na atoms with HATN are −2.43 eV, −2.09 eV,

and −2.32 eV, respectively, with the average of −2.28 eV. The binding energies for the rest of the

three Na atoms with HATN are −1.42 eV, −1.63 eV, and −1.42 eV, respectively, with an average

of −1.49 eV. The binding strength is much stronger for the first three Na atoms, where each pair

of N atoms are bonded to one Na atom only.

The optimized structures for the reduced HATN (3Na@HATN and 6Na@HATN) are depicted in

Figure 3.5. The initial reduction with three Na atoms leads to Na-N bonds of 2.224-2.242 Å, and

the Na atoms are coplanar with HATN. On the other hand, further reduction with three additional

Na atoms indicates that the first three Na atoms and the rest of the three Na atoms sit on the

opposite side of the plane containing the HATN moiety with Na-N bond distance in the range of

2.264-2.288 Å. It is worth noting that our theoretical studies indicate that the accommodation of

the Na atoms takes place in regions that make up the pores of Aza-COF rather than "intercalating"

between the 2D layers of the framework. The ability of porous COFs to store sodium ions in the

pores is very significant in advancing SIBs since graphitic carbon is incapable of intercalating Na.
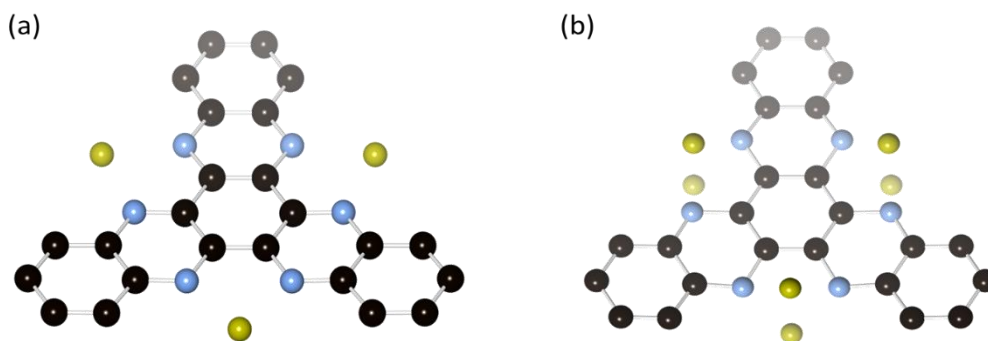
Figure 3.5 Optimized structures for (a) 3Na@HATN and (b) 6Na@HATN; carbon (black), nitrogen (blue), sodium (yellow), Hydrogens were omitted for clarity.

To examine the energy storage mechanism, we used CV measurement having variable sweep rates in the range of 5.0 - 50 mV s^{-1} (Figure 3.6 a) in combination with electrochemical impedance spectroscopy (EIS) to estimate diffusion kinetics of Na$^+$ ion. In theory, the relationship between the active material's voltammetric response and sweep rates can be described as:

$$i = av^b$$

Where i is the peak current, v is the sweep rate, while α and b are constants. Therefore, the relationship between i and v for battery behavior can be described by $i = \alpha v^{0.5}$ (b = 0.5) which represents Na$^+$ ion diffusion-controlled process.[19] Unlike battery performance, normal capacitive behavior is a surface-limiting redox rather than a diffusion-controlled process.[103] Therefore, i should relate linearly with v (b = 1). Analysis of the Aza-COF battery shows that the values of b were 0.668 for anodic and 0.676 for cathodic systems, which is most likely due to short transport paths for both electrons and ions as well as rapid access to the redox-active sites that decorate the pores (Figure 3.6 b).[103] The data presented here indicated that the overall process is a combination of both Na$^+$ diffusion-controlled and surface-limiting redox processes given the material an "extrinsic" pseudocapacitive-like properties.[126]
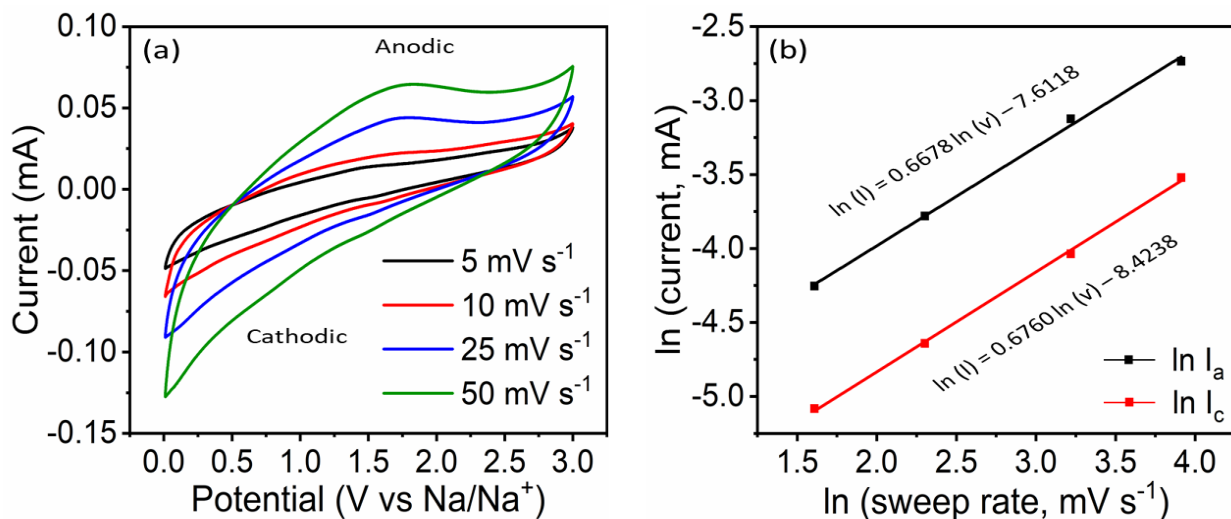
Figure 3.6 (a) CV curves at different sweep rates (5.0-50 mV s^{-1}) of Aza-COF cathode in DEGDME-based electrolyte. (b) The corresponding linear fit of the ln (peak current) vs. (ln sweep rate) at 5, 10, 25, and 50 mV s^{-1}.

For further study of electrode kinetics, EIS was performed for the pristine Aza-COF electrode and after 225 cycles at a frequency range of 0.01 Hz to 1 MHz and 5 mV amplitude. According to the Nyquist plots (Figure 3.7 a, b), both fresh and cycled batteries exhibited semicircles with small diameters, concurred with pseudocapacitive behavior for a speedy surface-controlled Faradic process.[105] However, the low-frequency region shows a straight line that is significantly inclined from the ideal vertical line (45°), which is consistent with battery behavior. The inclined line indicates a higher diffusive resistivity, slower diffusion process of Na$^+$ ions into the bulk of electrode material, and lower charge transfer than ideal pseudocapacitive materials.[105,127] The first intercept points of the semicircle with Z' at the high-frequency section for the pristine and cycled batteries were 10.66 and 16.09 Ω, respectively, (Figure 3.7 a, b), which arise from the electrolyte's resistance and cell components. The impedance data were simulated and numerically analyzed by Randles equivalent circuits (Figure 3.7 c, d). C_1 and C_2 represent the capacitance of negative and positive electrodes, respectively. R_W Warburg resistance for the diffusion processes. The

semicircle at high frequency represents the charge transfer resistance (R_{CT}). Aza-COF-based electrode exhibits a minimal R_{CT} of 1.493 and 2.053 Ω before and after 225 cycles, indicating low charge transfer impedance and enhanced electrochemical performance.
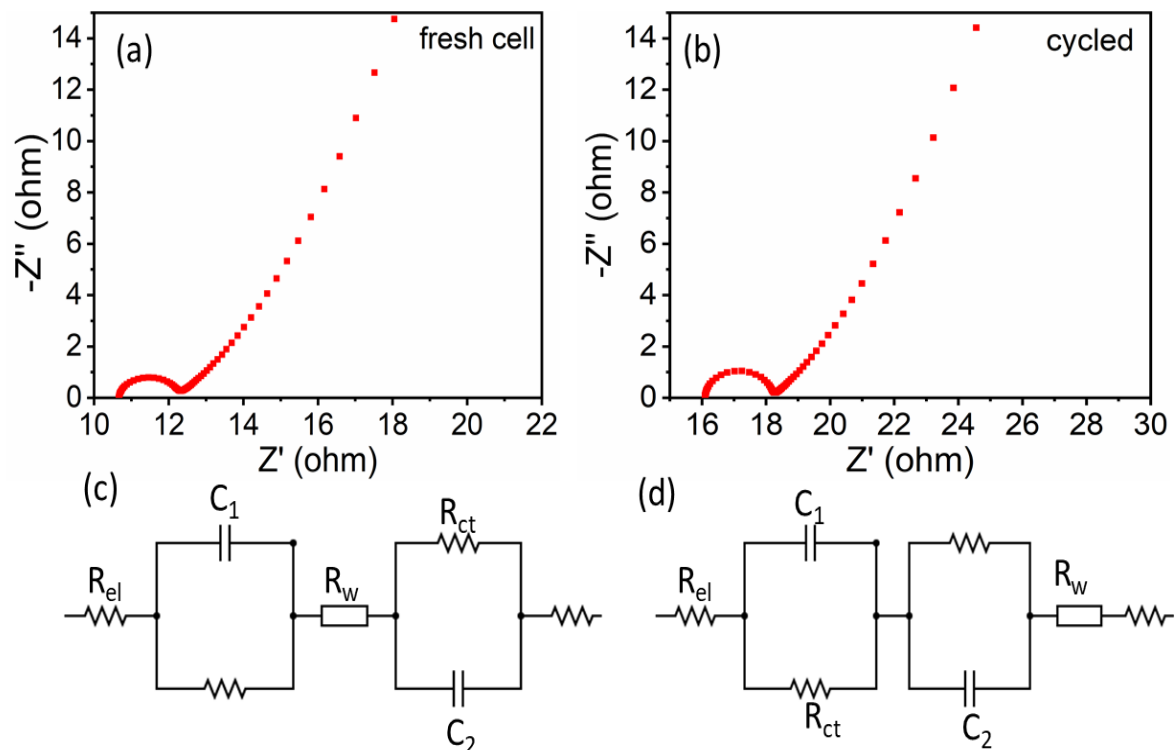
Figure 3.7 Electrochemical impedance spectra for a) battery before cycling and b) after 225 cycles, c) simple equivalent Randles circuit diagram for the battery before cycling, and d) after cycling.

We have used the electrochemical impendence data to estimate the sodium ion diffusion coefficient (D_{Na^+}) before (9.14×10^{-11} cm^2 s^{-1}) and after battery cycling (4.18×10^{-11} cm^2 s^{-1}); the values are somewhat in line with those reported in literature for COFs.[80,128,129](Figure 3.8)
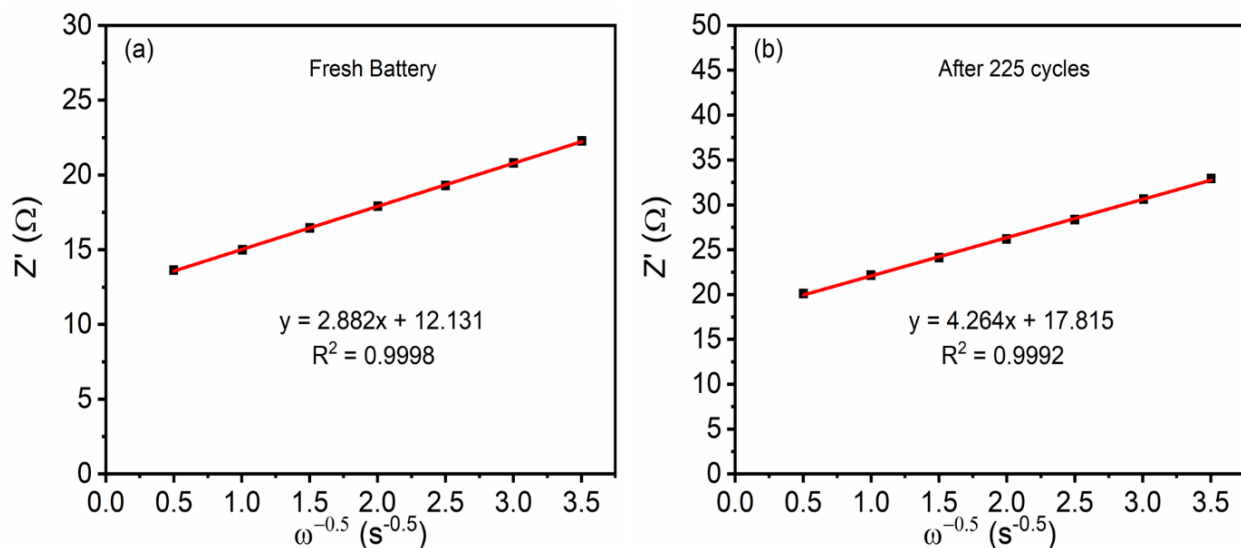
Figure 3.8 The plot of the real impedance resistance, Z′, vs. the reciprocal root square of the lower angular frequencies ($\omega^{-1/2}$) for (a) fresh battery and (b) after being cycled for 225 cycles to measure the Warburg coefficient (σ) which is necessary for the Na$^+$ ions diffusion coefficient before and after 225 cycles.

The durability and functionality of the Aza-COF battery were evaluated by rate capability and prolonged cycling studies. The battery shows stable reversible capacities of 523, 374, 232, and 161 mA h g^{-1} at current rates of 0.1, 1.0, 5, and 10 C, respectively. Even at a higher loading current (20 C), the battery delivers good specific capacity 103 mA h g^{-1} as shown in Figure 3.9 a. Upon current rate reduction back to 0.1 C, the discharge capacity reached ~516 mA h g^{-1} with 99% capacity recovery, attesting to the swift charge exchange kinetics in the extended π-framework during sodiation and de-sodiation process (Figure 3.9 b). Furthermore, the outstanding rate capability is ascribed to the widely accessible 1D channels, high electronic conductivity, and high porosity of Aza-COF.[19,86,89] When high current rates higher than 0.1 C were used, the battery performed very well, and no hysteresis was observed, indicating very reversible processes. A slight hysteresis at a low current (0.1 C) is most likely due to the lower diffusion rate of the Na$^+$ in the inner regions compared to the outermost region of the Aza-COF material due to ion depletion within the pores

and limits the accessibility to the redox-active sites.[130] As expected, when higher current rates were employed, a noticeable drop in capacity was recorded as a result of the ion-diffusion controlled activity.

The cycling performance of the Aza-COF battery showed remarkable stability over 500 cycles at 5 C, with an excellent coulombic efficiency of nearly 100% (Figure 3.9 c). The initial capacity of 278 mA h g^{-1} obtained by the first cycle dropped to 241 mA h g^{-1} after prolonged cycling (500 cycles), showing remarkable capacity retention of ~ 87 % (Figure 3.9 d). This outstanding cycling stability could be ascribed to the chemical and physical stability of Aza-COF and its insolubility in the electrolyte, which preserves high capacity and ionic conductivity.[19,81]
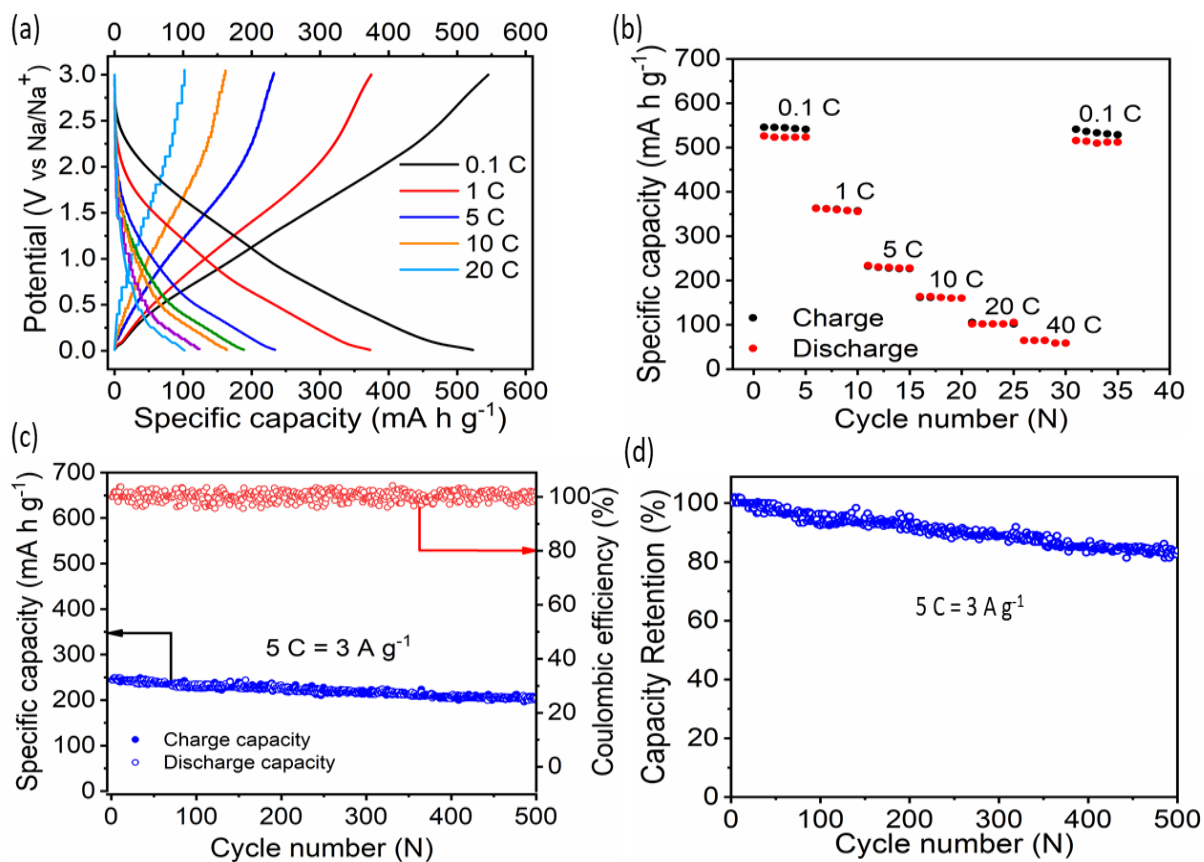
Figure 3.9 a) Galvanostatic cycling profiles, (b) Rate capability, (c) Long-term cycling stability and Coulombic efficiency, and (d) capacity retention at 5 C current rates.

One of the common concerns of organic materials use in electrodes stems from the modest mass loading because of their low density. Higher mass loading of the active material is desired to attain high energy density. Therefore, we investigated the influence of the active material mass loading on the charge/discharge capacity. Three different loadings: 0.45, 0.74, and 1.00 mg cm^{-2}, were used for cathode fabrication (Figure 3.10). It is clear that as the material loading increases, the charge/discharge capacity decreases due to the increased resistance of the composite cathode.[40]
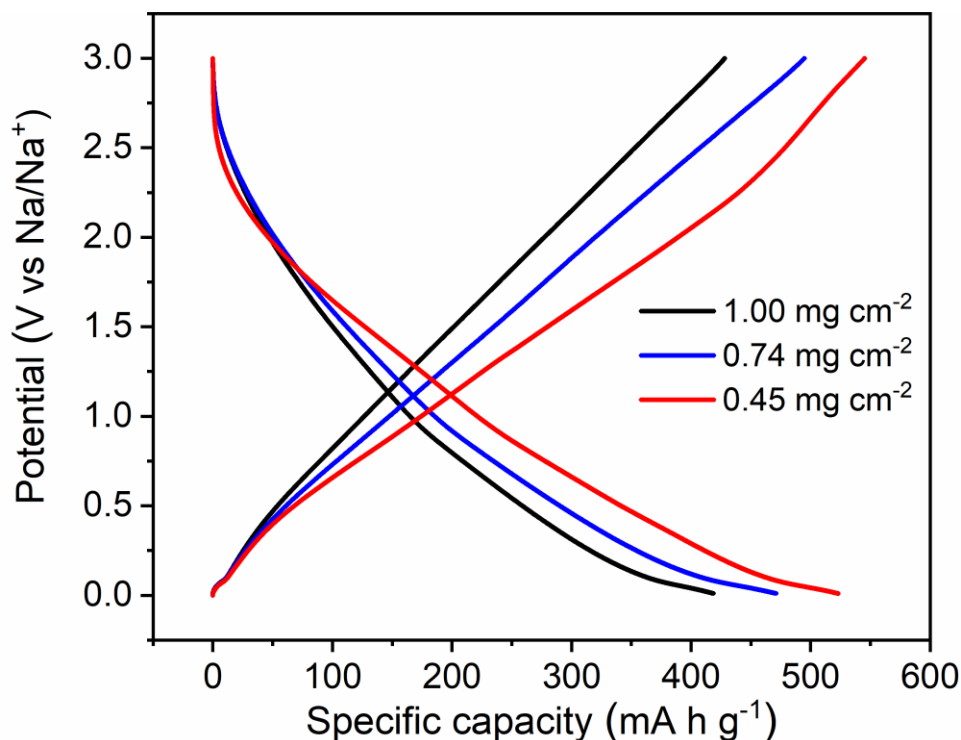
Figure 3.10 The specific charge/discharge capacities of the Aza-COF-based cathode with different loadings of active material (0.45, 0.74, and 1.00 mg cm^{-2}) at a current rate of 0.1 C.

The redox reaction progress during battery cycling was monitored using XPS, and the results were referenced to the C 1s peak at 284.4 eV (Figure 3.11). We noted that the C 1s peak exhibited an asymmetric and broad tail towards higher binding energies, which supports the presence of sp^2-C.[131] The C 1s XPS spectrum of pristine electrode produced a C=N peak at 286.6 eV (Figure 3.11 a), which is seen to disappear during discharging (sodiation). In contrast, a new peak for the

reduced C-N is produced at 286.1 eV (Figure 3.11 b). The C=N peak reappeared on recharging the battery, demonstrating the highly reversible chemistry at the aza-centers (Figure 3.11 c). Furthermore, XPS shows no contribution of C=C as a redox site on the total specific capacity at which C=C and C-C peaks stayed intact in the charge and discharge profiles (Figure 3.11 b and c), indicating that the total capacity accessed is due to aza-redox sites only. The signal at ~289 eV can be ascribed to C-F in SEI. It is interesting to note that for C 1s peak, the full width at half maximum remains unchanged during sodiation (discharge), suggesting minimal intercalated Na$^+$ ion storage in the matrix.[132]
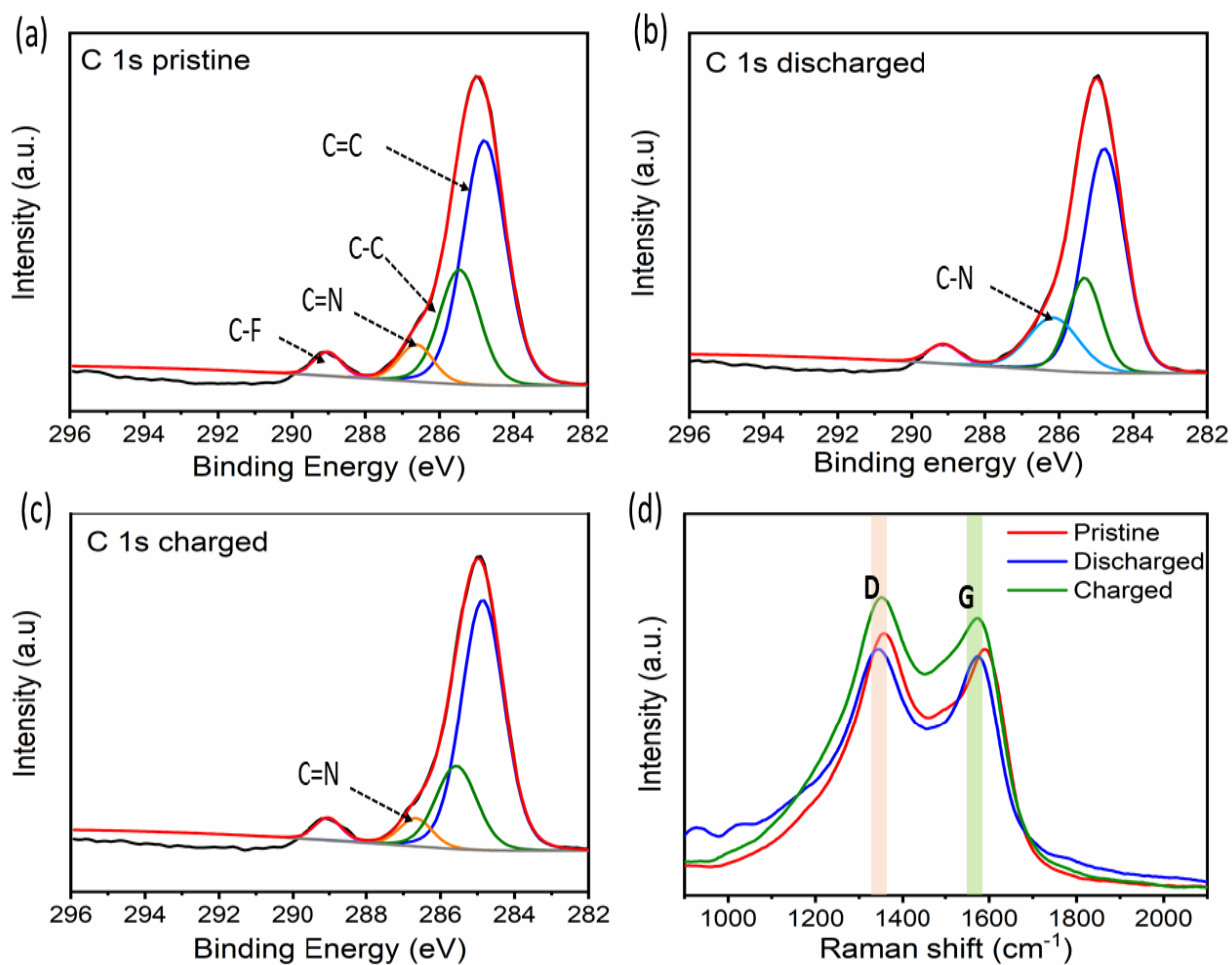
Figure 3.11 Deconvoluted C 1s XPS spectra of (a) Aza-COF, (b) discharged, and (c) charged Aza-COF-based electrodes. (d) Results from Raman studies.

For further investigation of the sodiation/desodiation process, Raman spectroscopy and ATR-IR studies were carried out on Aza-COF-based electrodes in various stages: pristine, charged, and discharged. Unfortunately, Raman spectroscopy ran short in monitoring the actual redox process during the cycling of the electrode. This is due to the fact that the characteristic C-N modes (1250 – 1400 cm^{-1}) and C=N stretching modes (1540 – 1620 cm^{-1}) for Aza-COF are located within the same D and G bands that arise from the high content of carbon black used in the electrode which appears at ~1356 cm^{-1} (D) and ~1574 cm^{-1}(G) as depicted in Figure 3.11 d.[133] However, the small shift of the discharge band 1352 cm^{-1} is most likely due to imine-bond sodiation. On the other hand, The IR results show a clear charge/discharge mechanism. Upon discharging the electrode to 0.01 V, the C=N (1220 cm^{-1}) of the pyrazine disappeared, indicating the C-N-Na formation. However, the C=N band was recovered by charging the electrode to 3.0 V. It is worth mentioning that the C=C stretching band (1612 and 1424 cm^{-1}) did not change during the battery cycling, confirming that the C=C bonds did not contribute as active sites in the observed total specific capacity (Figure 3.12).
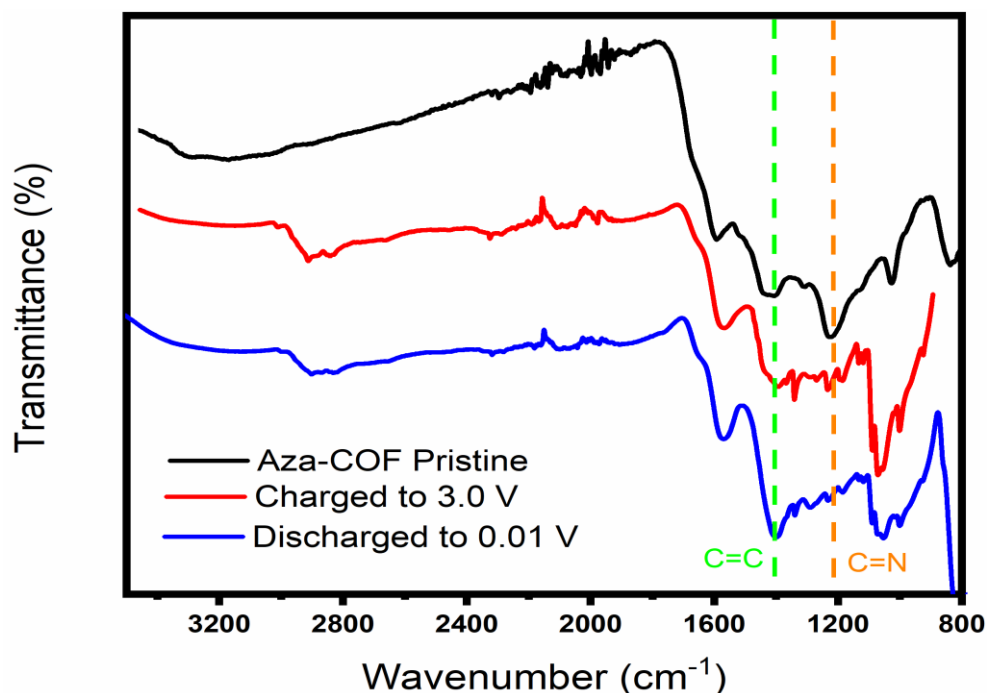
Figure 3.12 ATR-IR for the Aza-COF in various stages: pristine, charged to 3.0 V, and discharge to 0.01 V for further investigation of the sodiation/desodiation mechanism.

The pristine Aza-COF morphology exhibits nano rod-like morphology with an estimated length average of 300 nm and a width average of 80 nm (Figure. 3.13 a). Furthermore, SEM images were also used to investigate the cast Aza-COF active materials' integrity and morphology before and after 125 charge/discharge cycles. The cycled electrode sample was prepared by dismantling the battery and separating the Aza-COF cathode from the separator. The SEM images (Figure 3.13 b, c) show a uniform distribution of Aza-COF and carbon black in both pristine and cycled cast electrodes, which illustrate the high stability and integrity of the electrode due to the minimal morphological changes during cycling. The morphological stability is believed to arise from the reversible accommodation of sodium ions inside the porous channels of Aza-COF.
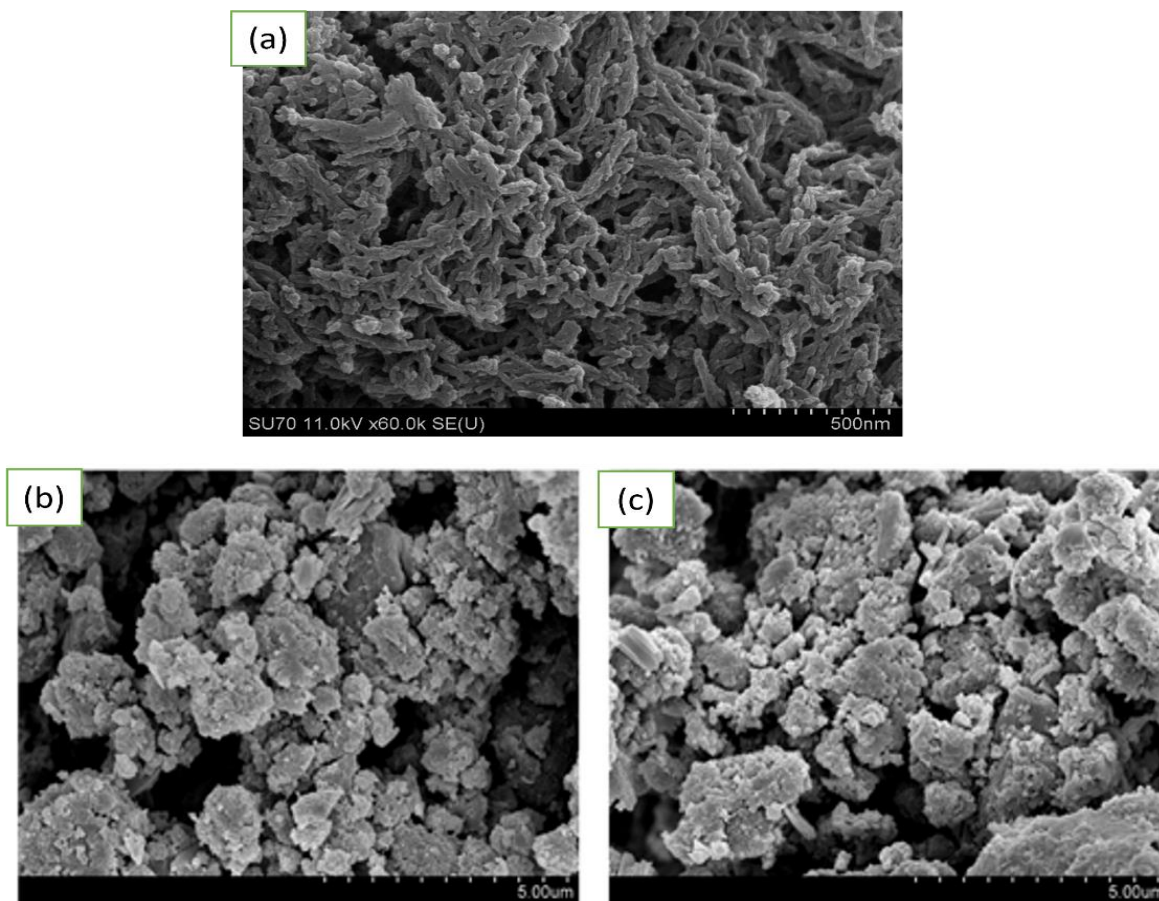
Figure 3.13 SEM images of (a) as-prepared Aza-COF (b) the electrodes before cell assembling and c) after 125 cycles at a density rate of 63 mA g^{-1} in 1M NaPF$_6$/DEGDME.

To explore the effect of the Aza-COF-based electrode on the amount of energy storage as well as the amount of power given per unit mass, energy density and power density measurements were carried out. Combining both high energy density with high-power density is necessary for superior performance in energy storage. The Aza-COF battery attains a remarkable energy density of 492 W h kg^{-1} at 0.1 C (Figure 3.14 a), similar to those reported for best-performing inorganic and organic electrodes for SIBs.[134,135] In terms of power density, Aza-COF exhibits an outstanding power density of 1182 W kg^{-1} at 40 C. Aza-COF battery can deliver at a specific energy of 111 W h kg^{-1} at 8 C, which corresponds to a specific power of 884 W kg^{-1} (Figure 3.14 b).
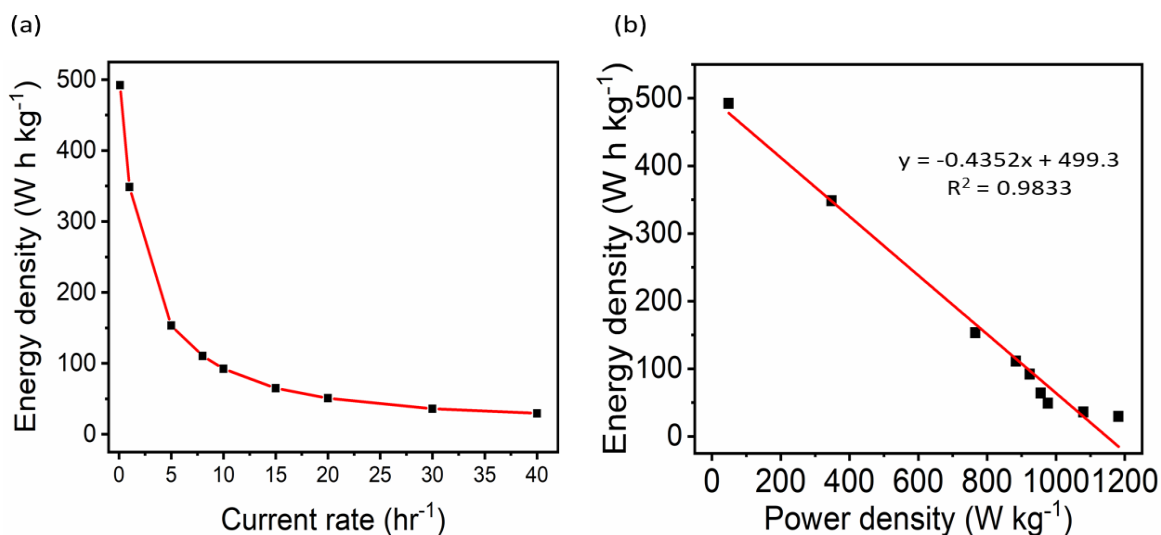
Figure 3.14 (a) Energy density of Aza-COF battery at different current rates of 0.1, 1, 5, 8, 10, 15, 20, 30, and 40 C and (b) Ragone plot.

3.4. Conclusion

In conclusion, we investigated the potential of crystalline porous Aza-COF in SIBs. The 1-D channels and π-conjugation of this COF facilitate rapid sodium ions diffusion and reactivity with the dense redox-active aza sites. Aza-COF-based battery exhibits a superior high average specific capacity (550 mA h g^{-1} at 0.1 C) which is one of the highest reported values for SIBs derived from organic electrodes.[136] This remarkable capacity delivery is attributed to a rapid surface-controlled Faradic process, facile sodium ions diffusion into the bulk electrode, and the accessibility of abundant redox-active aza sites. An outstanding rate capability at different current rates was observed for the battery in the range of 0.1 to 40 C. The battery also exhibited very good stability over 500 cycles retaining 87% of its original capacity and high columbic efficiency. The Aza-COF battery also showed an outstanding energy density and power density as well. We believe this study will help in developing new approaches to systematically advance organic electrodes in sustainable SIBs.

Chapter 4. Templated Synthesis of 2D Polyimide Covalent Organic Framework for Rechargeable Sodium-Ion Batteries

4.1. Introduction

Covalent organic frameworks (COFs) are two-dimensional or three-dimensional porous organic solids with extended structures in which building blocks are connected together by strong covalent bonds.[90,137,138] Due to their programmable architecture, thermal stability, uniform porosity, and structural diversity, COFs have been extensively explored over the past decade in numerous areas such as catalysis[76], gas separation[73,74], drug delivery[75], pseudocapacitors[77,78], proton conduction[79], and energy storage.[80–82] In the latter, 2D COFs take advantage of their semiconductive nature endowed by extended π-conjugated crystalline skeletons and high capacities from accessible built-in redox-active sites. These characteristics of the COFs are important for charge and ionic transportation and restraining dissolution in the electrolyte.[71,72] In the field of energy storage, COFs have been employed as either cathode or anode, as well as solid-state electrolytes in a half cell of metal-ion batteries.[139,140] Besides their use in batteries, COFs are also used as working electrodes in supercapacitors and pseudocapacitors.[141,142]

For the aforementioned applications, controlling the growth rate and structural uniformity of COFs is essential for optimizing performance. Typical synthetic routes of COFs involve connecting organic linkers by reversible bond-forming reactions, allowing error correction processes to form highly ordered frameworks.[138] Although there are very successful synthetic routes for preparing highly crystalline networks, this bottom-up approach becomes very challenging with bulky, rigid

linkers that can impede the reaction kinetics and hinder the growth of desired crystallinity.[98] Recently, a linker exchange mechanism for COFs was reported, which allows the interchange between structural linkers to reconstruct and produce advanced COFs that might otherwise be tedious or challenging via the bottom-up approach. For instance, COF-to-COF transformation by heterogeneous linker exchange and linker substitution has been demonstrated.[143–145] The linker exchange approach is an effective approach for transforming amorphous covalent organic polymers (COPs) into highly crystalline COFs; therefore, can aid in accessing optimized materials for electrochemical energy storage.[146–151] Extending this approach to porous polyimides holds great promise, especially in advanced rechargeable lithium and sodium-ion batteries (LIBs and SIBs) wherein rapid ion and charge transfer and full accessibility of the redox-active sites dictate device performance.[44,152–154] Such properties become even more crucial when sodium is employed because of its large ionic size and sluggish intercalation kinetics.[89] Developing efficient SIBs is highly desirable because sodium is much cheaper than lithium and widely accessible.[18,136,155–157] In recent years, several studies have shown that COFs are promising electrode materials in SIBs with much emphasis on aza and azo-functionalities.[39] However, synthesizing crystalline polyimide COFs remains a challenge limiting their use in rechargeable batteries and other applications.

This work reports the synthesis of a porous polyimide COF (PICOF-1) via linker and linkage exchange using an imine-linked COF (Py-1P COF)[158] as a template and demonstrates its effective use in SIBs. The high porosity and well-defined 1D channels enable fast ion and charge transfer, reaching an excellent specific capacity of 230 mA h g^{-1} and maintaining over 99% coulombic efficiency over 175 cycles at 0.3 C.

4.2. Experimental Section

4.2.1. Materials

1,3,6,8-Tetra(4-aminophenyl)pyrene (TAPP) and Py-1P COF were synthesized according to reported procedures in literature.[159,160] Pyromellitic dianhydride (PMDA) was purchased from a commercial source and used without further purification. Anhydrous N-methyl pyrrolidone (NMP), mesitylene, and isoquinoline were purchased in reagent grade or higher purity from commercial suppliers and were used without further purification. Tetrahydrofuran was freshly distilled from sodium before use.

4.2.2. Synthetic Methods

4.2.2.1. Synthesis of 1,3,6,8-Tetra(4-aminopheny)pyrene (TAPP)

TAPP was synthesized using a modified procedure in literature.[161] 1,3,6,8-Tetrabromopyrene (1.0 g, 1.9 mmol), 4-(4,4,5,5-tetramethyl-1,3,2-dioxaborolan-2-yl)aniline (2.5 g, 11.6 mmol), palladium tetrakis(triphenyl phosphine) (0.12 g, 0.1 mmol), and potassium carbonate (2.1 g, 15.2 mmol) was added to anhydrous dioxane (25 mL) in a Schlenk flask and refluxed with stirring under N_2 for 3 days. The mixture was allowed to cool to room temperature, the product was removed by vacuum filtration, and washed with chloroform and acetone to afford TAPP in 70% yield. ^{1}H NMR (DMSO, 400 MHz): δ (ppm) 8.1 (s, 4H), 7.8 (s, 2H), 7.32 (d, 8H), 6.73 (d, 8H), 5.3 (s, 8H). ^{13}C NMR (DMSO, 400 MHz): δ (ppm) 148.3, 137.6, 131.6, 129.5, 128.4, 127.2, 126.6, 125.0, 114.7.

4.2.2.2. Synthesis of PICOP-1 (Conventional Route)

PMDA (21.8 mg, 0.1 mmol) was charged into a 10 mL round bottom flask with a stir bar. TAPP (28.33 mg, 0.05 mmol) was dissolved in a solution of NMP (0.2 mL), mesitylene (1.0 mL), and isoquinoline (0.1 mL) and was added slowly into the PMDA while stirring under a nitrogen

atmosphere. The solution was stirred overnight at room temperature under nitrogen, after which the mixture obtained was transferred into a pyrex tube. The mixture was degassed by three freeze-pump-thaw cycles and flash-frozen at 77 K using a liquid N_2 bath before flame sealing it under a vacuum. The reaction mixture was then heated at 210°C for 5 days to afford a fluffy brown powder (32.0 mg, 35% yield). Anal. Calcd for $C_{30}H_{13}N_2O_4 \cdot 3H_2O$: C, 69.36; H, 3.69; N, 5.39; O, 21.56. Found: C, 69.46; H, 3.66; N, 5.50; O, 21.38.

4.2.2.3. Synthesis of PICOF-1 via linker exchange. [146]

A pyrex tube was charged with Py-1P COF (60 mg, 1 eq), PMDA (18 mg, 1 eq), benzaldehyde (0.80 mL), NMP/mesitylene (4.00 mL, 1:3 v/v) and isoquinoline (0.20 mL). The mixture was sonicated for 15 min and degassed by three freeze-pump-thaw cycles. The tube was then flash frozen at 77 K using a liquid N_2 bath and then flame sealed under vacuum. The mixture was heated at 160 °C for 5 days. The resulting mixture was filtered and washed with DMF. PICOF-1 was further purified by Soxhlet extraction with THF for 24 h to yield PICOF-1 as a dark orange powder (65 mg, 89% yield based on Py-1P COF). Anal. Calcd for $C_{30}H_{13}N_2O_4 \cdot 2H_2O$: C, 74.53; H, 3.13; N, 5.79; O, 16.55. Found: C, 73.91; H, 4.04; N, 6.02; O, 16.03.
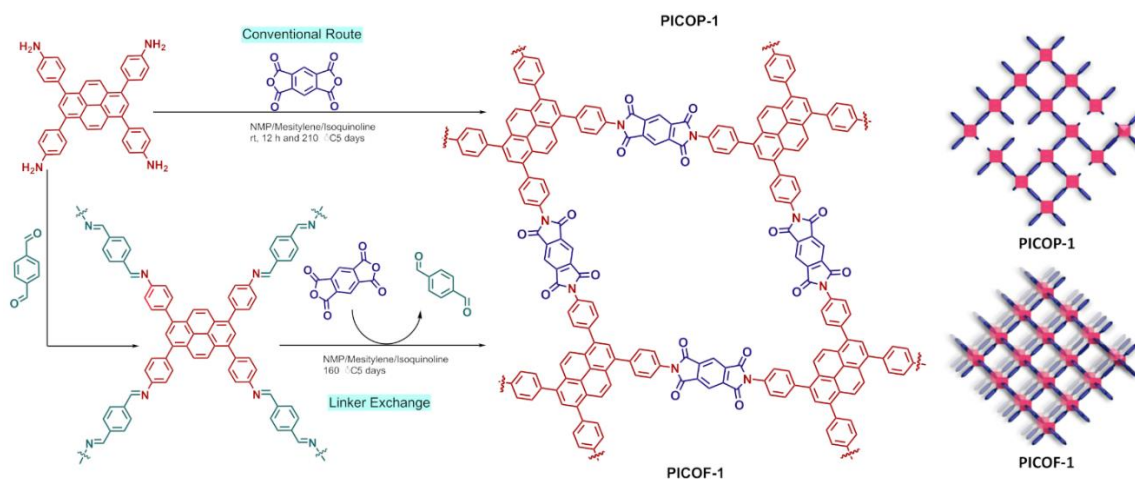
Scheme 4.1 Conventional synthetic route and the alternative linker exchange approach for porous polyimide framework synthesis.

4.2.3. Preparation of PICOP-1 and PICOF-1 Electrodes

Polymer composite electrodes were prepared using 60 wt% active material, 30 wt% conductive carbon (Ketjenblack EC-600JD), and 10 wt% polyvinylidene fluoride in an NMP medium. The resulting slurry was cast onto an aluminum current collector using a doctor blade and dried at 60 °C overnight in a vacuum oven. The dried material was then cut into circular discs of 15 mm diameter, affording an areal mass loading of 0.5 mg.

4.2.4. Physical and Spectral Characterizations

N_2 adsorption/desorption isotherms were collected using 3Flex Surface Characterization Analyzer (Micrometrics) after degassing the samples at 120 °C for 24 hours under a vacuum. Powder X-ray diffraction (PXRD) was carried out using Panalytical Empryrean Diffractometer using Cu Kα radiation (1.54059 Å) at 45 kV and 40 mA. For Scanning Electron Microscopy (SEM) imaging, the samples were prepared by mounting the prepared electrode on sticky carbon attached to the Al sample holder. The samples were coated with platinum at a pressure of 1×10^{-5} mbar in an N_2 atmosphere for 60 seconds before SEM imaging. The images were taken using a Hitachi SU-70 FE-SEM. Ex-situ X-ray photoelectron microscopy (XPS) was carried out using PHI VersaProbe III Scanning XPS Microprobe. Raman spectroscopy was carried out using Thermo Scientific DXR SmartRaman (532 nm) at 5 mW. The structural changes of electrodes on cycling were examined by dismantling the half cells in an argon-filled glovebox using a de-crimping device. The working electrodes were carefully removed and stored under N_2 until ready for examination. Atomic Force Microscopy (AFM) imaging was performed using an Asylum Research MFP-3D AFM (Oxford Instruments, Santa Barbara, CA, USA). Imaging was conducted in a non-contact mode in the air using an AC240 cantilever (Olympus, Japan) with a nominal force constant of 2 nN/nm.

4.2.5. Electrochemical measurements

The prepared PICOP-1 and PICOF-1 electrodes were used as the working electrode in half cells. 1M NaPF$_6$ in diethylene glycol dimethyl ether (DEGDME) was used as the electrolyte (30 μL mg^{-1} of active material), while polypropylene (Celgard 3501, LLC, Corp., USA) was used as the separator. Sodium metal was cut into circular discs (thickness = 0.6 mm) and was used as the counter and reference electrode in these Na cells. CR2032-type coin half-cells were assembled in an argon-filled glovebox using an electric crimper (MTI Corp.). The assembled coin cells were tested using CHI600 electrochemical workstation for cyclic voltammetry (CV) and electrochemical impedance spectroscopy (EIS) measurements. Galvanostatic charge and discharge data were obtained using a battery analyzer (MTI Corp.). All measurements were carried out at room temperature.

4.3. Results and Discussion

The synthesis of PICOF-1 is depicted in Scheme 1. Our initial attempts involved a condensation reaction between pyromellitic dianhydride (PMDA) and 1,3,6,8-tetra(4-aminophenyl)pyrene (TAPP) using conventional solvothermal routes[75,95], which afforded partially crystalline material (PICOP-1) with low surface area. The first step of the imidization reaction was carried out in a solution of N-methylpyrrolidone (NMP), mesitylene, and isoquinoline at room temperature, followed by heating at 210 °C for 5 days to complete the cyclization. Mixed solvents are typically used to control the solubility of the monomers, while the isoquinoline acts as a catalyst to help control the speed of the reactions, while elevated temperatures are needed for thermal ring closure in the second step. FT-IR and PXRD characterizations were carried out to determine the completion of the reaction and the degree of crystallinity, respectively (Figure 4.1). However, this direct synthetic approach produced only semi-crystalline PICOP-1 (35% yield based on PMDA)

owing to the random association of the PMDA molecules with TAPP and the low overall reversibility of the imidization reaction. In addition, ATR-IR showed residual amine sites, a sign of a defective framework (Figure 4.1a).
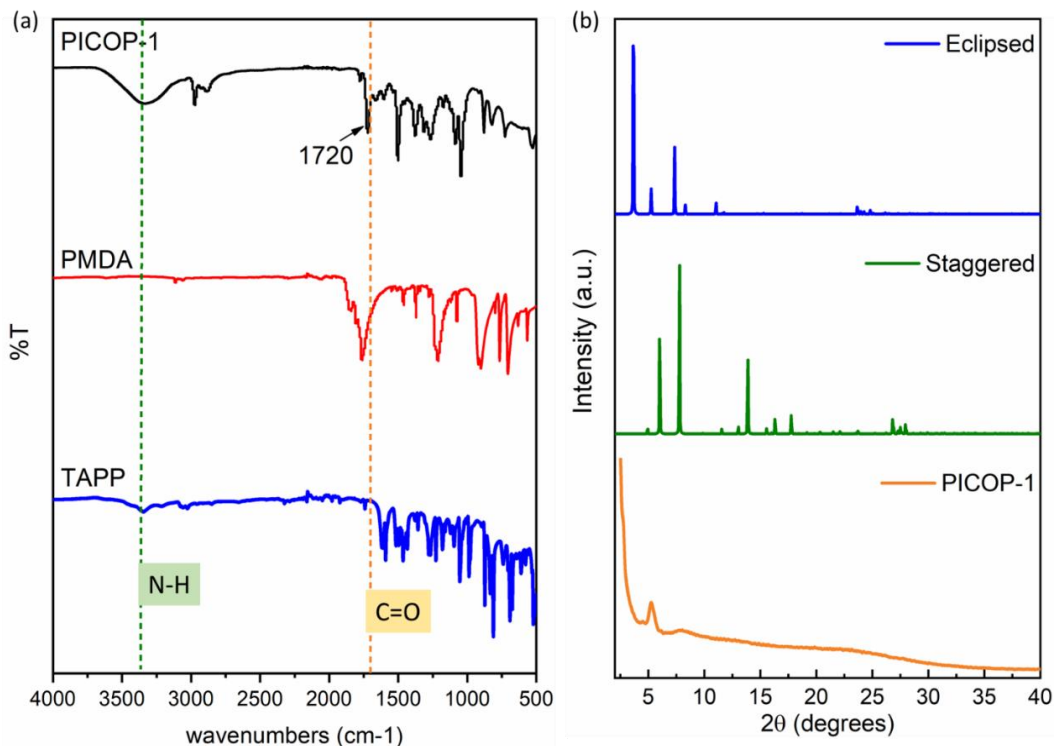
Figure 4.1 FT-IR spectra comparing (a) PICOP-1 and starting materials, (b) PXRD patterns of simulated eclipsed and staggered models in comparison to that of PICOP-1.

To optimize the crystallinity and porosity of the material, a post-synthetic linker exchange-type modification was adopted using Py-1P COF as a template and PMDA as the exchange linker (Scheme 4.1). We envisioned that the preorganized 2D framework of Py-1P COF[41] would direct and facilitate linker exchange with PMDA to produce the desired crystalline PICOF-1. Moreover, the new imide bond is less reversible and more stable than the imine linkage in Py-1P COF, favouring linker exchange and PICOF-1 formation.[24] Indeed, this strategy significantly improved the crystallinity and porosity of the latter. The FT-IR characterization was performed to confirm complete imidization to produce PICOF-1 (Figure 4.2). The peaks at 1780 cm^{-1} and 1720 cm^{-1} of

the PICOF-1 correspond to the asymmetric and symmetric stretching vibrations of the C=O moiety in the five-membered imide ring, respectively (Figure 4.2 a). The peak at 1357 cm^{-1} is due to the stretching vibrations at the C-N-C moiety. Furthermore, the absence of the C=N peak at 1610 cm^{-1} in PICOF-1 confirms the completion of the ligand exchange (Figure 4.2 b). Residual -NH$_2$ (3300 cm^{-1}) and amic acid intermediate (1365 cm^{-1}) were also absent in PICOF-1, in comparison to semi-crystalline PICOP-1 (Figure 4.2 c).
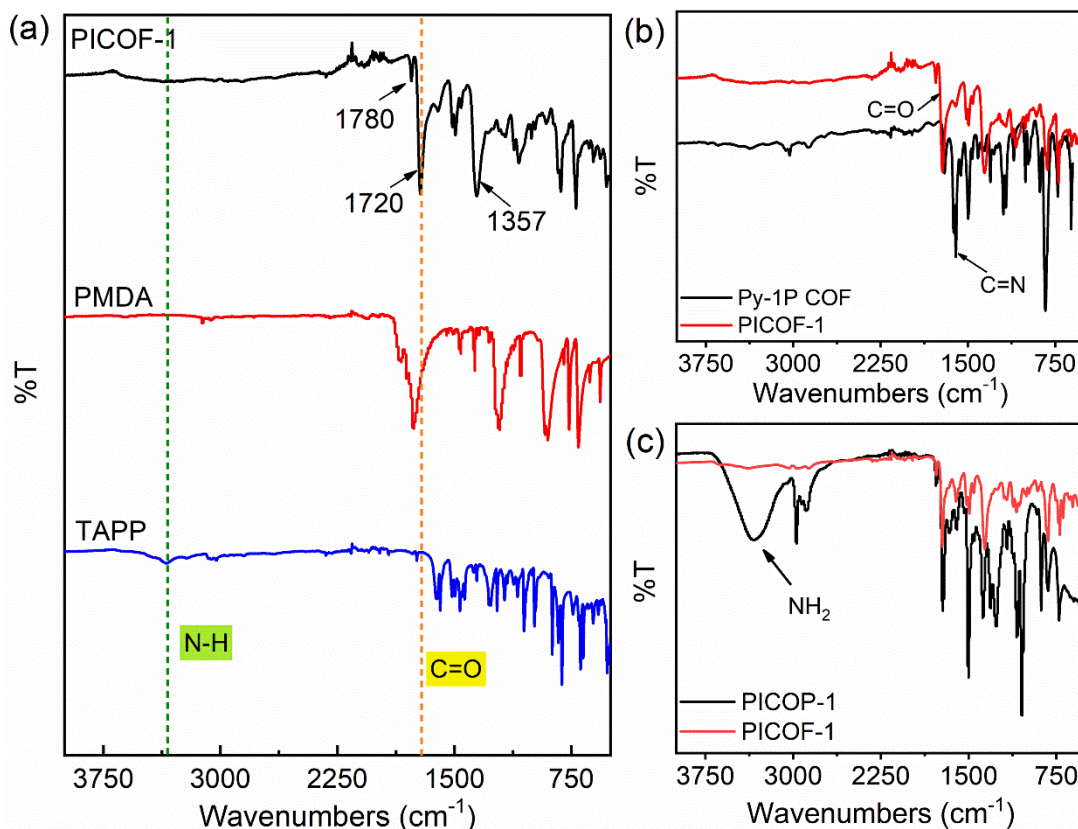
Figure 4.2 FT-IR spectra comparison (a) PICOF-1 and starting materials, (b) Py-1P COF and PICOF-1, and (c) PICOP-1 and PICOF-1.

The ^{13}C cross-polarization magic-angle-spinning (CP-MAS) solid-state NMR spectroscopy of PICOF-1 also confirmed the complete imidization (Figure 4.3). The peak at 165.2 ppm arises from the carbonyl carbon on the imide ring. The overlapping peaks between 115 – 140 ppm can be

attributed to the aromatic C signals. The absence of any peaks around 176 ppm further confirms the absence of amic acid intermediates.[18,162]
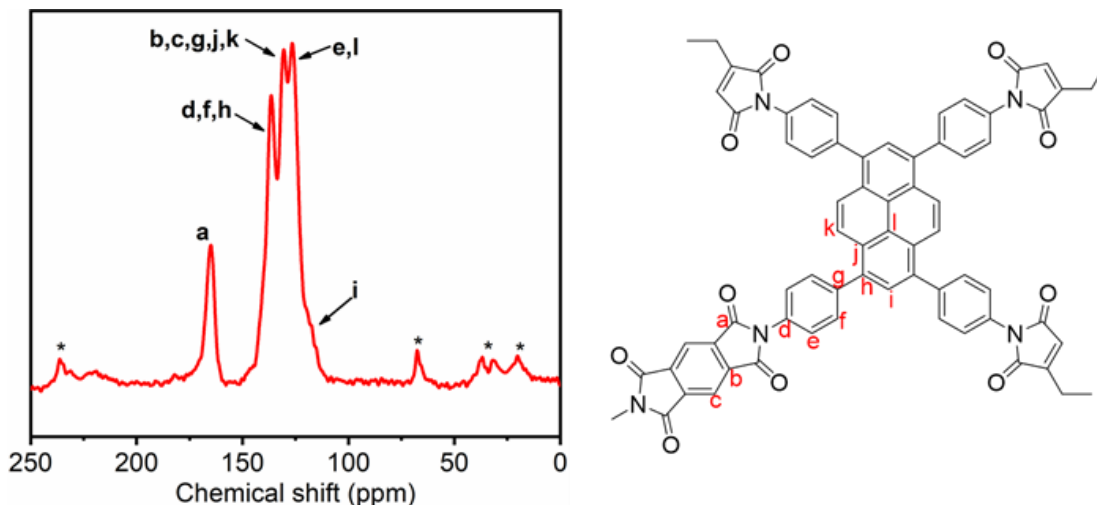
Figure 4.3 Solid-state ^{13}C NMR spectra of PICOF-1. Asterisks (*) indicate peaks arising from spinning sidebands.

The crystallinity of PICOF-1 and PICOP-1 was investigated using the powder X-ray diffraction (PXRD) technique (Figure 4.4 a and 4.1 b). The PXRD pattern of PICOF-1 reveals a highly crystalline material that matches well with the pattern of the predicted eclipsed model with very low refinement parameters R_P and R_{WP} of 0.415% and 0.326%, respectively (Figure 4.4 a), indicating that the extended π conjugation directs the eclipsed stacking of the crystal structure, regardless of the slightly off-rotated phenyl rings in the structure. The intense peaks around 3.6°, 5.3°, and 7.4° correspond to the (110), (200), and (220) planes, respectively. Furthermore, the peak at 23.5° corresponds to the (001) plane, which is related to the interlayer distance between two π-conjugated PICOF-1 layers (0.37 nm) and is in accordance with that of the simulated eclipsed model of PICOF-1 (Figure 4.4 b). However, this behavior was not observed for the material obtained in the conventional synthesis (PICOP-1), which showed very little crystallinity compared to PICOF-1 (Figure 4.1 b). It is assumed that the poor crystallinity of PICOP-1 is due to defective

framework formation (i.e., unreacted sites and missing linkers) promoted by the low reversibility of the imide bond. High-resolution transmission electron microscopy (HR-TEM) was further used to examine the periodicity of PICOF-1, which showed thin sheet-like morphology with a lattice fringe distance of 3.75 Å (Figure 4.4 c) and agrees with the PXRD data and the simulated model.
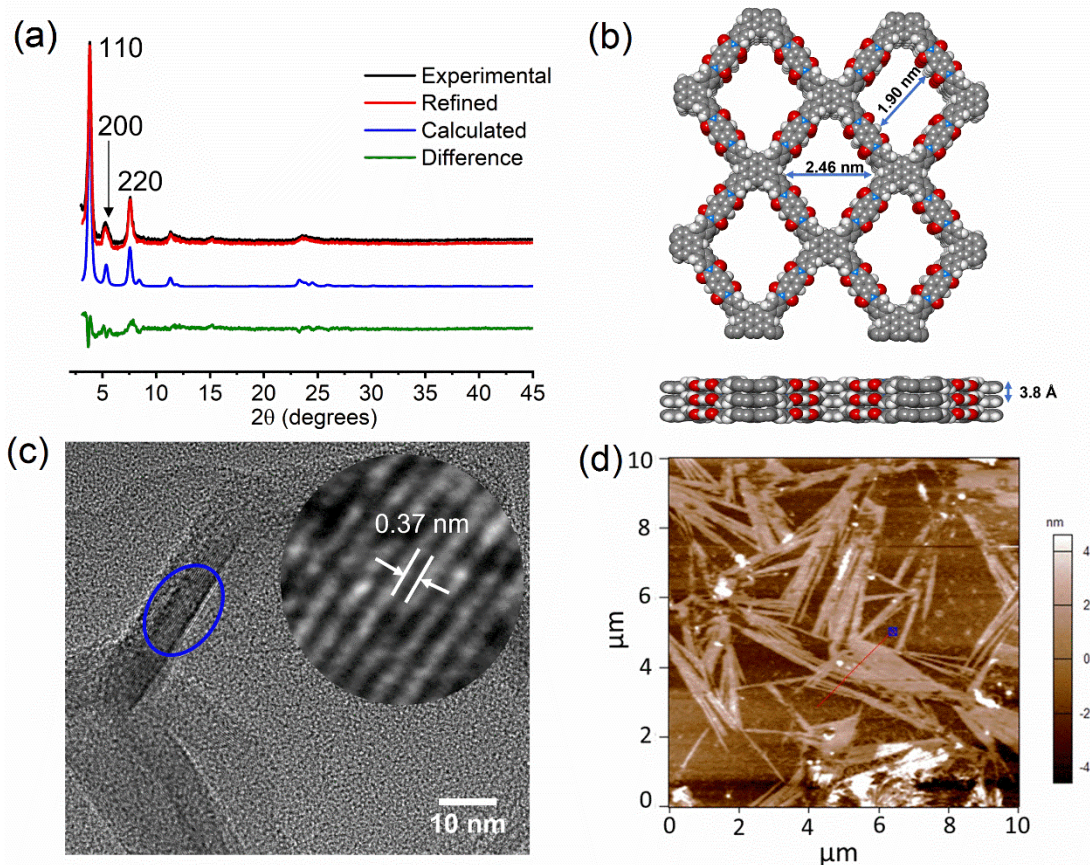
Figure 4.4 a) PXRD patterns of PICOF-1 with the experimental, refined, calculated, and difference profiles ($R_P = 0.415\%$ and $R_{WP} = 0.326\%$), (b) Simulated eclipsed model (C: gray, O: red, N: blue, H omitted for clarity), (c) TEM (inset, d-spacing), and (d) AFM image of PICOF-1.

Another prominent observation that was noticed by HRTEM is the formation of rolled-up sheets giving rise to nanoscrolls (Figure 4.5). This is believed to occur due to the exfoliation of PICOF-1 into single layers during ultrasonication for TEM sample preparation. Instead of remaining flat sheets, the single layers overlap to stabilize the structure. This is a well-observed phenomenon for

highly π-conjugated 2D COFs and is governed by the intermolecular interactions in the overlapped areas.[163,164] Atomic force microscopy (AFM) was utilized to determine the thickness of the 2D sheets of PICOF-1 and was found to be ~3.8, suggesting a thickness of ~10 layers (Figure 4.4 d). AFM also exhibited some nanoscroll formation, as observed in HR-TEM images.
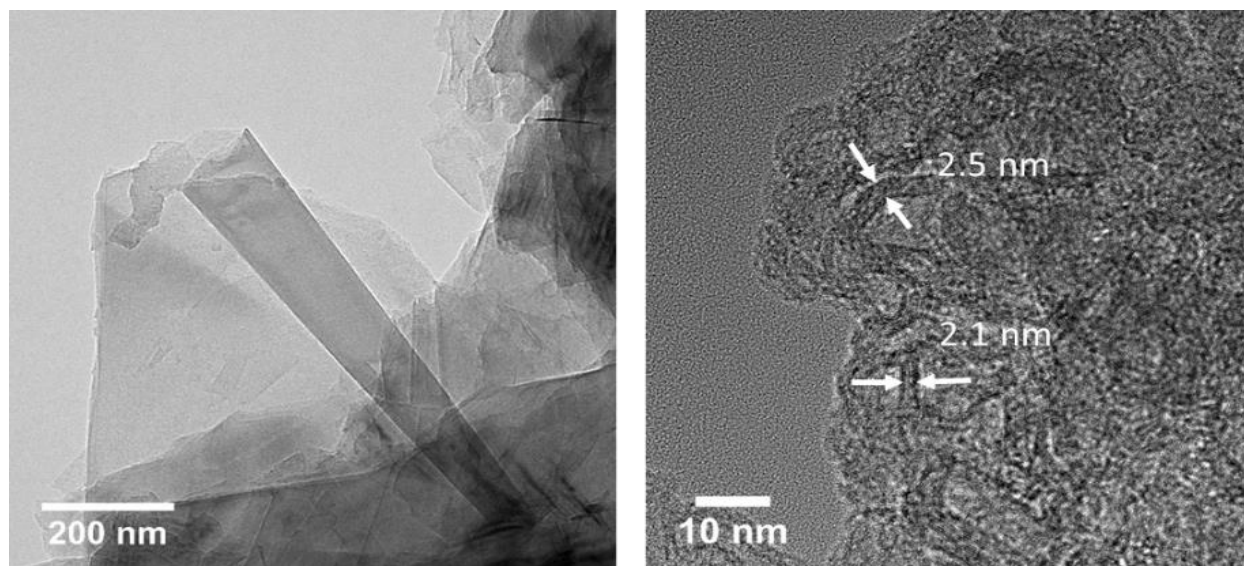
Figure 4.5 HR-TEM images of PICOF-1 showing the nanoscrolls.

The structural morphology of PICOF-1 was also investigated using scanning electron microscopy (SEM), and the images revealed a flaky texture for PICOF-1 with uniform aggregations (Figure 4.6).
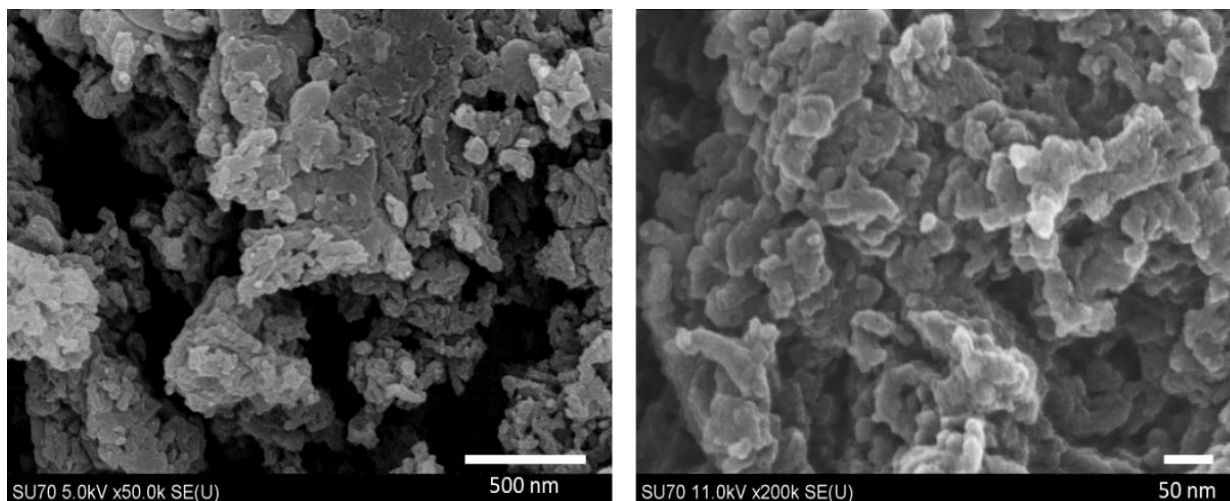
Figure 4.6 SEM images of PICOF-1.

The porosity and surface area of PICOP-1 and PICOF-1 were measured using N_2 adsorption-desorption measurement at 77 K. Both materials show Type I isotherms with a gradual increase in the N_2 adsorption at higher relative pressures (Figure 4.7 a). Steep adsorption at the low-pressure region ($P/P_0 < 0.05$) indicated microporosity. The Brunauer-Emmette-Teller (BET) surface areas of PICOP-1 and PICOF-1 were 510 and 924 m^2 g^{-1}, respectively, and the minor hysteresis shows the adsorbate-induced swelling of the material due to flexibility in the structure.[165,166] The higher porosity of PICOF-1 is due to the more ordered structure giving rise to a higher available surface area, whereas in the semi-crystalline PICOP-1, the overall pore volume and surface area may be constrained by disordered 2D layers and the absence of long-range eclipsed stacking. The NLDFT pore size distribution curve (PSD) for PICOF-1 indicated a dominant pore size of 1.95 nm (Figure 4.7 b) and a nominal pore size of 2.39 nm, which is consistent with the simulated eclipsed model (1.91 nm and 2.78 nm). In contrast, the PSD for PICOP-1 showed a pore size of 1.03 nm owing to the absence of regular pore channels. Thermogravimetric studies (TGA) were also carried out, and PICOF-1 exhibited a very high thermal stability under nitrogen, up to 600 ℃.
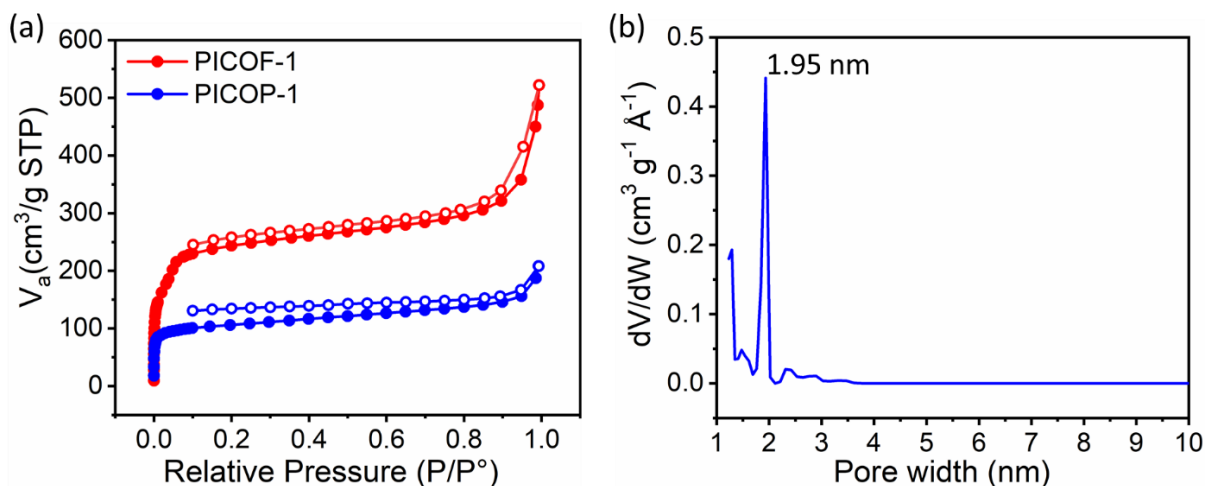
Figure 4.7 (a) N$_2$ adsorption/desorption isotherms of PICOF-1 and PICOP-1 (filled circles represent adsorption and the unfilled circles represent desorption), and (b) PSD of PICOF-1 and the pore size of the simulated eclipsed model (inset).

While several crystalline polyimides are reported in literature, their application in energy storage remains very scarce.[153,154,167] The high crystallinity and porosity of polyimide-COFs, and their redox-active nature, make them good candidates for electrochemical energy storage. Therefore, we studied the application of PICOF-1 for Na ion storage in SIBs. We anticipated the highly π-conjugated PICOF-1 with its large surface area and uniform pore channels to facilitate the flow of electrons and charge more efficiently compared to the irregularly organized PICOP-1. Moreover, the abundant and accessible carbonyl groups in the polyimide framework act as the redox-active sites for charge storage, thereby making this material promising for high sodium storage. Each repeating unit moiety in PICOF-1 consists of 16 redox-active imide sites, which give rise to a theoretical specific capacity (C_{th}) of 230 mA h g^{-1} (Scheme 4.2). Therefore, PICOF-1 electrodes were prepared using PICOF-1 active material, Ketjenblack EC-600JD, and PVDF binder in a 6:3:1 w/w ratio and assembled into CR2032-type coin cells using 1M NaPF$_6$ in DEGDME solvent as the electrolyte solution.
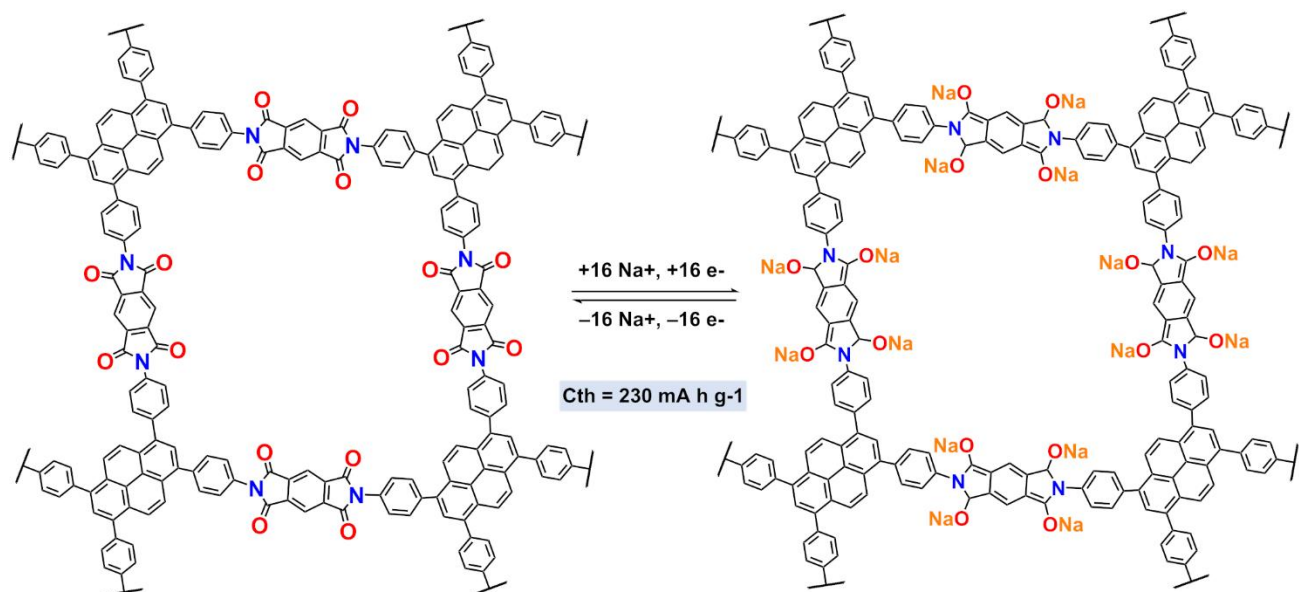
Scheme 4.2 Redox mechanism of PICOF-1 with sodium.

The redox activity of PICOF-1 was first tested using CV studies by cycling the assembled half cells between $0.01 – 3.0$ V at a scan rate of 0.1 mV s^{-1}. The CV displayed four redox peaks where two cathodic peaks centered at 1.20 V (sharp) and 0.80 V (broad). On the other hand, two anodic peaks were noticed at 1.65 V (broad) and 2.23 V (sharp), corresponding to the sodiation and desodiation at the four C=O, respectively (Figure 4.8 a). This is an indication of the full utilization of all carbonyls active sites in the repeating unit. The broad peaks suggest the presence of non-equivalent redox sites on the polymer as well as the surface pseudocapacitive charge storage.[168] This can be confirmed by the CV profiles obtained at different scan rates (Figure 4.8 b), where the ln current increases with the ln scan rate in a linear fashion (Figure 4.8 c). The slopes of the anodic and cathodic curves were 0.7039 and 0.7355, respectively, which suggest that the Na$^+$ ion storage mechanism is governed by both diffusion-controlled faradaic intercalation as well as surface limiting pseudocapacitive process as shown in (Figure 4.8 d).[103,169]
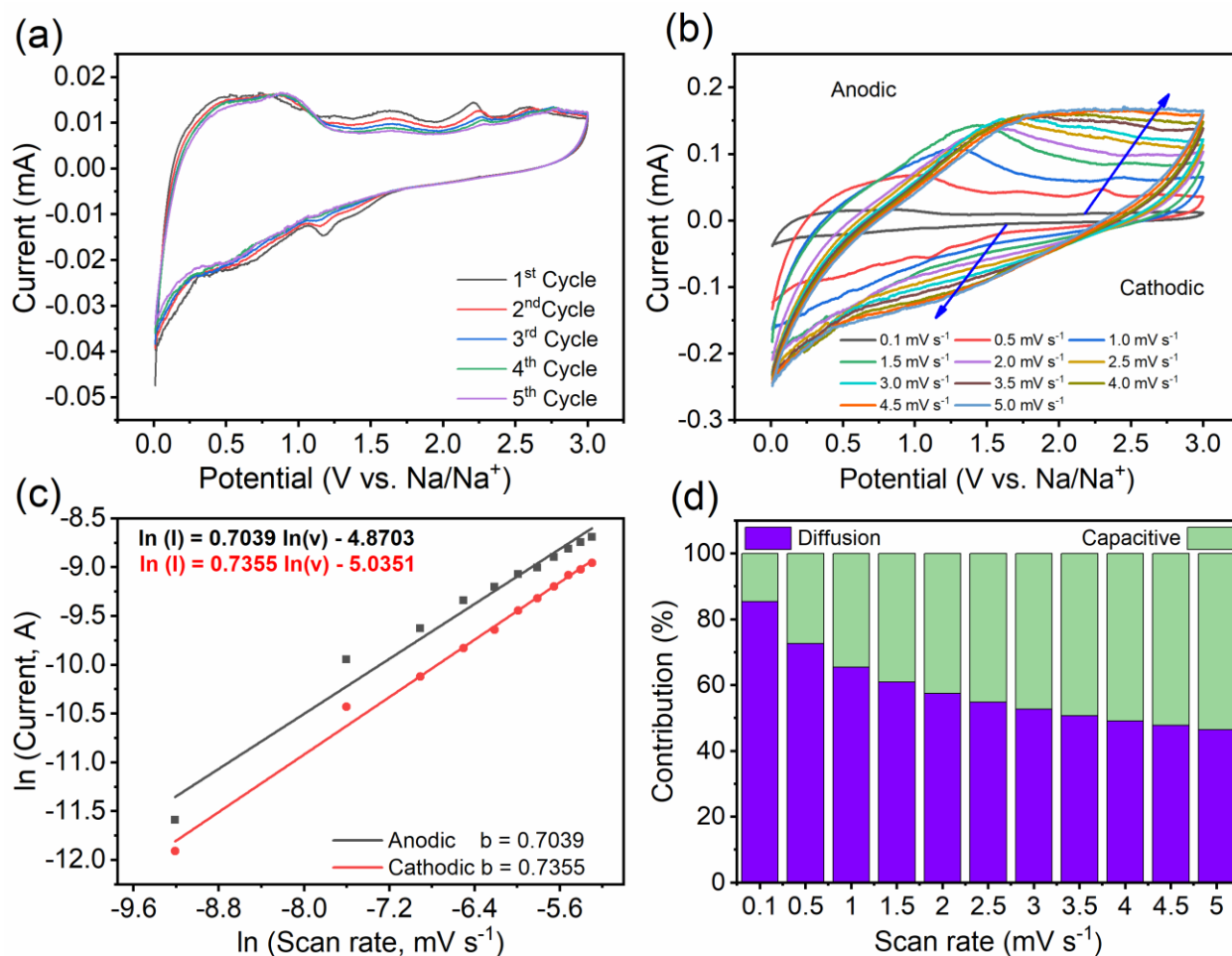
Figure 4.8 (a) CV profiles of PICOF-1 battery at 0.1 mV s^{-1}, (b) CV at different scan rates ranging from 0.1-5 mV s^{-1}, (c) The corresponding linear fit of the ln i vs. ln v (0.1-5.0 mV s^{-1}). (d) the overall total charge storage contribution at different scan rates.

The galvanostatic charge-discharge profiles were collected at 0.1 C in the potential range 0.01 – 3 V vs. Na/Na$^+$ reference electrode, which produced an initial discharge capacity of 237 mA h g^{-1} (Figure 4.9 a). This value corresponds to the sum of the reversible and irreversible capacities resulting from the formation of the solid electrolyte interface (SEI) at the initial cycling steps that involve electrolyte degradation.[169] Thereafter, a reversible capacity of ~ 230 mA h g^{-1} was achieved after the first cycle, which is the same as the theoretical specific capacity of PICOF-1. The sloping charge-discharge curves indicate the presence of complex redox reactions that may arise due to

the repulsion of charges inside the framework, as well as possible pseudocapacitive behavior.[126,153,170] However, the curves are in good agreement with the CV profiles observed with sodiation (reduction) and desodiation (oxidation) (Figure 4.9 b). The rate capability studies were carried out by cycling the batteries at different current rates ranging from 0.1 to 1 C, in the same potential range (Figure 4.9 c). PICOF-1 produced a specific capacity of almost 230 mA h g^{-1} in the first few cycles at 0.1 C. When cycled at higher current rates without relaxation in between, good charge-specific capacities of; 181, 121, and 53 mA h g^{-1} were observed for 0.3 C, 0.5 C, and 1.0 C, respectively. When it was reduced back to the original rate, the specific capacity recovered to 185 mA h g^{-1}, which suggests the structural integrity of the PICOF-1 electrode. However, the sheet exfoliations and the formation of 1D nanoscrolls shown in HRTEM and AFM could reduce the ionic conductivity in the framework by limiting the accessibility of sodium ions to the redox active sites that existed on the exterior side of the nanoscrolls at a higher current rate. On the other hand, the electronic conductivity might be inferior due to the rolling of the exfoliated 2D sheet into 1D nanoscrolls, which limits the charge exchange kinetics in the extended 2D π-conjugated molecule during the sodiation and desodiation process, causing a fair kinetic performance.[19] The long-term cycling stability over 175 cycles of the PICOF-1 battery showed remarkable stability after the first 25 cycles at 0.3 C, with an excellent Coulombic efficiency of nearly 100% (Figure 4.9 d). During the first 25 cycles, the capacity drops quickly from 171 to 95 mA h g^{-1}, then exhibited stable reversible stability with capacity retention reaching up to 84 %.
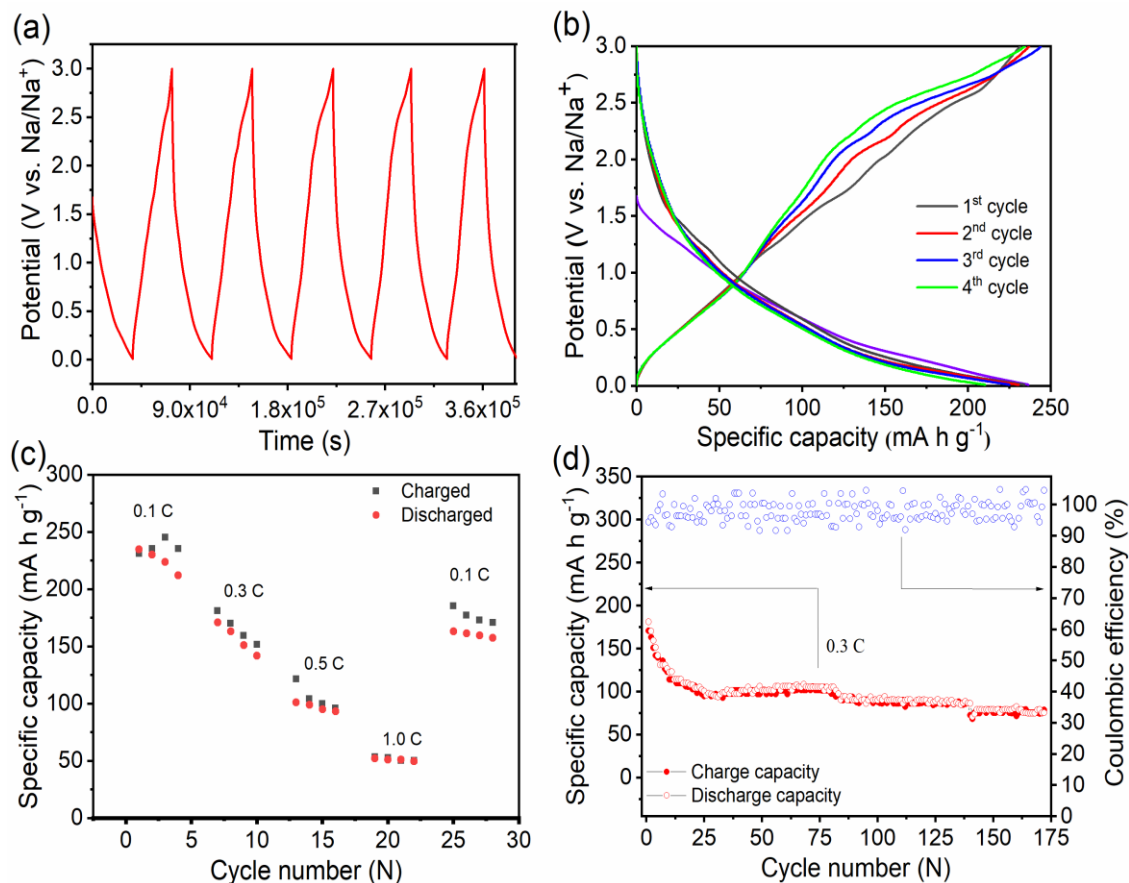
Figure 4.9 (a) Galvanostatic charge-discharge profile at 0.1 C, (b) Charge-discharge curves of potential vs capacity at 0.1 C (c) Rate capability at different current rates, 0.1 – 1.0 C, and (d) Long-term stability and coulombic efficiency at 0.3 C. (1 C = 230 mA g^{-1}).

For comparison, galvanostatic cycling studies of PICOP-1 at 0.05 C showed a charge/discharge hysteresis with over 150% Coulombic efficiency (Figure 4.10 a). This implies a disparity in the charge flow in and out of the semi-crystalline network and, therefore, an irreversible loss of Na into the electrode. In addition, the charge and discharge capacities of 41 and 63 mA h g^{-1} were recorded, respectively, after 25 cycles, corresponding to over 50% loss in performance. Rate capability studies of PICOP-1 also showed an unsteady performance with considerable charge/discharge hysteresis (Figure 4.10 b). These results clearly demonstrate the superior

performance of PICOF-1 due to its optimized crystallinity and porous properties compared to PICOP-1.
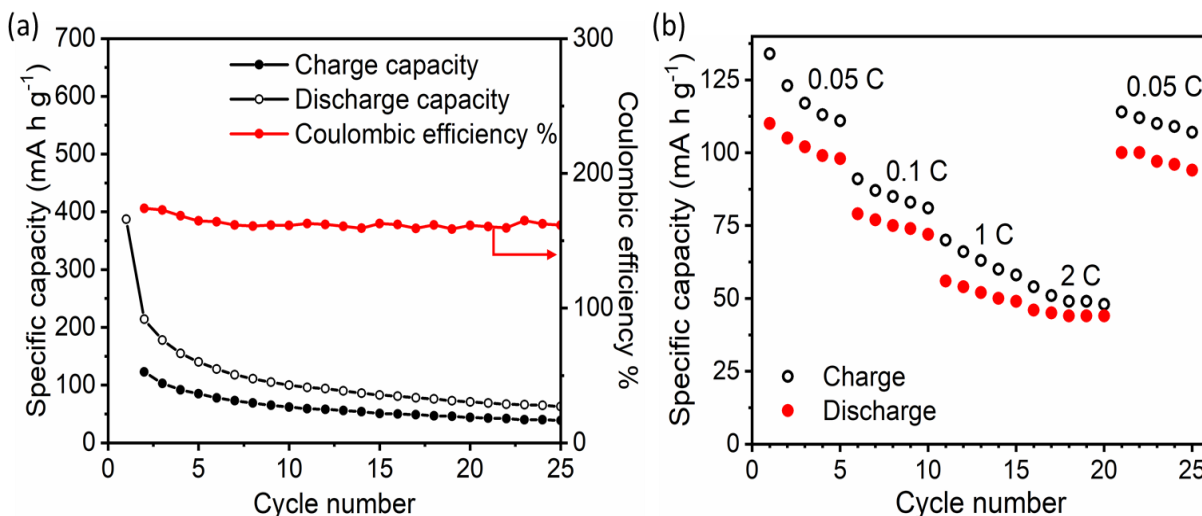
Figure 4.10 (a) Galvanostatic charge-discharge profiles of PICOP-1 at 0.05 C, and (b) Rate capability studies at different current densities for PICOP-1.

Electrochemical impedance spectroscopy was done for both pristine and cycled PICOF-1 electrodes in a frequency range from 0.01 Hz to 1 MHz with 5 mV amplitude. The Nyquist plot for uncycled fresh battery showed a semicircle with charge transfer resistance (R_{ct}) of 60.32 Ω and total internal resistance (R_{in}), including the electrolyte resistance of 10.37 Ω (Figure 4.11 a). On the other hand, the Nyquist plot for the PICOF-1 electrode after being cycled for 220 cycles exhibited R_{ct} and R_{in} of 532.4 Ω and 8.763 Ω, respectively (Figure 4.11 b). A bigger R_{ct} for the cycled battery might be attributed to the partial decomposition of the electrolyte and the formation of organic and inorganic salts upon cycling, which might block the channels and reduce the ion mobility in and out.[171]
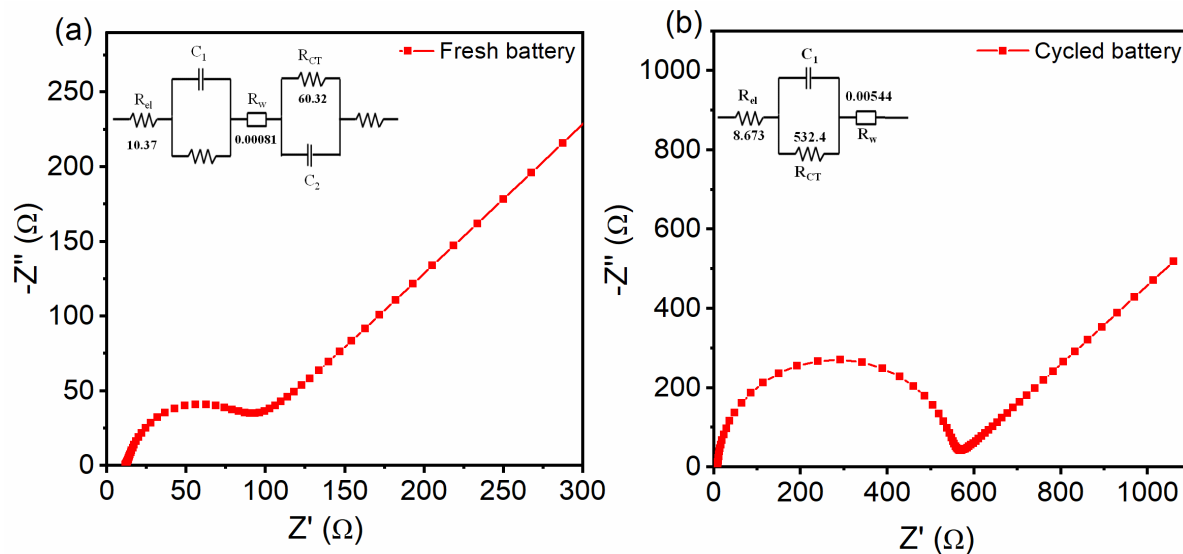
Figure 4.11 Electrochemical impedance spectroscopy for (a) a freshly prepared battery and (b) a cycled battery after 220 cycles. The insets are the Randles' equivalent circuits.

Ex-situ XPS analysis was employed to further study the electrochemistry in the PICOF-1 battery. The C 1s peak at 284.4 eV was used as the reference peak to correct all binding energies for XPS analysis (Figure 4.12). The distinct asymmetry of the C 1s spectra towards the higher binding energies shows the high density of sp^2 carbon in the material.[131] The C 1s XPS spectrum for pristine electrode produced peaks corresponding to PICOF-1, PVDF binder, and adventitious carbon (Figure 4.12 a). The peak at 287.6 eV corresponded to the C=O functionality of the imide group and was used as a guide to study the reversibility of the sodium storage mechanism in PICOF-1. During discharging, the C=O peak disappeared, and a new peak at 286.2 eV, corresponding to C-O, appeared (Figure 4.12 b). This illustrates the reduction taking place during discharge at the imide. When recharged to 3 V, the C-O peak disappeared while the C=O peak reappeared (Figure 4.12 c). Survey spectra of the electrodes at different stages of charge show the appearance of Na 1s peaks during discharge (Figure 4.12 d). The Na 1s peak in the recharged electrode comes from the sodium in the SEI formed during the initial cycling stages.
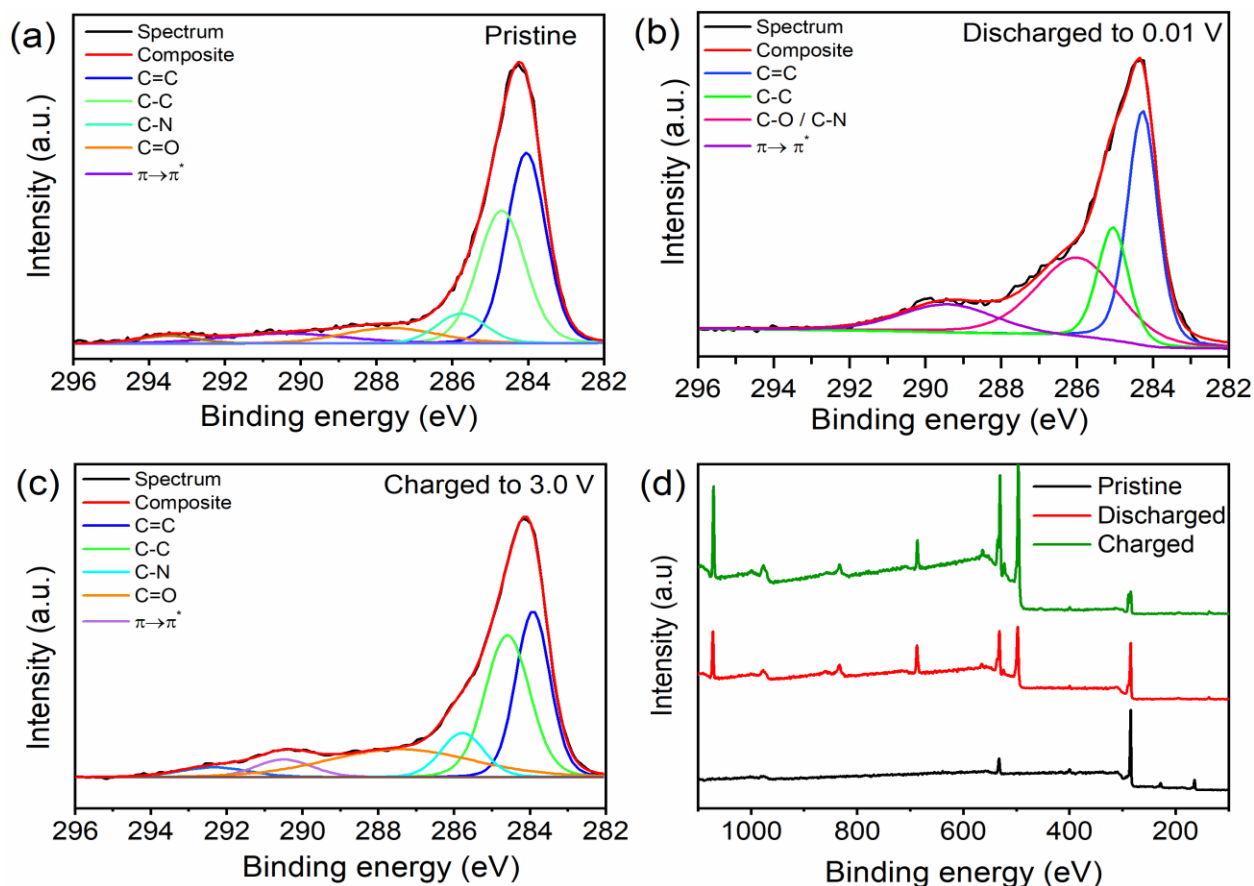
Figure 4.12 Deconvoluted C 1s XPS spectra of (a) Pristine, (b) Discharged electrode to 0.01 V, (c) Recharged PICOF-1 electrode to 3 V, and (d) Survey spectra.

Raman spectra (Figure 4.13 a) show a D band at 1356 cm^{-1} and a G band at 1591 cm^{-1} for pristine PICOF-1 electrode, which demonstrates some disorder in the sp^2 structure. In comparison to the Raman spectrum of PICOF-1 ($I_D/I_G = 0.03$, Figure 4.13 b), this disorder can be attributed to the presence of conductive carbon and binder material in the composition of the electrode.[133] However, the Raman spectra of the discharged and charged electrodes produced similar D and G bands with constant relative intensities ($I_D/I_G = 0.8$), further confirming the high structural integrity of the electrode material and the ability to hold its 2D π-conjugated structure with open channels during the electrochemical insertion and extraction of Na$^+$ ions. The peak at 1150 cm^{-1} in Figure 4.13 b corresponds to the C-N-C axial vibration stretch.[172]
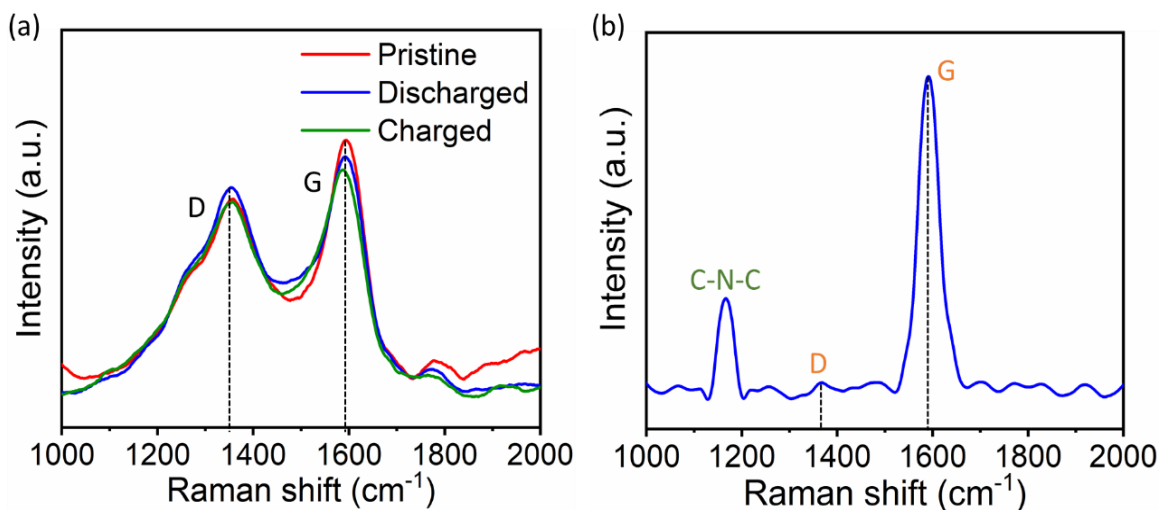
Figure 4.13 (a) Raman spectra of PICOF-1 electrode at different states of charge and (b) Raman spectrum of PICOF-1.

4.4. Conclusion

In summary, we synthesized a crystalline highly conjugated pyrene-based polyimide PICOF-1 using linker exchange-based post-synthetic modification of imine-linked Py-1P. This synthetic route was effective in forming a highly crystalline porous polyimide framework. The high surface area coupled with the well-defined pore structure effectively uses Na^+ ion storage via both faradaic intercalation and pseudocapacitive storage. At low C rates, all carbonyl redox active sites were utilized efficiently during the charge and discharge process, which maximizes the specific capacity to approach the theoretical capacity based on eight redox-active sites per repeating unit. High-resolution TEM and AFM studies indicate the formation of thin layers reorganizing into nanoscrolls of about 4 nm in diameter. According to rate capability studies, such morphology seems to impede the accessibility of the redox active sites at high C rates. Therefore, the current study demonstrates that polyimide COFs have the potential to address the shortcomings of

electrode materials in SIBs. However, control over morphology is needed to fully exploit the potential of this class of COFs in rechargeable batteries.

Chapter 5. Synthesis of Multifunctional Benzimidazole Linked Polymer for Energy Storage Applications

5.1. Introduction

Covalent organic frameworks (COFs) are crystalline organic polymers built by connecting selected organic building blocks with strong covalent bonds.[90,137,138] The structural and chemical composition of the COFs can be perfectly designed and tailored to suit many different applications and uses such as electrochemical energy storage[30,39,113,114], drug delivery[75,173], gas separation and storage[73,112], and catalysis[76,174]. For instance, COFs have shown great promise in supercapacitors[117,141], pseudocapacitors[30,39,78] and rechargeable batteries[142,175–177]. The highly cross-linked nature of the networks prevents its breakdown in electrolytes. On the other hand, the highly eclipsed porous channels and the π-conjugated in 2D backbones secure sufficient pathways for ion movement back and forth to the dense redox active sites and facilitate charge transfer along the 2D network. Furthermore, bigger pores endow a chance to reversibly accommodate bigger metal ions to be utilized rather lithium, such as sodium and potassium[89], making them very wanted electrode materials in green batteries. Part of the COFs family, Benzimidazole Linked Polymers (BILPs) have emerged widely in many applications. BILPs are extended heterocyclic aromatic organic compound polymers, which are synthesized by a polycondensation reaction. The synthesis of different BILPs and their applications in the field of proton conduction[94], solid state electrolyte for lithium-ion batteries (LIBs)[178], and gas capture and storage[73,93] were reported in the literature. BILPs can be designed and synthesized by increasing the redox active sites per repeating unit to be used as efficient materials for metal-ion rechargeable batteries. Up to the best of our knowledge, BILPs was utilized in LIBs as a solid-state electrolyte. However, using BILPs as a cathodic material in a half cell battery hasn't been addressed yet.

Nowadays, LIBs are extensively used as a power supply for electric vehicles, portable electronics, and grid-scale energy storage systems because of the high specific energy and long-term cycling stability performance.[179] However, lithium's cost and limited resources geographically make it vital to consider more sustainable alternatives to replace LIBs.[85,180] Therefore, some of abundant metals like sodium[19,30,39,157,181,182], aluminum[183], potassium[86,184] and magnesium[185] have been utilized as replacements of lithium as an anode in batteries. Among these options, rechargeable sodium ion batteries (SIBs) have grabbed attention for electrical energy storage and smart grid due to low cost, the abundance of sodium, and competing performance with LIBs.[115] Organic materials have been utilized to advance SIBs due to the natural abundance, ease to design, environmentally green, low cost, , and lightweight which is essential for high gravimetric capacities.[8,12,13,15,26,135] In addition, the excellent structural, versatility and flexibility of organic materials give rise to be perfectly designed at the molecular level to afford different redox active sites (N=C, N=N, and C=O), uniform pore size, high surface area, high order π-conjugated frameworks, and low HOMO-LUMO gap.[16,137] As a result, many potential organic materials have been examined in electrodes, encompassing traditional conducting polymers[186], organic carbonyl frameworks[30,150,151], organosulfur compounds[140,187], organic radical compounds[18,162,188], azo compounds[22,81,157] and polymeric Schiff base.[21] However, some of inherent issues are accompany with organic compounds such as break down in organic electrolytes, inferior electronic conductivity, defects in the π-conjugated frameworks and little redox stability.[25,26] These kind of hurdles could be addressed by the reticular chemistry of COFs.[189] This strategic synthetic methodology allows inserting more dynamic reversible redox-active sites into highly ordered, crystalline, and porous π-conjugated frameworks which enhance the ion diffusion, ion mobility and thereby increase the electronic conductivity. Also, incorporating the conductive material to a backbone (C black) while

using polymeric materials with extended π-conjugation could lower the solubility of the composite in the organic electrolyte.[27,28]

Herein the overarching goal of this project is to establish the use of porous and redox-active Benzimidazole Linked Polymer (BILP) developed in our laboratory as highly efficient green electrodes for SIBs for the first time. BILPs are synthesized from condensation of aryl-hexamine monomers, and terephthalaldehyde to afford a decorated nine aza bonds (-N=C-) undergo reversible redox reactions with sodium. Our work demonstrates the effectiveness of BILPs in SIBs that exhibit high initial specific capacity and good recyclability range and compete with the best performing organic electrodes in the field. As a result, this work will provide fundamental insight into the structure-function relationship of BILPs in electrochemical energy storage and provide new materials for sustainable and efficient batteries.

5.2. Experimental Section

5.2.1. Materials

The chemicals used were purchased from commercial suppliers and all utilized without further purification. 1,2-diaminobenzene (Alfa Aesar, 98%), benzenesulfonyl chloride (Alfa Aesar, 98%), pyridine (Sigma-Aldrich, 99+), Palladium on activated carbon (Pd/C, Acros Organics, 10% Pd) Hexaketocyclohexane octahydrate (HKH·8H$_2$O, Fisher Scientific, 97%), sulfuric acid (H$_2$SO$_4$, Fisher scientific, 94-98%), diethylene glycol dimethyl ether (DEGDME, Sigma Aldrich, anhydrous 99.5%), N–methyl–2–pyrrolidinone (NMP, ACS grade, Alfa Aesar, 99%), electro conductive carbon black (Ketjenblack-600JD), sodium hexafluorophosphate (NaPF$_6$, Alfa Aesar, 99+%), sodium alginate (Alfa Aesar, high viscosity).

5.2.2. Synthesis of the Building Blocks, monomer and Aza-BILP

The building blocks in the reaction scheme 5.1 below were synthesized based on literature with modifications[190–193]
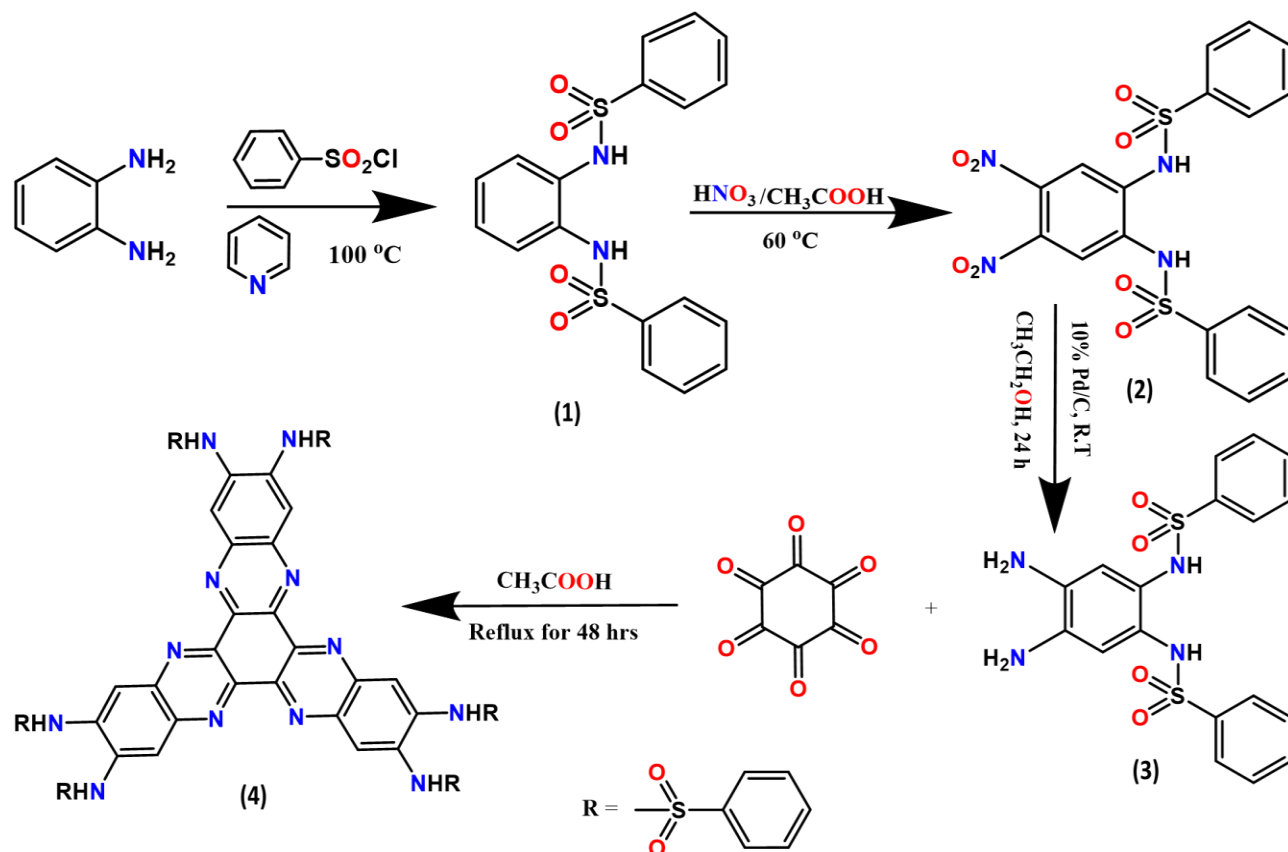
Scheme 5.1 Step-by-step synthesis of the building blocks.

5.2.2.1. 1,2-Bis-(phenylsulfonamido) benzene[190] (1)

20 g of 1,2-diaminobezene (185 mmol) and 65 ml pyridine were charged in 250 ml 2-neck flask under nitrogen. A solution of 47.20 ml benzenesulfonyl chloride (370 mmol) and 10 ml pyridine was added slowly into the flask. The solution mixture was heated for 5 hours at 100 °C under nitrogen. Pour the solution into 250 ml water and stir it for 30 seconds to get pale yellow precipitate. The crude product was recrystallized with ethyl acetate by slow evaporation at room

temperature to afford off-white crystals and then dried at 110 °C. (>90% yield) ATR-IR; 3272 cm$^-$

^{1} for (NH), 3070 cm^{-1} for (=C-H), 1597 cm^{-1} for (C=C), 1153 and 1331 cm^{-1} for (S=O).^{1}H NMR

(400 MHz, DMSO-d6) δ 6.986 (t, 2H), 6.989 (t, 2H), 7.55 (t, 4H), 7.66 (t, 2H), 7.72 (d, 4H), 9.35

(s, 1H); ^{13}C NMR δ 123.91, 126.39, 127.31, 129.79, 130.17, 133.72, and139.48 ppm. (Scheme 5.2
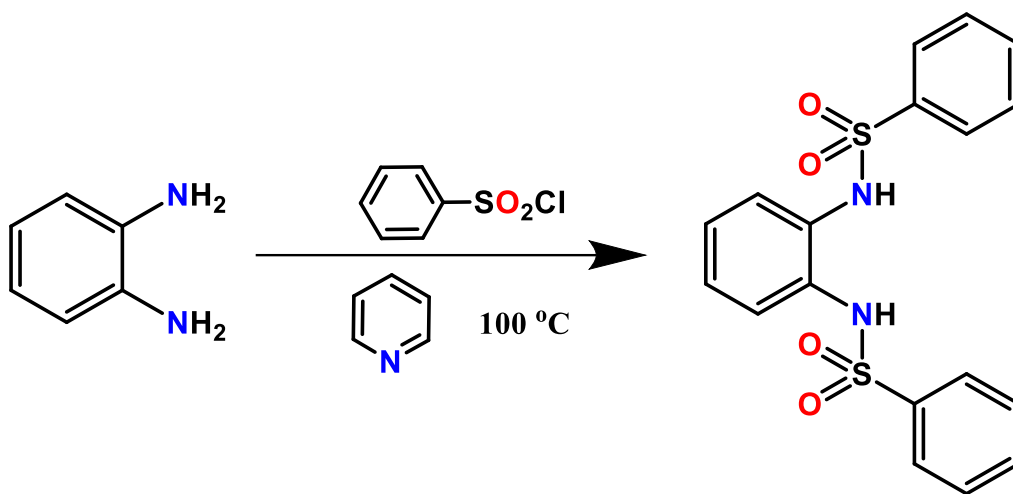
Scheme 5.2 The synthesis of 1,2-Bis-(phenylsulfonamido) benzene from 1,2-diaminobenzene
(1).
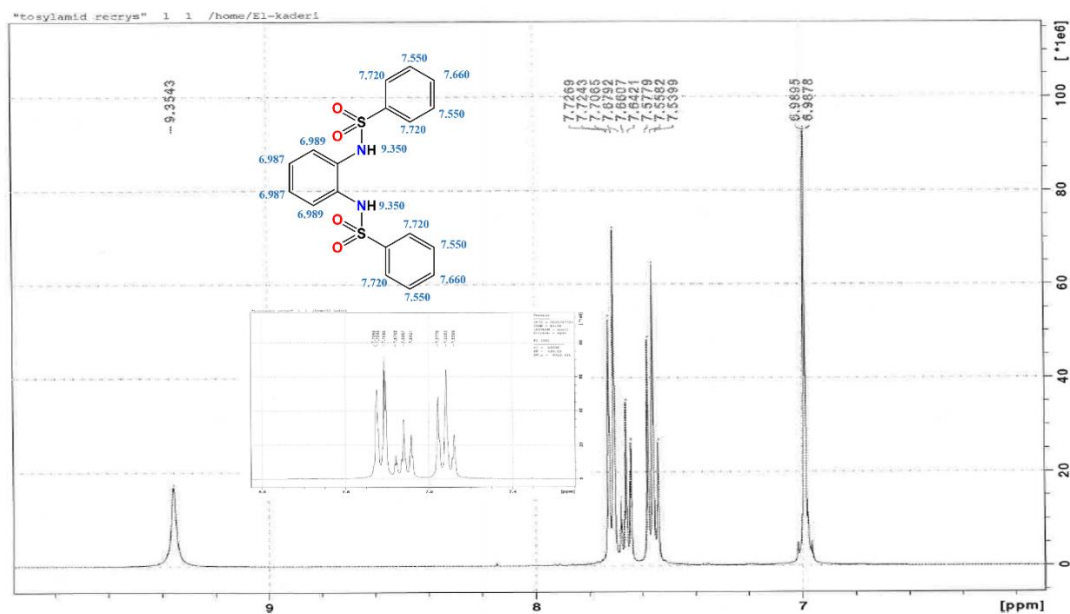
Figure 5.1^{1}HNMR of 1,2-Bis-(phenylsulfonamido) benzene **(1)**.
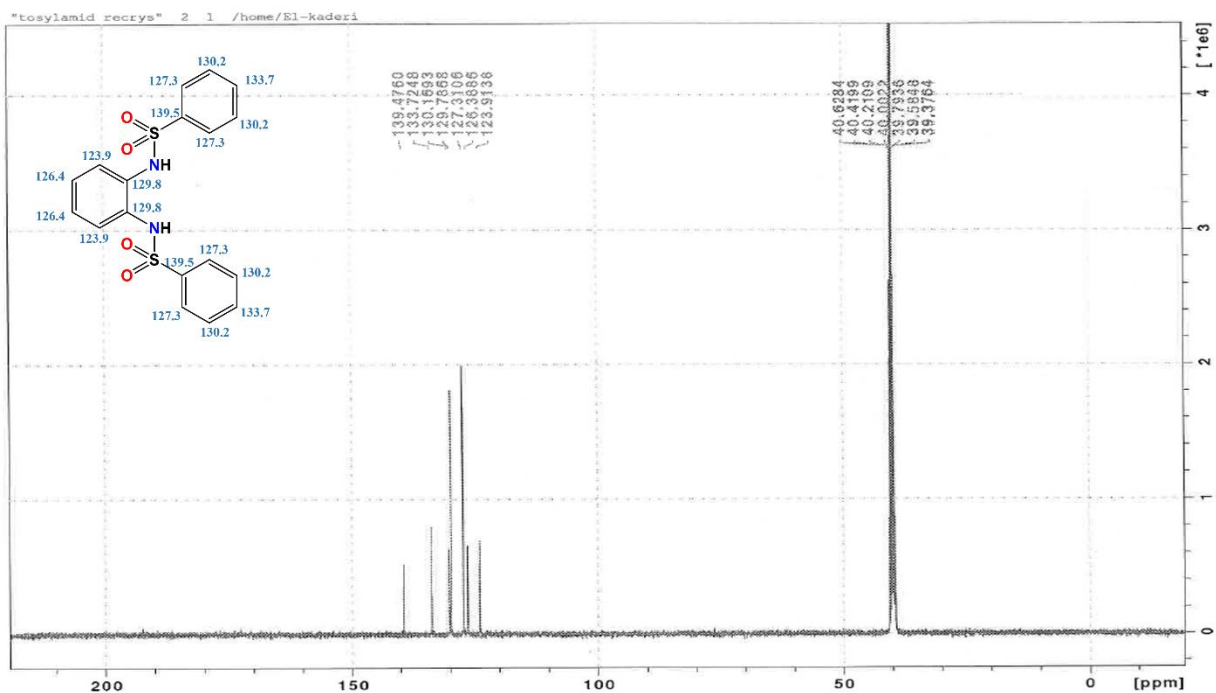
Figure 5.2 ^{13}CNMR of 1,2-Bis-(phenylsulfonamido) benzene (**1**).
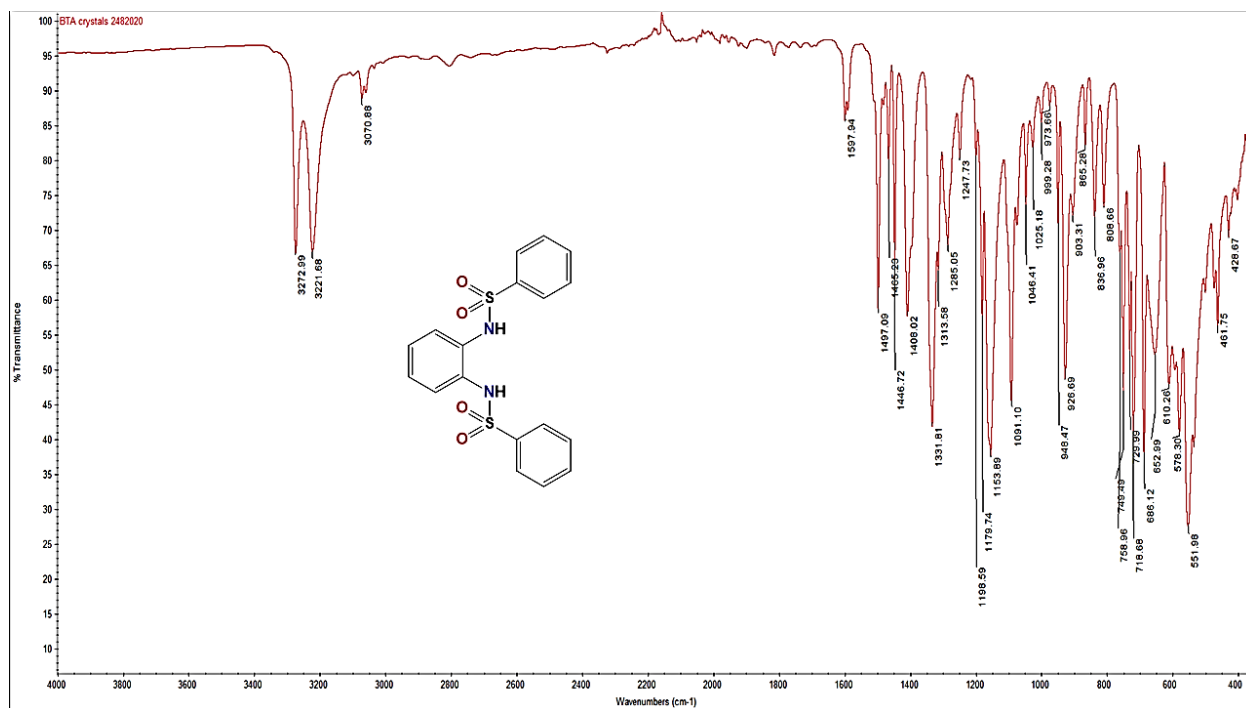
Figure 5.3 ATR-IR of 1,2-Bis-(phenylsulfonamido) benzene (**1**).

5.2.2.2. 1,2-Bis-(phenylsulfonamido)-4,5-bis-nitrobenzene[191] (2)

20 g of 1,2-Bis-phenyl-sulfonamido-benzene (51 mmol) was put in a 500 ml two-neck flask, and 175 ml CH_3COOH was added. Then a mixture of acids (6.00 ml fuming HNO_3 and 7.00 ml CH_3COOH) was added dropwise at 60 ^oC while stirring. After the addition was completed, the mixture solution was reacted again for 30 minutes at 60 ^oC, cooled, filtrated, and obtained shallow yellow solid. The product was washed with acetic acid, recrystallized from ethanol by slow evaporation at room temperature to afford off-white needle crystals, and dried in the oven at 110 ^oC; ATR-IR; 3265 (NH), 3071 cm^{-1} (=C-H), 1593 cm^{-1} (C=C)1357 and 1529 cm^{-1} (NO_2), 821 cm^{-1} (Ar-NO_2), 1163 and 1331 cm^{-1} (S=O).^{1}HNMR (400 MHz DMSO-d6), 8.83 (s, 2H), 7.79 (d, 4H), 7.73 (s, 2H), 7.67(t, 2H), 7.57 (t, 4H); ^{13}C NMR δ 115.80, 127.23, 127.31, 129.99, 133.98, 134.92, 137.15 and 139.64 ppm.
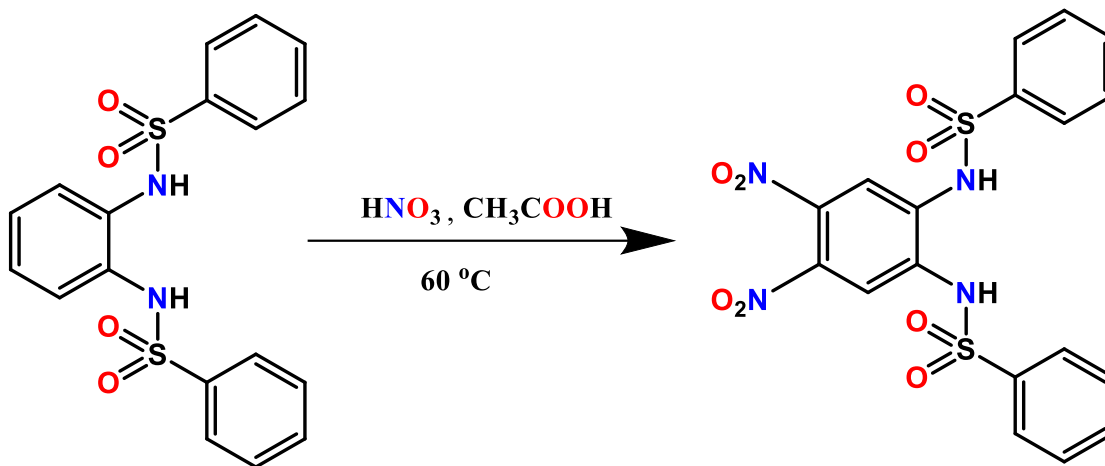
Scheme 5.3 The synthesis of 1,2-Bis-(phenylsulfonamido)-4,5-bis-nitrobenzene (2).
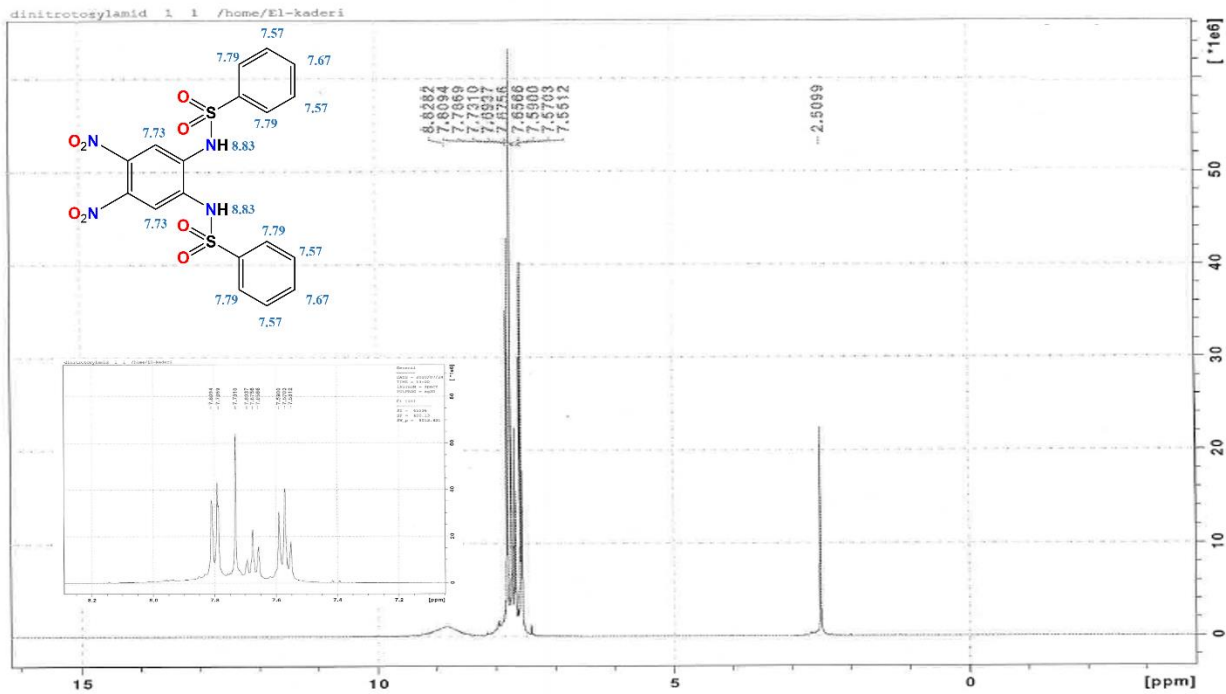
Figure 5.4 ^{1}HNMR of 1,2-Bis-(phenylsulfonamido)-4,5-bis-nitrobenzene (**2**).
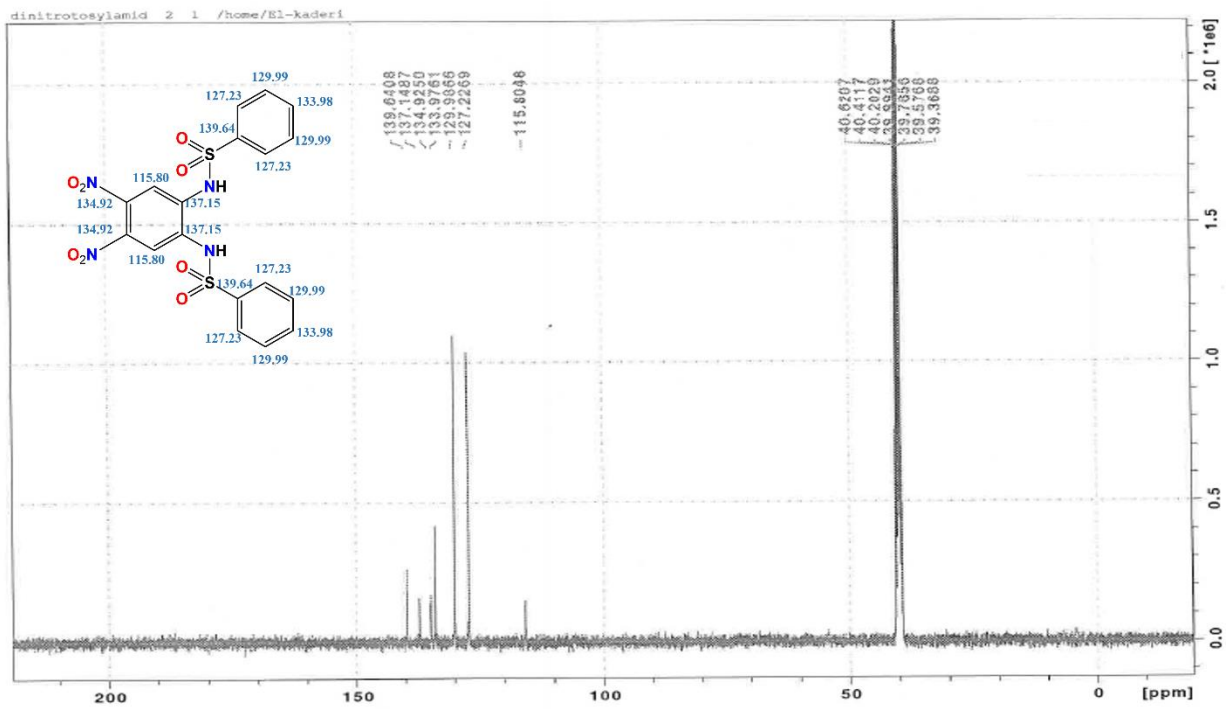
Figure 5.5 ^{13}CNMR of 1,2-Bis-(phenylsulfonamido)-4,5-bis-nitrobenzene (**2**).
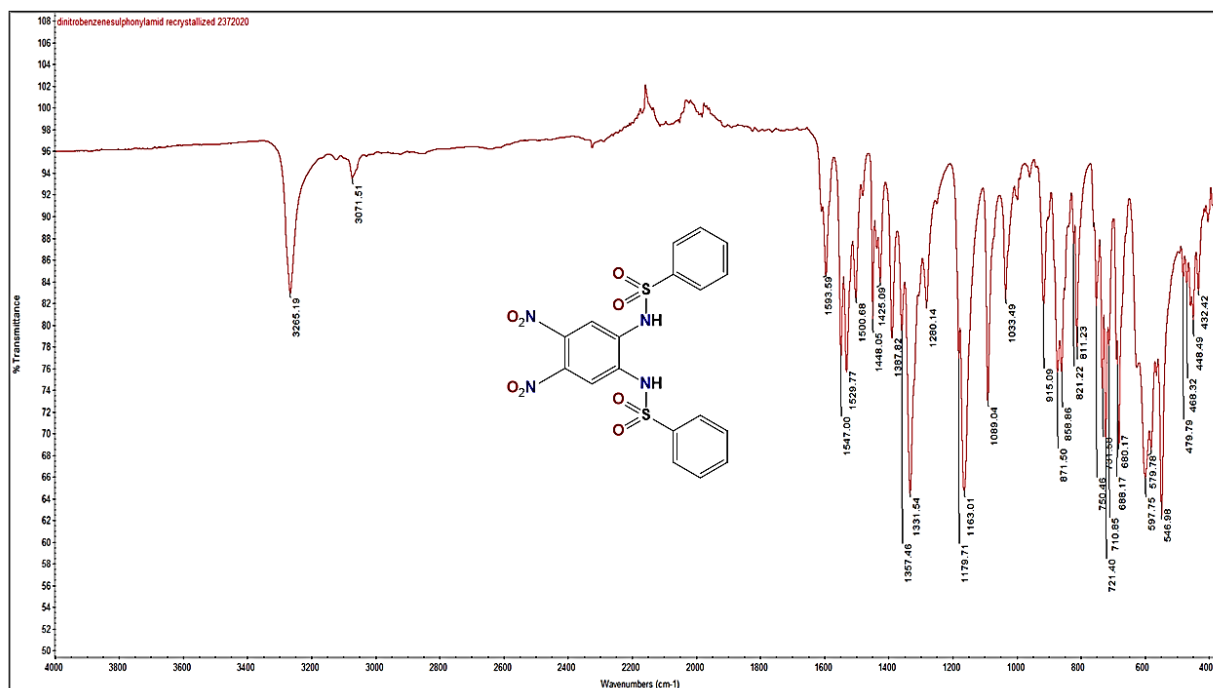
Figure 5.6 ATR-IR of 1,2-Bis-(phenylsulfonamido)-4,5-bis-nitrobenzene (**2**).

5.2.2.3. 1,2-Bis-(phenylsulfonamido)-4,5-bis-aminobenzene[192] (3)

A high-pressure vessel reactor was charged with 5.0 g of N,N'-(4,5-Dinitro-1,2-phenylene)dibenzenesulfonamide (10.5 mmol), 60.0 ml ethyl acetate, 60 mg 10% Pd/C powder, and a stir bar. H_2 gas at high pressure (60 psi) was provided to the vessel, and the mixture was under stirring for 24 hours at room temperature. The mixture was filtered using a frit funnel and washed with boiling ethanol (2x100 ml each), and the filtrate was let to cool down at room temperature and then in an ice bath to afford offwhite crystals (yield >90%). ATR-IR; 3270 (NH, sulfonamide), 3367 and 3436 cm^{-1}(NH$_2$ symmetrical and asymmetrical stretching), 3071 cm^{-1} (=C-H), 1629 cm^{-1} (C=C), 1158 and 1323 cm^{-1} (S=O).1H NMR (400 MHz, DMSO-d6) δ 4.53 (s, 2H), 6.13 (s, 2H),7.53 (t, 4H), 7.62 (t, 2H), 7.64 (d, 4H), 8.57 (s, 2H); ^{13}C NMR δ 111.34, 120.43, 127.32, 129.47, 133.28, 134.22, and 139.61 ppm.

Scheme 5.4 The synthesis of 1,2-Bis-(phenylsulfonamido)-4,5-bis-aminobenzene (**3**).

Figure 5.7 [^1]HNMR of 1,2-Bis-(phenylsulfonamido)-4,5-bis-aminobenzene (**3**).
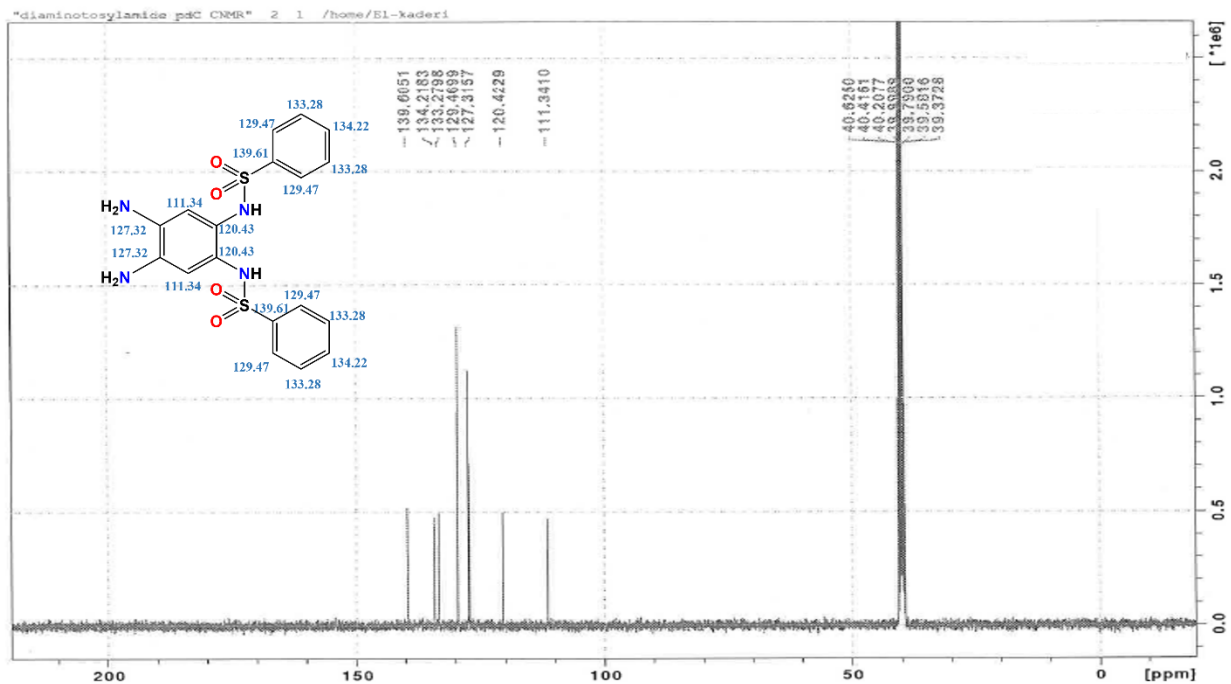
Figure 5.8 ^{13}CNMR of 1,2-Bis-(phenylsulfonamido)-4,5-bis-aminobenzene **(3)**.
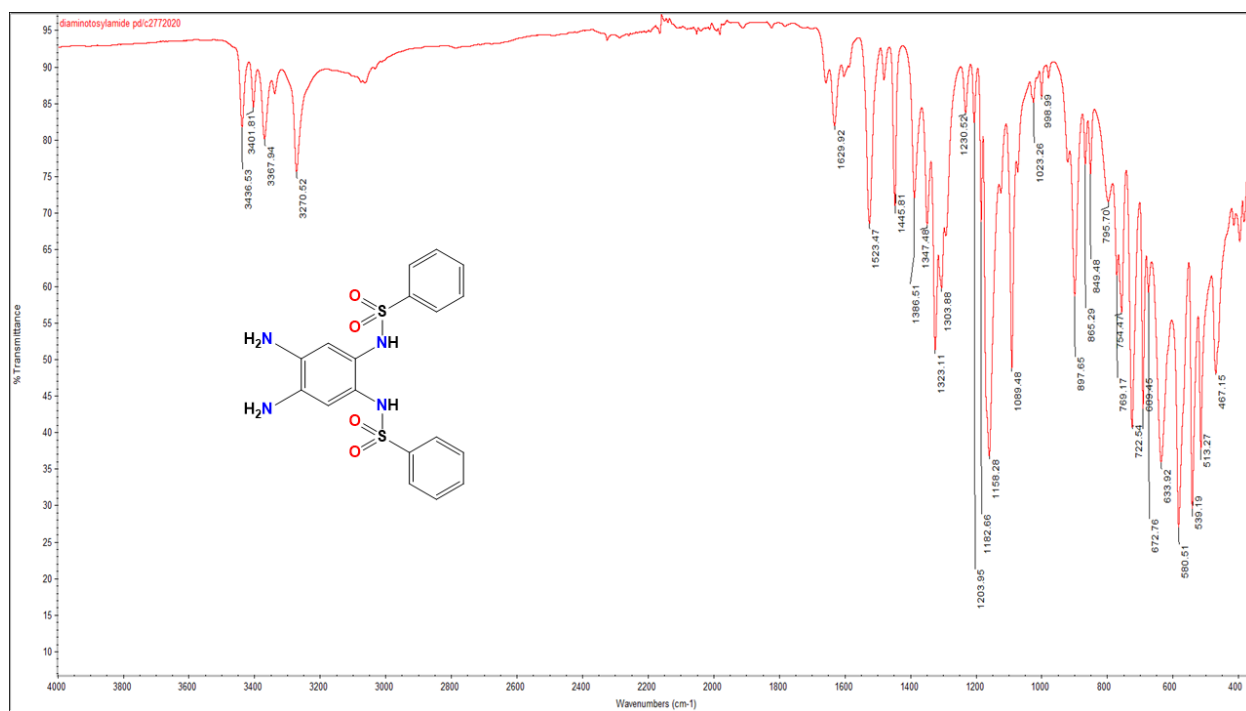
Figure 5.9 ATR-IR of 1,2-Bis-(phenylsulfonamido)-4,5-bis-aminobenzene **(3)**.

5.2.2.4. Hexaazatrinaphthalenehexasulfonamide (HATNHSA)[193] (4)

1.0 g of 4,5-Diamino-1,2-phenylene-dibenzenesulfonamide (2.39 mmol) and 248.8 mg of hexaketocyclehexane octahydrate (0.80 mmol) was mixed with 25 ml deoxygenated acetic acid in a 100 ml three-necked round bottom flask. The mixture was heated for 48 hours at 120 °C. After cooling down to room temperature, the solution was poured into a 500 ml water-ice slurry. Then, filter out the green precipitate using a frit funnel. The crude product was air-dried to afford a green precipitate with a high yield. The crude product was stirred in hot ethanol for 10 minutes for further purification, and the solution was filtered while it is warm. The product was dried in the oven overnight at 90 °C. (>90 % yield) ATR-IR; 3297 (NH), 3071 cm^{-1} (=C-H), 1622, 1479 cm^{-1} (C=C), 1220 cm^{-1} (C=N), 1156 and 1328 cm^{-1} (S=O). ^{1}H NMR (400 MHz, DMSO-d6) δ 7.62 (t, 12H), 7.70 (t, 6H), 7.94 (d, 12H), 7.99 (s, 6H); ^{13}C NMR δ 118.5, 127.4, 130.2, 134.2, 135.0, 139.4, 140.1, 143.5 ppm.
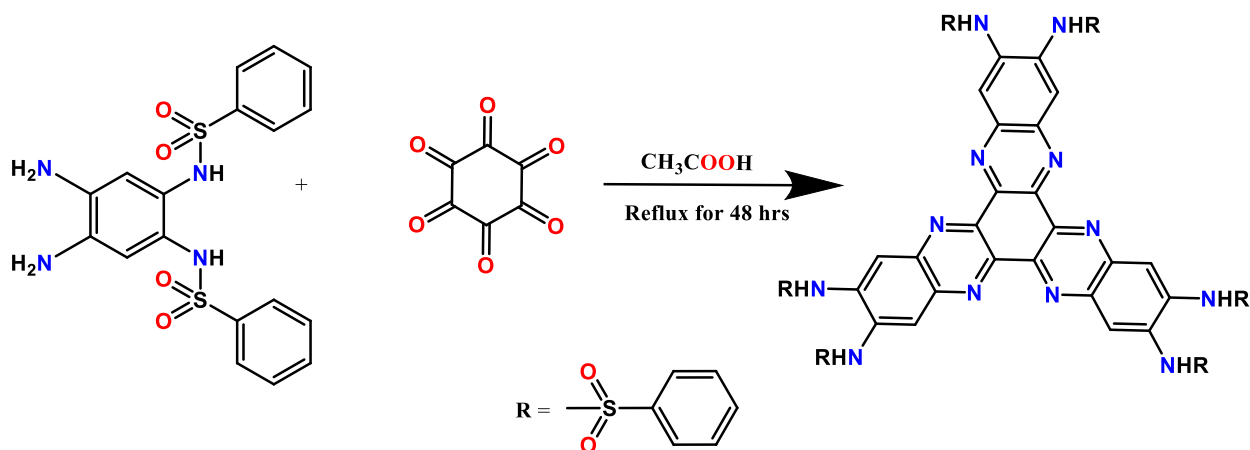
Scheme 5.5 The synthesis of HATNHSA (4).

Figure 5.10 ^{1}HNMR of HATNHSA (**4**).

Figure 5.11 ^{13}CNMR of HATNHSA (**4**).
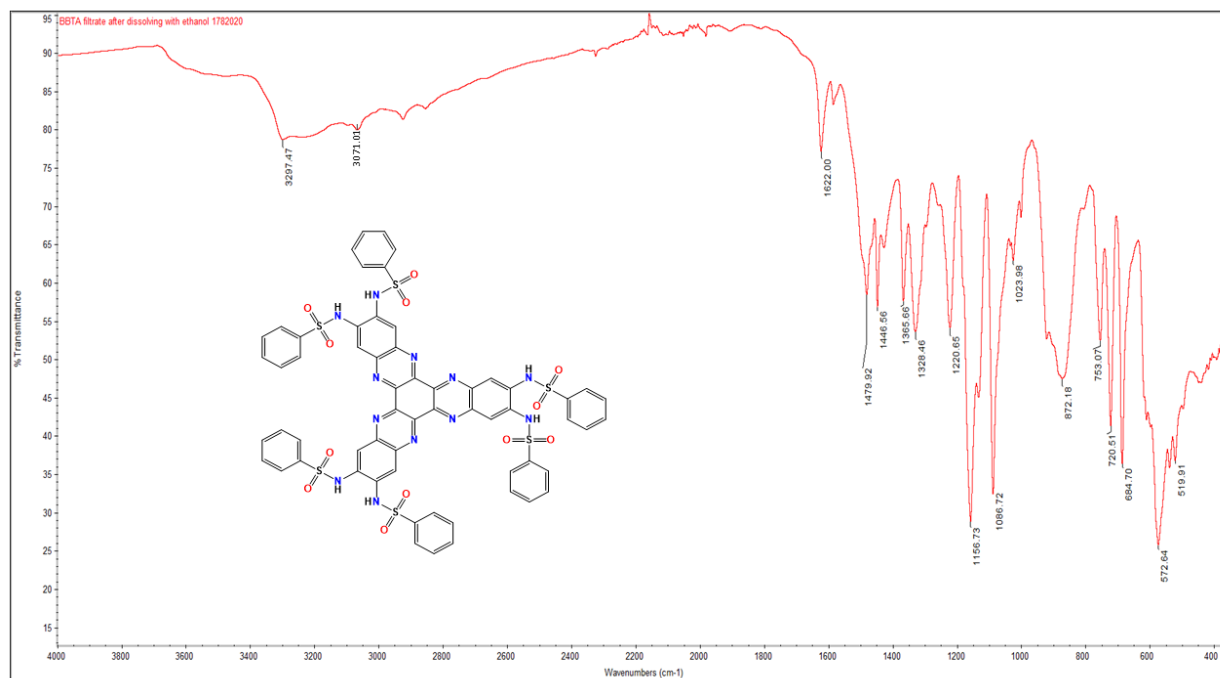
Figure 5.12 ATR-IR of HATNHSA (**4**).

5.2.2.5. Hexaazatrinaphthalenehexamine (HATNHA)[194]

1.0 g of HATNHSA (0.76 mmol) was mixed with 25 ml conc. H_2SO_4 in 100 ml round bottom flask and stirred for 24 h at room temperature. After 24 hours, the solution was poured into 1000 g of ice to avoid the exothermic heat between H_2SO_4 and water. When the ice has melted, the precipitate was filtered out using a fine frit funnel and washed with distilled water (30 ml x 3). Meanwhile, 300 ml of 10 % Potassium carbonate solution was prepared to neutralize the product. To do so, the precipitate was collected and dispersed in the K_2CO_3 solution and stirred for 3 hours. After completion, the product was filtered out using a fine frit and washed many times with double deionized water (DDW) (30 ml x 5). The sample was dissolved in 100 ml DMSO for further purification, and then water was added until the product reappeared again. Then the solution was kept under stirring for 30 minutes at room temperature. Finally, the product was collected and dried under a vacuum to afford shiny dark green building block HATNHA. (93% yield) ATR-IR;

96

3184 and 3275 (NH$_2$ symmetrical and asymmetrical stretching), 3071 cm^{-1} (=C-H), 1634, 1492 cm^{-1} (C=C), 1262 cm^{-1} (C=N). ^{1}H NMR (400 MHz, DMSO-d6) δ 6.14 (s, 12H), 7.23 (s, 6H); 13C NMR δ 105.09, 139.25, 140.27, 143.40 ppm.
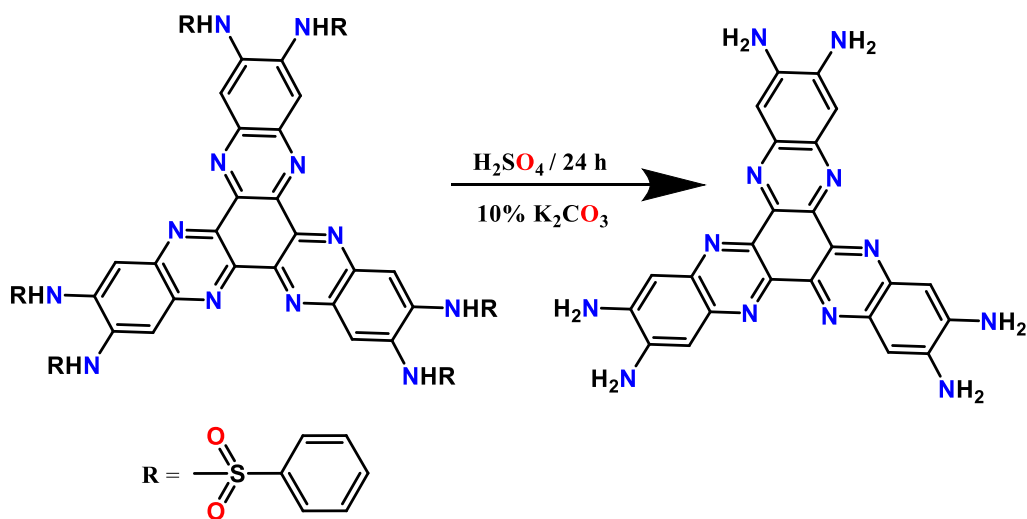
Scheme 5.6 The synthesis of HATNHA.
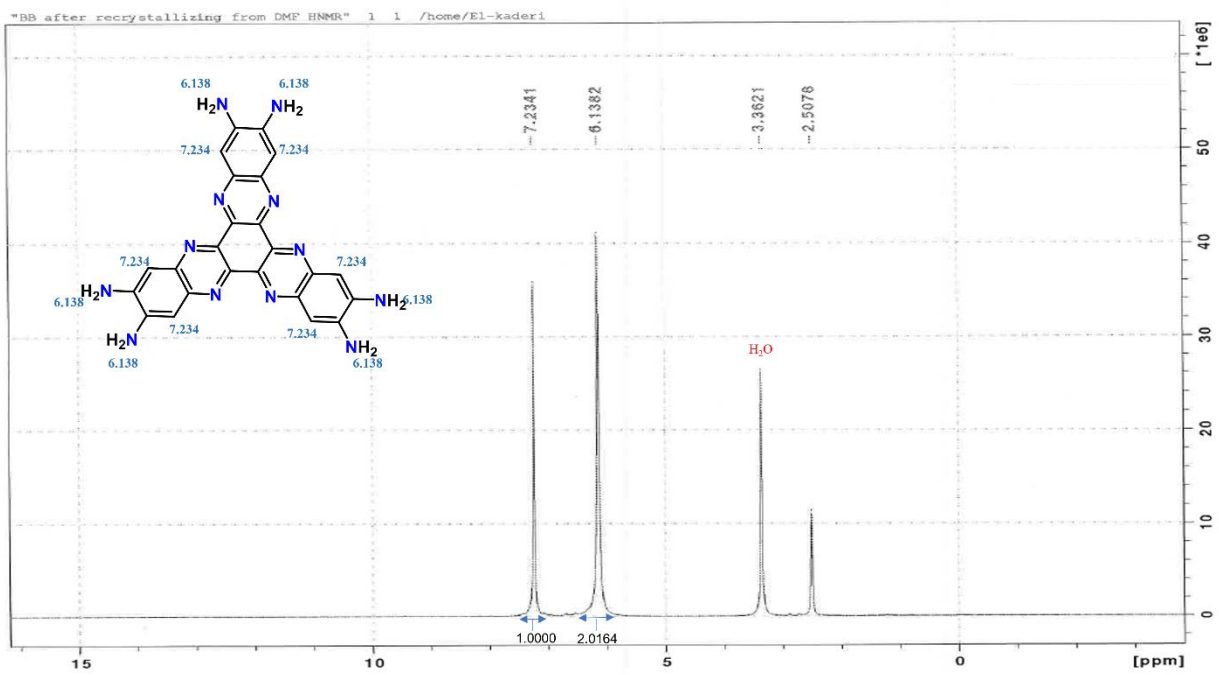
Figure 5.13 ^{1}HNMR of HATNHA.

Figure 5.14 ^{13}CNMR of HATNHA.

.

Figure 5.15 ATR-IR of HATNHA.

5.2.2.6. Synthesis of Aza-BILP monomer

HATNHA (100 mg, 0.210 mmol) and benzaldehyde (67.0 mg, 64.4 µl, 0.632 mmol) was mixed with 25 ml deoxygenated acetic acid in a 100 ml three-necked round bottom flask. The mixture was heated for 48 hours at 120 °C. After cooling down to room temperature, the solution was poured into a 500 ml water-ice slurry. Then, filter out the black precipitate using a frit funnel. To crystallize the monomer, the crude product was dissolved in 5 ml DMSO and left overnight. The crystallized product was crushed out to afford orange crystalline monomer; 3138 cm^{-1} (N-H stretching), 3071 cm^{-1} (=C-H), 1632, 1410 cm^{-1} (C=C), 1247 cm^{-1} (C=N). ^{1}H NMR (400 MHz, DMSO-d6) δ 7.23 (m, 15H), 7.82 (s, 6H), 12.6 (s, 3N-H)
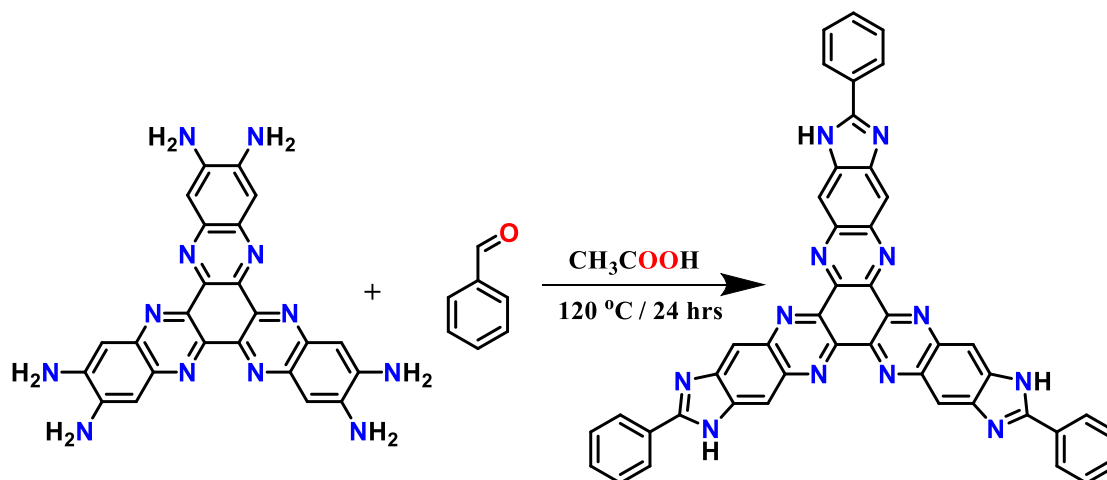
Scheme 5.7 The synthesis of Aza-BILP monomer.
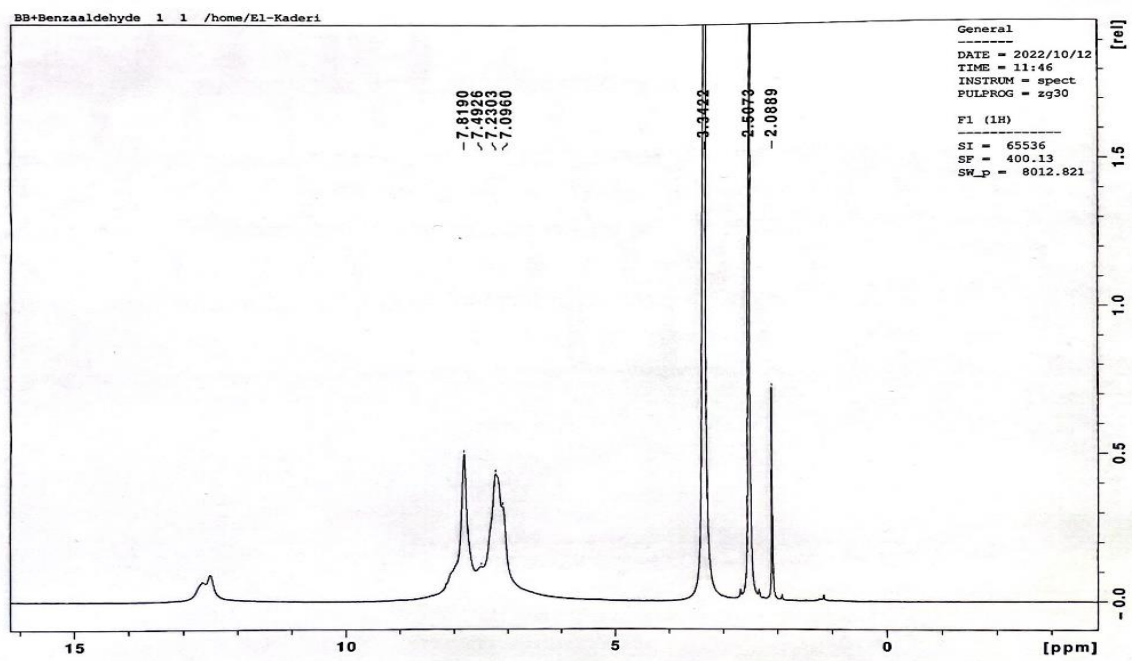
Figure 5.16 ^{1}HNMR of Aza-BILP monomer.
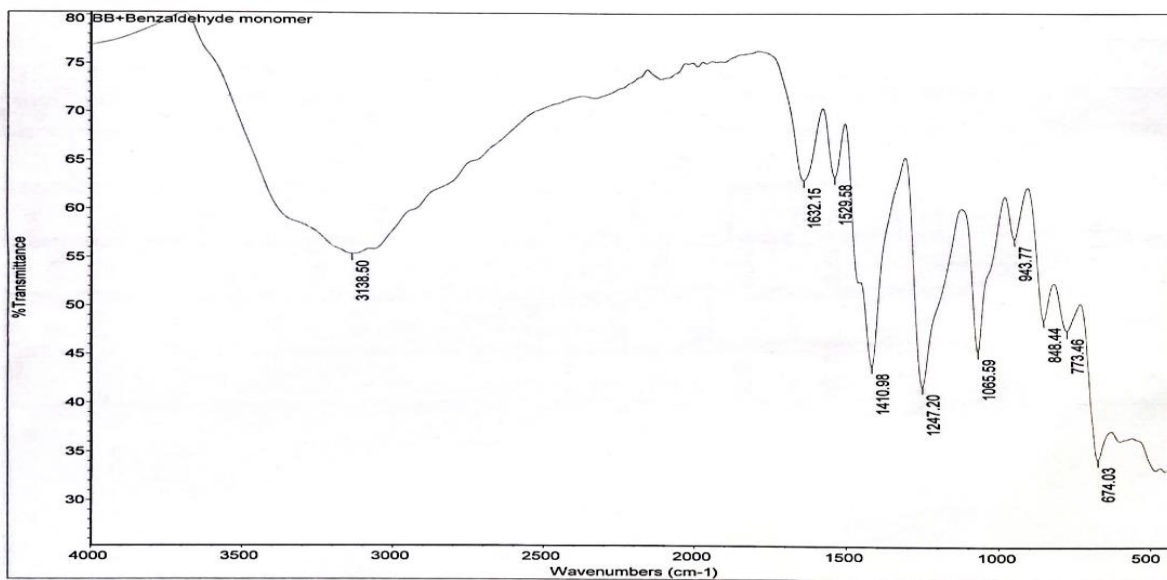
Figure 5.17 ATR-IR of Aza-BILP monomer.

100

5.2.2.7. Synthesis of BILP-based terephthalaldehyde

A dried Pyrex tube was charged with HATNHA (25.0 mg, 0.0526 mmol) and terephthaldehyde (10.5 mg, 0.0783 mmol, 1.5 eq.), 1,4-dioxane (2.0 mL) and mesitylene (0.5 ml), were charged in sequence. The mixture was sonicated for 3 minutes, and the tube was flash-frozen at 77 K using a liquid N_2 bath. After the first freezing, 0.5 ml of 3M CH_3COOH was added then followed by three freeze-pump-thaw cycles. Eventually, the tube was flame sealed under a vacuum and placed in the oven at 120 °C for 5 days, a dark brown precipitate formed at the bottom of the tube, which was isolated by filtration and washed with DMF (10 ml × 2). The solid was soaked in DMF (20 mL) at room temperature for 2 days, during which the solvent was replaced 2 times per day. After two days, DMF was replaced with CH_2Cl_2 and kept exchanged with the same solvent 2 times per day for 2 days. the product was dried in a vacuum oven at 60 °C overnight to afford a reddish-brown fluffy precipitate.
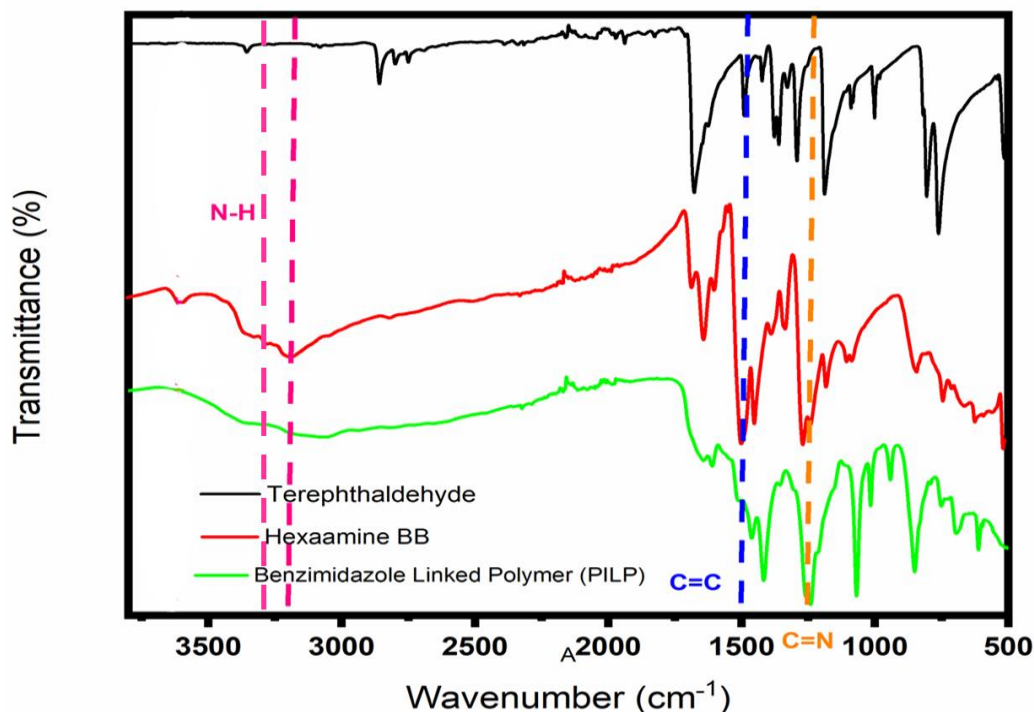
Figure 5.18 ATR-IR comparison of the precursors and the Aza-BILP.
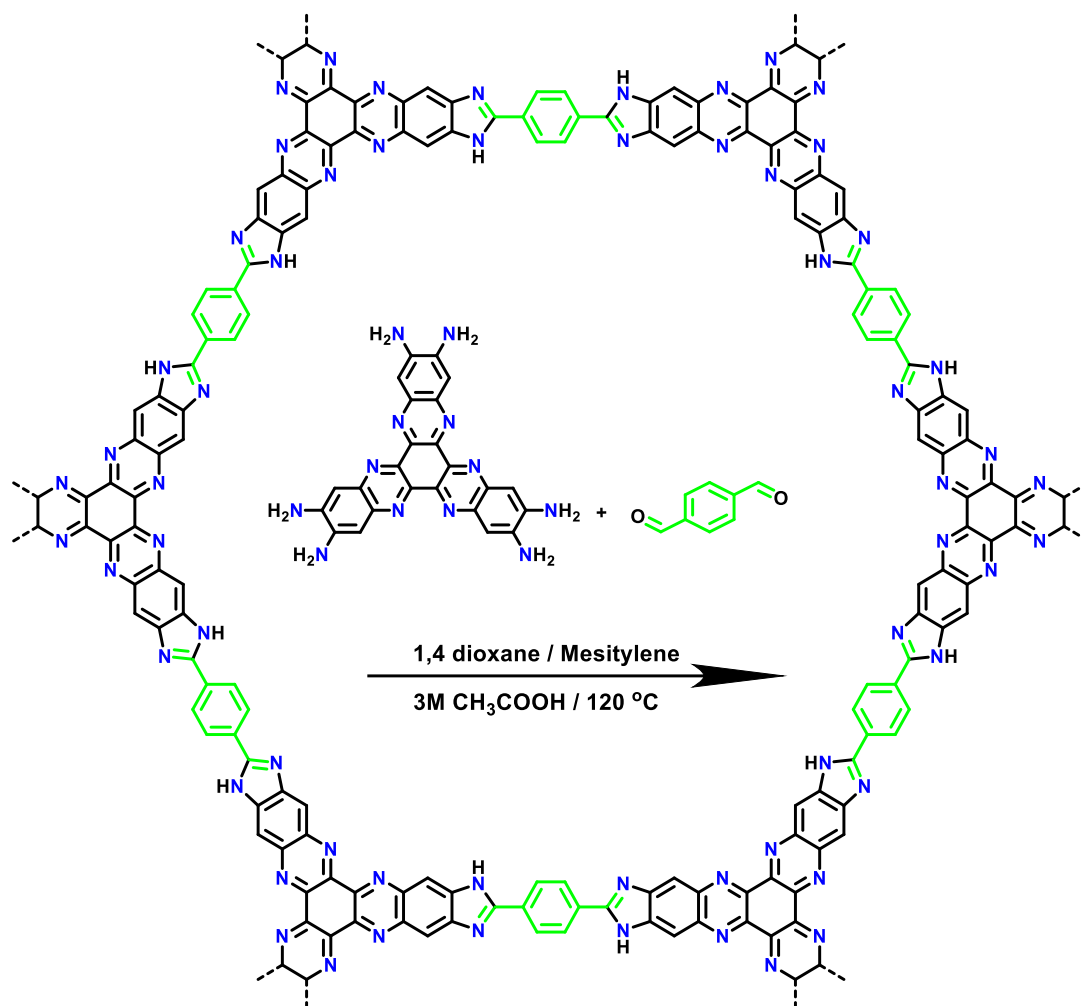
Scheme 5.8 The synthesis of BILP based terephthalaldehyde.

5.2.3. Electrode preparation and Coin Cell assembly

Aza-BILP was utilized as a working electrode and tested as a cathode in a sodium metal half-cell. The cathode composite consisted of 50 wt % active material (Aza-BILP), 30 wt % Ketjenblack-600JD, and 20 wt % binder (sodium alginate). A slurry was made of all aforementioned components along with DDW and kept under stirring overnight at room temperature. Then the slurry was cast on an aluminum foil (current collector) using a doctor blade and dried in the vacuum oven at 70 °C. The cathode was cut into a circular disc with a diameter of 15 mm and

assembled in a CR2032-type coin cell. Sodium metal was cut into a disc too and used as an anode, counter, and reference electrode. 1.0 M $NaPF_6$ in DEGDME solution was served as an electrolyte to facilitate the sodium ions movement between the electrodes (15 µL/ 0.5 mg of the active material). The polypropylene separator was used as a membrane and to separate between electrodes. The entire battery assembly process was done inside an argon-filled glove box using an electric crimper (MTI Corp.).

5.2.4. Physical and Spectral Characterization

The nuclear magnetic resonance data (^{1}HNMR and ^{13}CNMR) was obtained by NMR-400 MHz (Bruker), attenuated total reflection infrared spectroscopy (ATR-IR) was used to collect the infrared spectra. The surface topography images were captured at high magnifications by scanning electron microscopy (SEM, Hitachi SU-70 FE-SEM). 3Flex surface analyzer (Micrometrics) was utilized at 77 K to collect the nitrogen adsorption/desorption isotherms and the Brunauer-Emmett-Teller (BET) surface area measurements. Aza-BILP was activated by degassing at 80 °C for 4 hours and then was increased to 110 °C for 7 h at a rate of 5 min ^{o}C^{-1} under 10^{-6} bar vacuum. X-ray photoelectron microscopy (XPS) measurements were carried out using PHI VersaProbe III scanning XPS microprobe. For Raman spectroscopy studies, Thermo Scientific DXR Smart Raman was used at 532 nm laser with a power of 5 mW to excite the samples.

5.2.5. Electrochemical measurements

All electrochemical studies of the assembled coin cells were carried out and examined at room temperature using electrochemical workstation (CHI 600C). This includes the cyclic voltammetry (CV), galvanostatic charge/discharge, rate capability, long-term cycling stability, and electrochemical impedance spectroscopy (EIS).

5.3. Results and Discussion

In the conductive COFs, hexaazatrinaphthalene (HATN) molecular unit plays an important role for battery and supercapacitor applications due to its extended π-conjugated nature and the richness of the aza bonds in the framework, which both are essential for the charge transport and redox process (charge/discharge), respectively. COFs-based HATN can be synthesized by one step polycondensation reaction. A variety of COFs-based HATN can be made by changing the building blocks causing changes in theoretical specific capacity and the electrical conductivity of the framework. Aza-BILP was synthesized by a polycondensation reaction of a unique Hexamine building block and terephthalaldehyde. Hexamine building block was synthesized and designed to have 6 build-in aza active sites as depicted in scheme 2. Besides the 6 build-in aza redox sites, 3 additional sites can be added upon condensation with terephthalaldehyde. Therefore, Aza-BILP could be a potential cathode material since it has 9 active redox pyrazine sites per repeating unit and leads to a high theoretical specific capacity of 392 mA h g^{-1}. The network connectivity between the building blocks was confirmed by ATR-IR (Figure 5.18).

The crystallinity and the periodical structure of Aza-BILP-based terephthalaldehyde were confirmed by powder X-ray diffraction (PXRD) and high-resolution transition emission microscopy (HTEM). Both possible AA (eclipsed) and AB (staggard) were simulated to determine the stacking of 2D sheets growth. Simulations of AA stacking was done using P6/mmm space group with lattice parameters of a = b= 37.716 Å, c = 3.442 Å and α = β = 90 °, γ = 120 °(Table 5.1). On the other hand, the model of AB stacking was simulated using P6$_3$/mmc space group with a lattice parameter of a = b= 37.882 Å, c = 6.360 Å and α = β = 90°, γ = 120° (Table 5.2). As can be found, the experimental PXRD patterns for Aza-BILP concur well with the simulated patterns of the eclipsed stacking (AA) model with a P6/mmm space group. Aza-BILP exhibits a 2D stacked

sheets in eclipsed conformation. However, in the AB staggered stacking mode, the PXRD pattern exhibited some extra patterns which we could not see in the experimental XRD patterns. Furthermore, the stacking hexagonal layers toward the z-axis (001) was a little shifted toward higher $2\theta^o$ in the staggered mode. The experimental PXRD patterns was in agreement with the calculated patterns obtained by materials studio at $2\theta^o = 2.71$, 4.69, 5.41, 7.16 and 26.10° with calculated interplanar spacing distance (d-spacing) of 32.59, 18.82, 16.33, 12.34 and 3.41 Å, corresponding to (100), (110), (200), (210) and (001) crystal planes, respectively. To refine the position of the atoms in the model, Pawley refinement was carried out and the profile fitting factors R_p and R_{wp} were obtained to be 2.53 and 3.31% showing very small difference between the fitted and the experimental patterns (Figure 5.19).
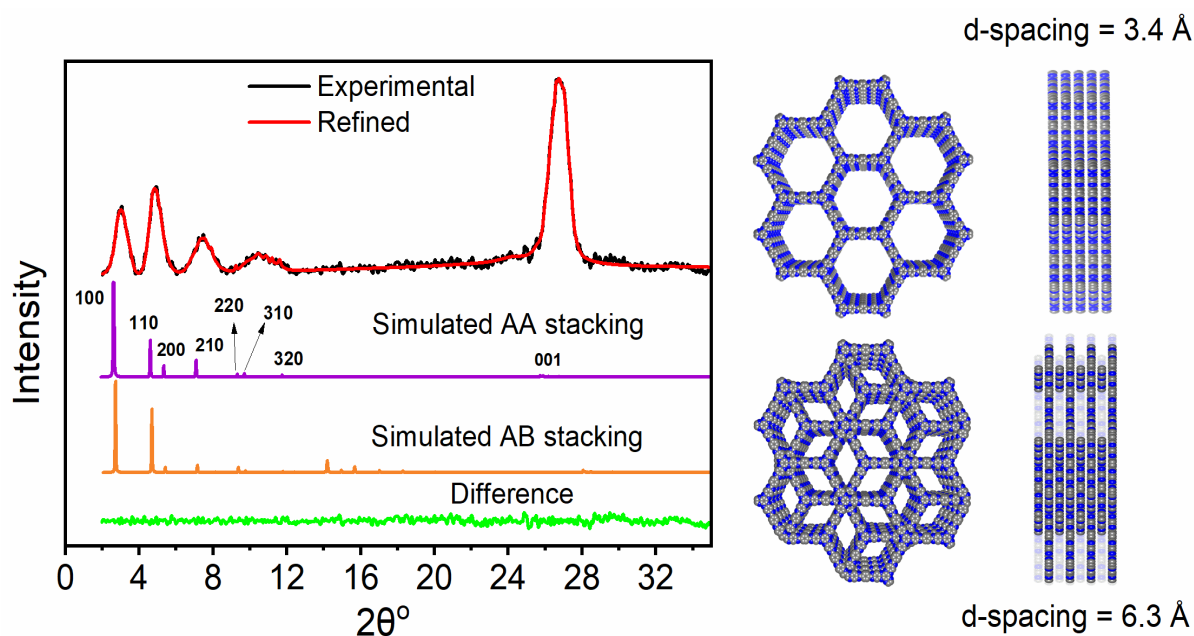
Figure 5.19 PXRD patterns of BILP; where the experimental in black, the Pawley refinement in red showing very minimal difference (green line) with R_p and R_{wp} of 2.53 and 3.31%, respectively, the simulated PXRD patterns for the AA eclipsed and AB structures are in purple and orange respectively.

Table 5.1 Crystallographic parameters for AA stacking Aza-BILP.

Crystallographic parameters for BILP-Based terephthalaldehyde AA stacking (Eclipsed)	
Crystal type	Hexagonal
Space group	P6/mm
Source wavelength (Å)	1.5406
a (Å)	37.715697
b (Å)	37.715697
c (Å)	3.44239
α (°)	90
β (°)	90
γ (°)	120
R_p (%)	2.53
R_{wp} (%)	3.31
Refinement method	Pawley

Table 5.2 Crystallographic parameters of AB stacking Aza-BILP.

Crystallographic parameters for BILP-Based terephthalaldehyde AB stacking (Staggered)	
Crystal type	Hexagonal
Space group	P6$_3$/mmc (194)
Source wavelength (Å)	1.5406
a (Å)	37.882282
b (Å)	37.882282
c (Å)	6.360726
α (°)	90
β (°)	90
γ (°)	120

For further investigation of the periodicity of the porous framework of Aza-BILP, High-resolution transmission electron microscopy (HRTEM) was carried out (Figure 5.20). HRTEM images showed high-ordered lattice fringes toward the z-axis with an interlayer distance of 3.3 Å between (0 0 1) crystal planes (Figure 5.20 a, c). Furthermore, a high-ordered honeycomb-like structure was seen with a uniform channel diameter of 3.3 nm on the (0 0 1) plane that in agreement with the simulated AA stack model of the Aza-BILP (Figure 5.20 b).
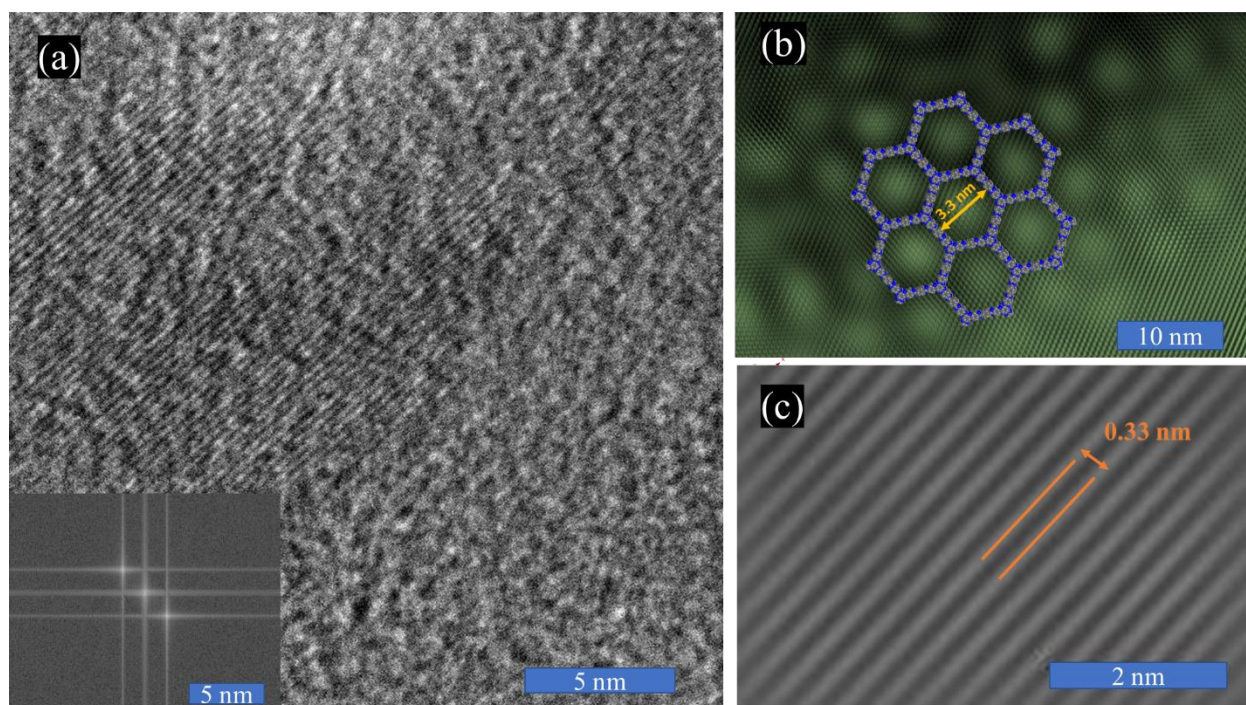
Figure 5.20 HRTEM images exhibit a) well-ordered lattice fringes b) a well-ordered 2D hexagonal layers with a diameter of 3.3 nm. c) Zoom-in FFT image for the lattice fringes with d-spacing of 0.33 nm. (The inset represents the FFT image for the diffracted patterns.)

To investigate the porosity of our Aza-BILP, nitrogen adsorption/desorption isotherm was carried out to measure the porosity and the surface area of Aza-BILP. The BET surface area was found to be (SA_{BET} = 930 m^2 g^{-1}). Furthermore, the pore size distribution did not show only micropores (< 20 Å) but also mesoporous (20-100 Å, , Figure 5.21 b), which causes the apparent hysteresis

between adsorption and desorption at higher relative pressure in the isotherm[195,196] (Figure 5.21 a). The high porosity of BILP was clearly shown in the SEM images of the pristine sample. The morphology of the pristine BILP exhibits nanorods-like morphology (Figure 5.22).
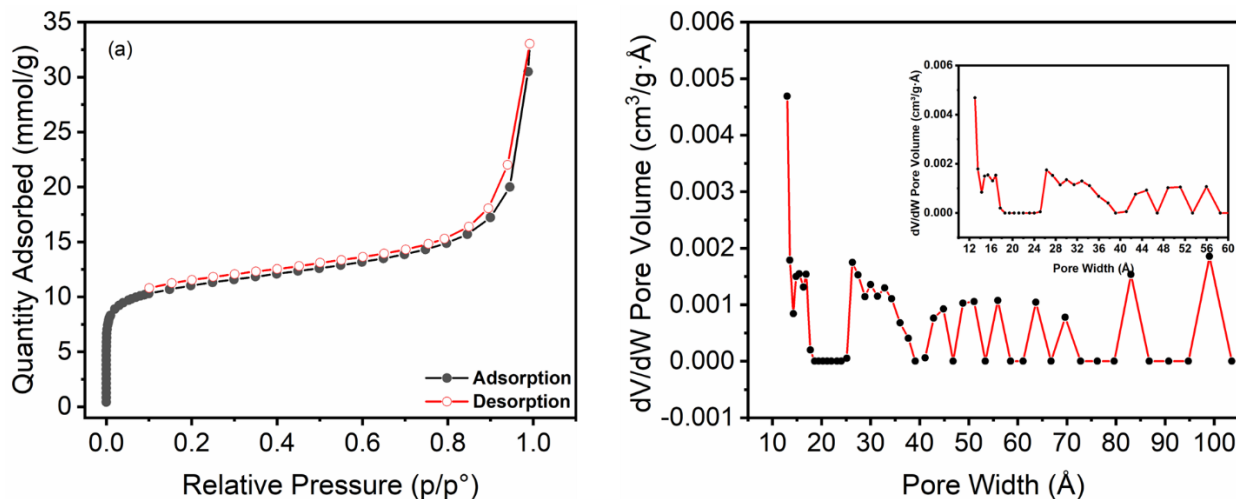
Figure 5.21 (a) is the N_2 adsorption/ desorption isotherm and (b) is the pore size distribution of BILP showing both microporous up to 20 Å as well as mesopores structures from 20 up to 100 Å.
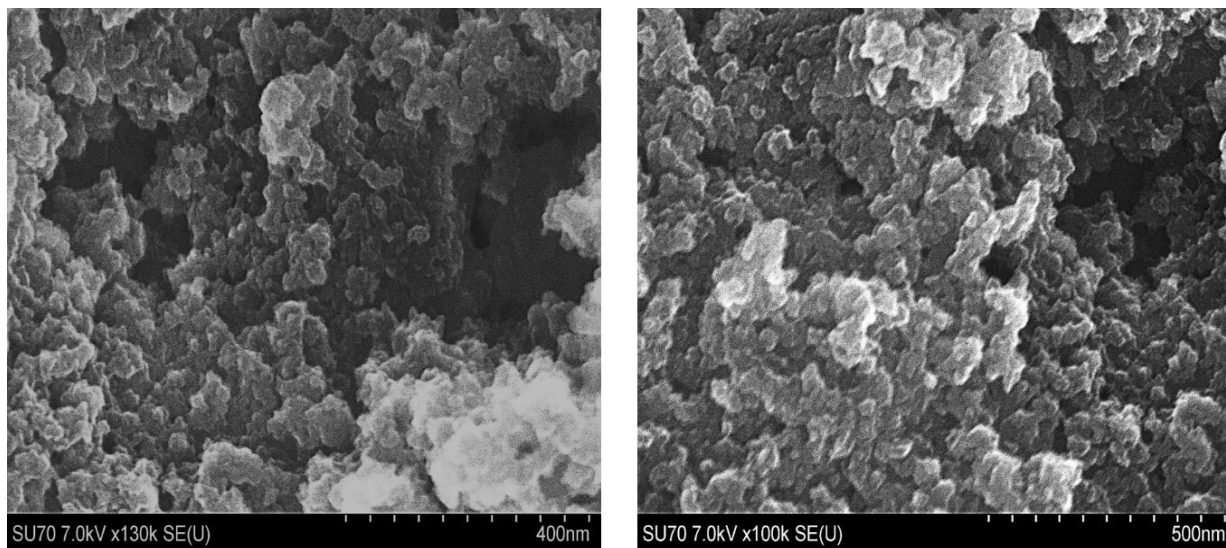
Figure 5.22 SEM images of as-prepared BILP

The first electrochemical test has been done after the battery assembly was cyclic voltammetry (CV). CV gives an idea about the reversibility process and the electron transfer kinetics of the redox reactions. Also, it indicates the type of electrochemical energy storage and finally, gives insight into the potential window for future characterization of the electrode.
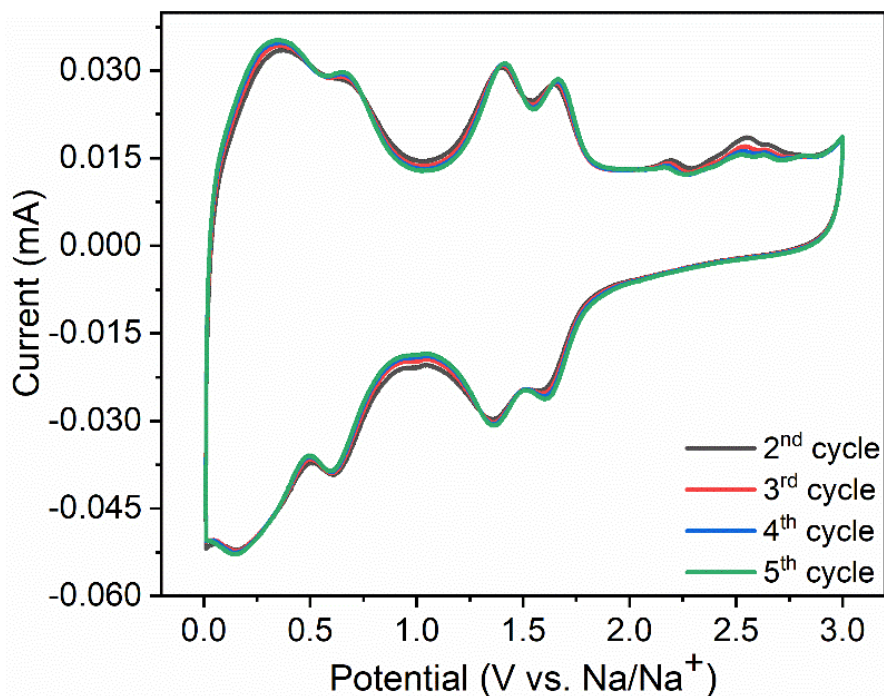
Figure 5.23 Cyclic voltammograms of BILP electrodes in 1M $NaPF_6$/DEGDME at a scan rate of 0.1 mV s^{-1} of the potential range between 0.01 and 3.0 V.

CV peaks attest for the reversible redox reactions occurred on the aza active sites (C=N) in the phenazine ring and the benzimidazole repeating units. These redox reactions represent the sodiation (reduction) and de-sodiation (oxidation) processes. Figure 5.23 shows three highly reversible redox peaks at around 0.67-0.50/0.58-0.72, 1.51-1.24/1.30-1.54 and 1.64-1.51/1.54-1.71 V. The first reversible redox peak is attributed to the redox reaction on the aza bond in the benzimidazole ring. To ensure that, the CV of aza-BILP monomer was carried out at scan rate of 0.1 mV s^{-1} and showed the same reversible peak of the framework at 0.67-0.50/0.58-0.72 (Figure

5.24). In comparison, the other two curves have been seen in the HATN core-based COF, where the sodiation/desodiation process can happen on the six aza bonds in the phenazine rings.[19]
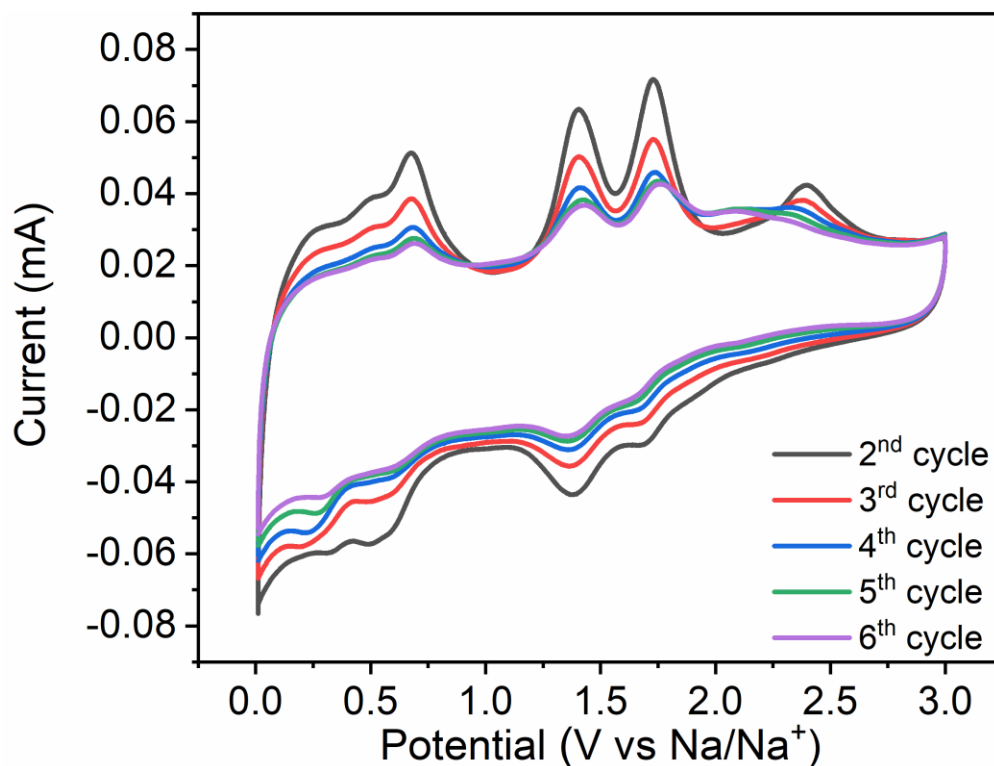
Figure 5.24 Cyclic voltammograms of Aza-BILP monomer electrodes in 1M NaPF$_6$/ DEGDME at a scan rate of 0.1 mV s^{-1} of the potential range between 0.01 and 3.0 V.

Furthermore, irreversible anodic peaks were observed at 2.6 V after the first 4 cycles. However, the irreversible anodic peak gets disappeared upon cycling. This might be attributed to a partial interaction between the electrolyte and imidazole ring causing the formation of inorganic and organic salts that can't revert back after lowering the potential (Figure 5.25).
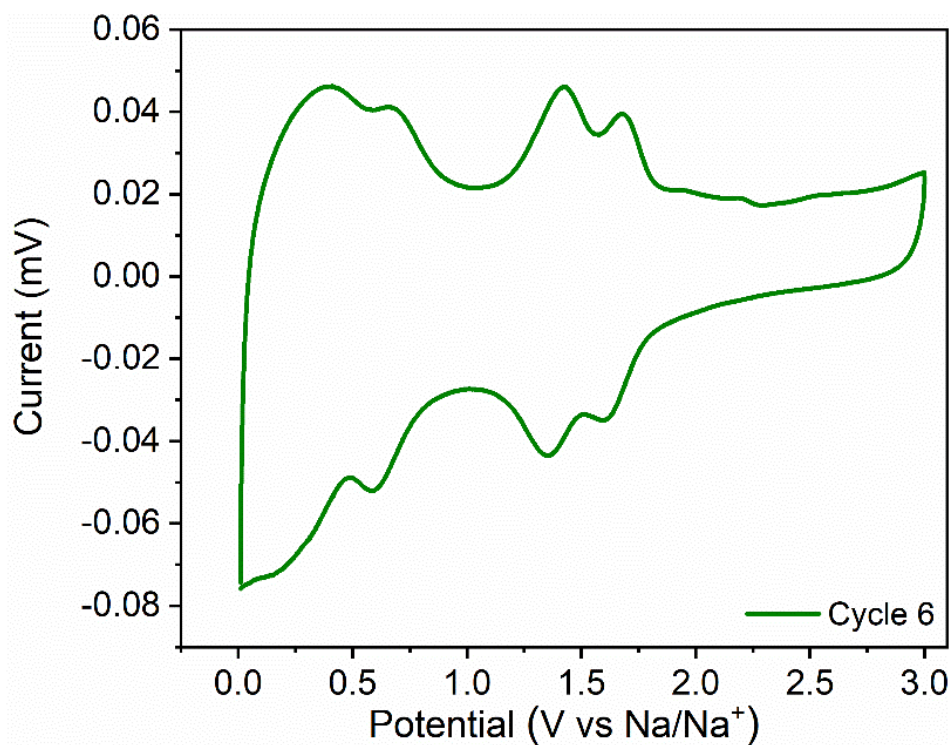
Figure 5.25 Cyclic voltammogram of BILP electrodes for just cycle 6 showing the disappearance of the anodic peak at 2.6 upon cycling in 1M NaPF$_6$/ DEGDME at a scan rate of 0.1 mV s^{-1} of the potential range between 0.01 and 3.0 V.

The BILP was designed to have additional redox-active sites than the conventional COF-based HATN. There are nine electroactive aza bonds per repeating unit comprising of six phenazine N atoms (three pairs in the HATN core) and three electroactive benzimidazole N atoms. The reactivity of the HATN molecule toward sodium using DFT stimulation has been addressed by El-Kaderi et al. The results show that the three N pairs of HATN molecule can strongly coordinate with up to six Na atoms at which two Na can bond with each N pair. Furthermore, the DFT study showed that the first reduction with three Na caused the metal ion to be coplanar with HATN. However, further reduction with three additional Na leads the coplanar Na to be pushed and sit on an opposite side of the plane containing the HATN moiety.[39] Besides the six-redox reaction

provided by HATN, benzimidazole rings can endow three additional sites to come to nine-electron redox reactions per repeating unit (Figure 5.26 a).
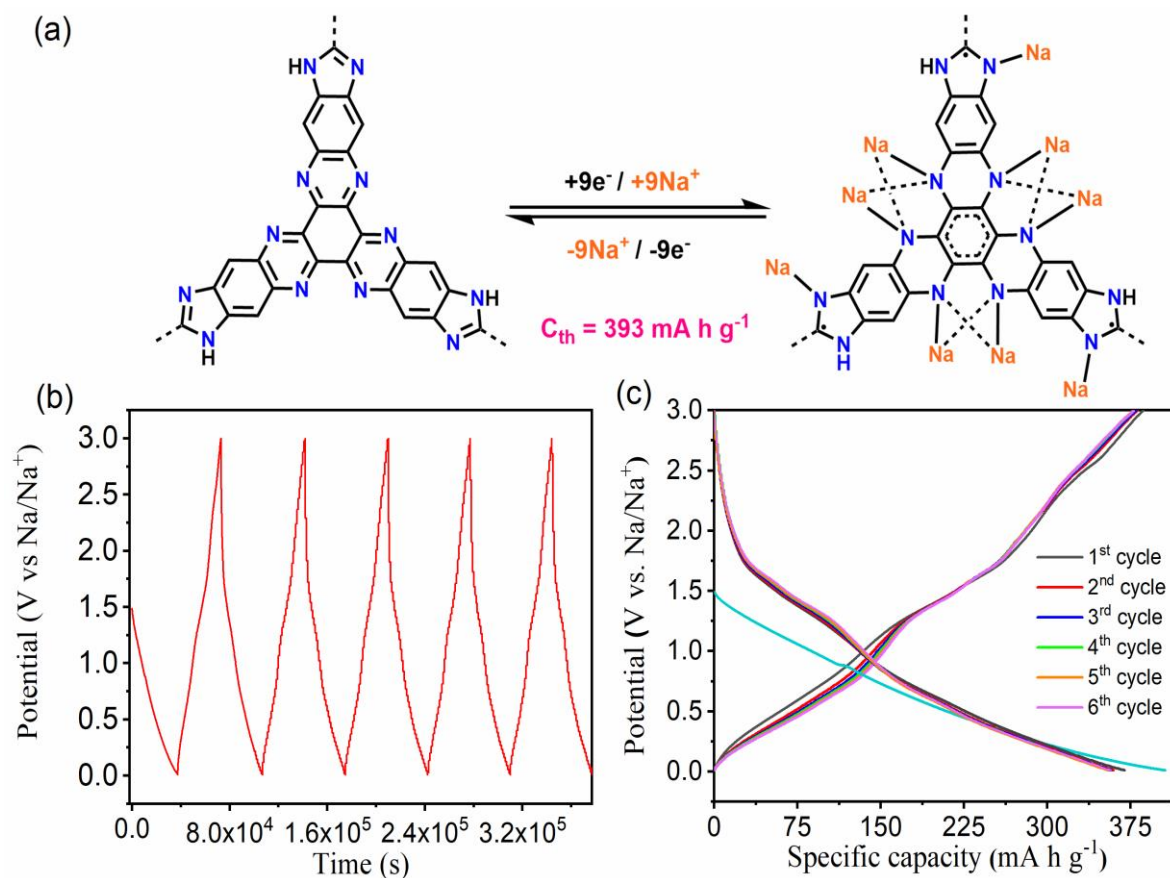
Figure 5.26 (a) Redox mechanism of the aza active sites, (b) time vs. potential profile and (c) six cycles galvanostatic charge/discharge at the current rate of 0.1 C.

To check the performance of BILP as an electrode material in SIBs, galvanostatic charge/discharge studies for the first 6 cycles was carried out at a current rate of 0.1 C (Figure 5.26 c). The selected potential range of 0.01 to 3.0 V vs. Na/Na$^+$ was used to run the battery because at high current rate, the battery behavior exhibits a significant disturbance above 3.0 V as well as the absence of the reversible peaks between 3.0 and 3.5 V (Figure 5.27). Furthermore, Thermodynamically, aqueous electrolytes show an electrochemical stability window of 1.23 V. Kinetic effects may expand the

stability limit to ~2 V.[197] As a result, the electrode showed in the first cycle an outstanding charge specific capacity of 387 mA h g^{-1} and a discharge capacity of 370 mA h g^{-1}. The resultant charge/discharge capacities speak for 98.5 % and 94.1 %, respectively of the theoretical capacity (393 mA h g^{-1} based on nine-electron redox reaction and the repeating unit molecular weight of 615 g/mol). The first cycle showed the highest charge/discharge specific capacity of 387/370 mA h g^{-1} compared to the other charge cycles. On the other hand, starting second cycle onwards, the capacities for all other cycles (2-6 cycles) exhibit highly reversible charge/discharge capacities of 377/360 mA h g^{-1} (Figure 5.26 c). The observed hysteresis in the first charge/discharge cycle (387/370 mA h g^{-1}), might be attributed to the electrolyte reduction on the anode surface and caused the formation of the solid electrolyte interface (SEI) layers. The SEI layer is typically a passive layer consisting of organic and inorganic electrolyte decomposition products such as sodium salts. These layers can partially hold and immobilize the cyclable sodium ions causing capacity degradation and charge/discharge capacity difference (hysteresis).[119] it is worth noting that the galvanostatic charge/discharge slopes exhibit three reversible curves which attest the curves of the CV.
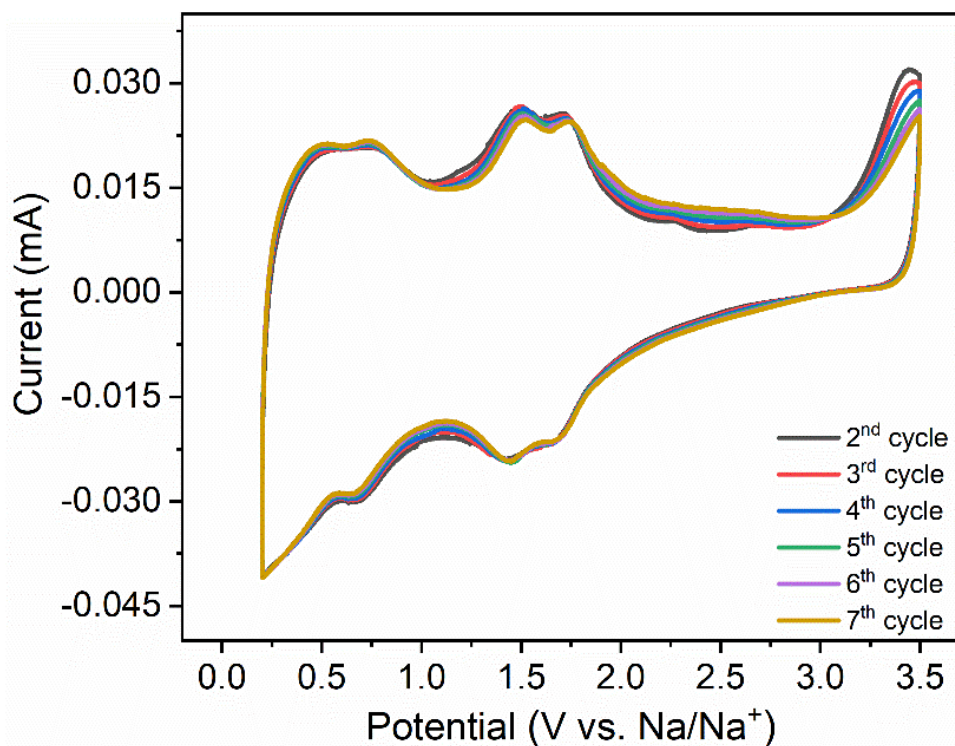
Figure 5.27 Cyclic voltammograms of BILP electrodes in 1M $NaPF_6$/ DEGDME at a scan rate of 0.1 mV s^{-1} of the potential range between 0.2 and 3.5 V.

For the sake of comparison, galvanostatic charged discharged cycles at 0.1 C and rate capability for the Aza-BILP monomer were carried out (Figure 5.28 a). Unlike Aza-BILP, the monomer required a full cycle to form a stable SEI and that was clear from the big first charged specific capacity of 527 mA h g^{-1} which is almost the double capacity of the theoretical specific capacity of the monomer which is 329 mA h g^{-1}. On the other hand, the discharge capacity after the SEI formation was 315 mA h g^{-1} which attributes 95.7% of the theoretical capacity of the monomer and indicates the full utilization of the nine aza redox active sites (Figure 5.28 a). Despite the high reversibility from 1-15 C, the rate capability figure shows a big hysteresis at 0.1 C due to the multicycle SEI layer formations. Also, the monomer exhibits a large drop in capacity at higher C rates compared to the Aza-BILP (Figure 5.28 b).
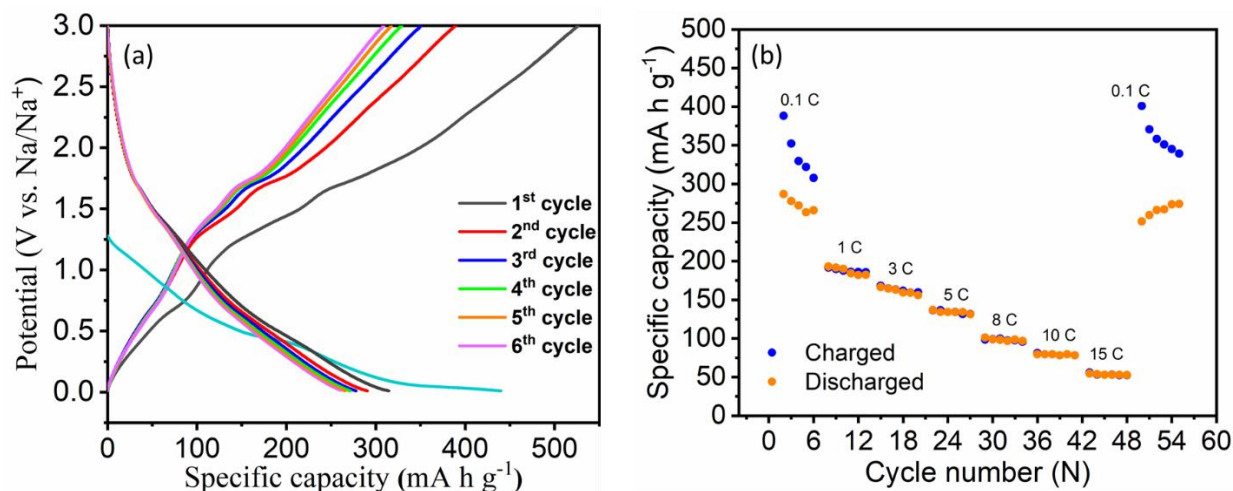
Figure 5.28 a) Galvanostatic charge/discharge at 0.1 C and b) rate capability at C rates ranging from 0.1-15 C for Aza-BILP monomer.

Diffusion kinetics and the energy storage mechanism information can be obtained by running CV measurements at different sweep rates (v) vary from 2.0 to 12 mV s^{-1} (Figure 5.29 a). In general, increasing the sweep rate magnifies the current peak (i) and broadens cyclic voltammogram as described in the equation below. However, the reversibility of the redox peaks still existed.

$$i_p = av^b$$

For the diffusion-controlled process, the peak current varies as $v^{0.5}$ (b = 0.5), which is the battery-like behaving process. However, for the surface-limiting redox, the peak current varies directly as v (b = 1), which is a capacitive-like behaving process.[103] when b is a middle area between 0.5 and 1, the pseudocapacitive behavior is dominated for a fast surface-controlled Faradic process.[105] Several cyclic voltammograms at different sweep rates were used to calculate the b-values at the current maxima in the anodic and cathodic systems. The analysis of the Aza-BILP battery exhibits that the values of b were 0.8339 for anodic and 0.8301 for cathodic systems. The small difference in the b values for anodic and cathodic systems indicates the highly reversible redox system.

Moreover, the redox peak potential separation is near to zero, which indicates the pseudocapacitive-like behavior (Figure 5.29 b).[105] As a result, and based on the aforementioned relationships between current and sweep rates for diffusion and capacitive processes, we were able to calculate quantitatively the contribution of each in the total energy storage of the BILP electrode based on the following equation:

$$i(V) = k_{Cap.}v + k_{Dif.}v^{0.5}$$

Where i(V) is the current at fixed potential, $k_{Cap.}$ and k_{Dif} are adjusted capacitive and diffusion parameters, k_{Cap} v is the capacitive contribution and k_{Dif} $v^{0.5}$ is the diffusion contribution. By rearranging the above equation, $k_{Cap.}$ (slope) and $k_{Dif.}$ (intercept), can be easily calculated (Figure 5.29 c). As a result, it is possible to specify the current fraction arising from the sodium ion diffusion (Faradaic current) and the current fraction arising from the capacitive process (non-Faradaic current) at certain potentials. $k_{Cap.}$ and k_{Dif} at different fixed potential values were calculated for oxidation potentials (charge) of 1.60, 1.80, 1.87 and 1.90 V; reduction potentials

(discharge) at 1.10, 1.16, 1.25 and 1.40 V (Figure 5.29 c) and then utilized to make the overall charge storage diagram.
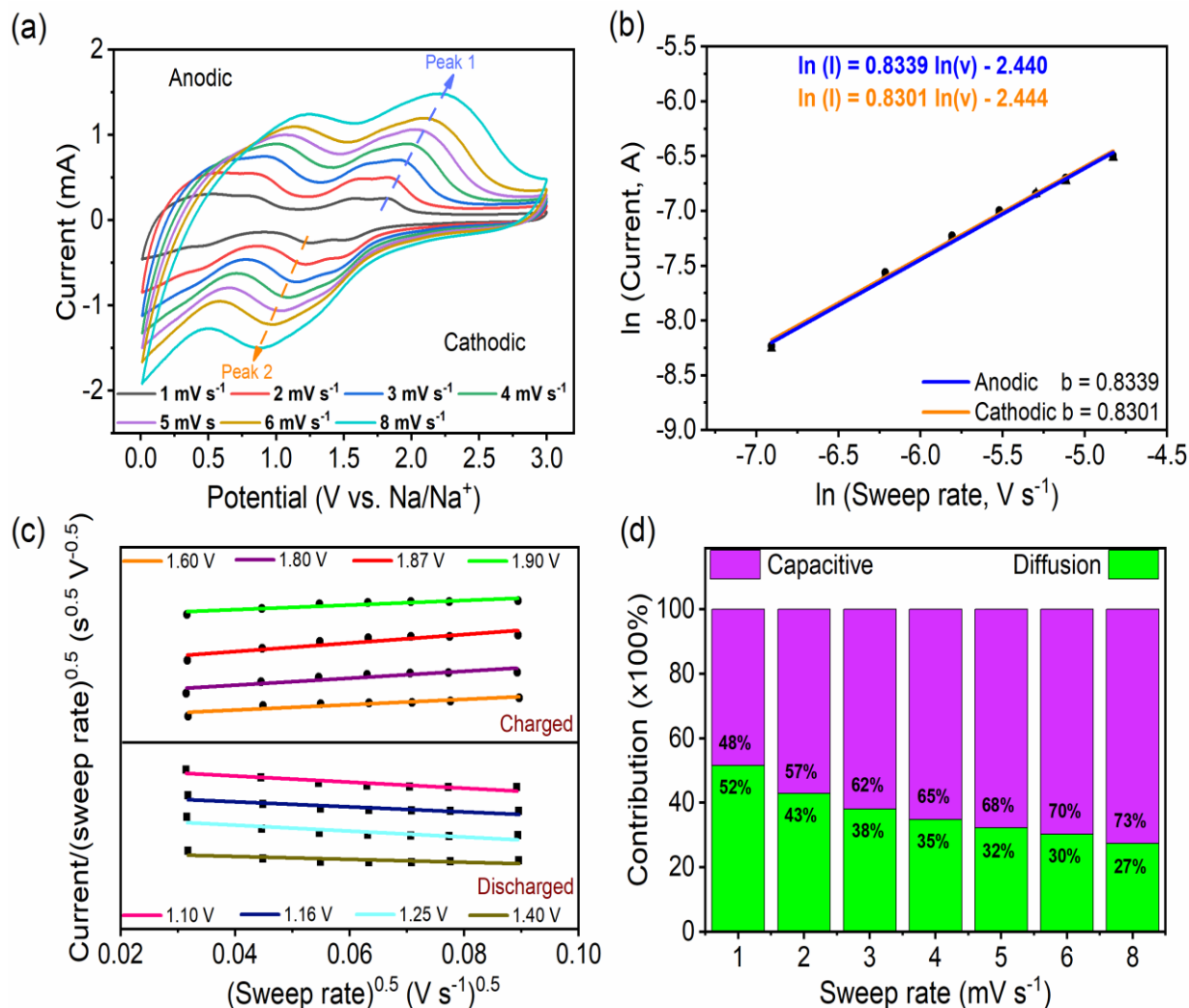
Figure 5.29 (a) CV curves at different sweep rates (1.0-8.0 mV s^{-1}) of BILP cathode in DEGDME-based electrolyte. (b) The corresponding linear fit of the ln i vs. ln v at 1, 2, 3, 4, 5, 6, and 8 mV s^{-1}. (c) Plot of i(V)/v$^{0.5}$ vs. v$^{0.5}$ of BILP based electrode at different potentials (d) the overall total charge storage contribution at different sweep rates.

The contribution diagram of the BILP electrode at sweep rates of 1, 2, 3, 4, 5, 6, and 8 mVs^{-1} shows the Faradaic (green) and non-Faradaic (violet) current contribution (Figure 5.29 d). At a lower sweep rate of 1 mVs^{-1}, the Faradaic current produced due to sodium ions diffusion (52%) was

almost comparable to the non-Faradaic current arising from the capacitive process (48%). However, increasing the sweep rates makes capacitive current more dominant. As the sweep rate increases from 1.0-8.0 mV s^{-1}, the capacitive contributions increase as 48%, 57%, 62%, 65%, 68%, 70% and 73%, respectively. This is in agreement with the cyclic voltammogram at higher sweep rate when the peaks become gradually broader, and its shape tends to be more rectangular which is a distinct feature of the capacitance behavior.[103] Therefore, higher the sweep rates, higher the capacitive contribution and thus more charge storage in the mesoporous structures of BILP.[198]

EIS studies with a frequency range of 0.01 Hz to 1 MHz were carried out for further investigation of the Aza-BILP electrode kinetics. Nyquist plots were made for the fresh and cycled (1000 cycles) coin cells (Figure 5.30 a, b). Fresh coin cell plot exhibits small diameter semicircles. Unlike the fresh coin cell, the cycled coin cell plot showed a large semicircle diameter which attributes to bigger charge transfer resistance (R_{ct}) built up upon cycling. The reason behind the wider R_{ct} is the partial decomposition of the electrolyte and the formation of inorganic and organic salts upon cycling, which might block the pores and minimize the sodium ions mobility toward the redox active sites in and out.[171] Furthermore, both coin cells possessed the 45° inclined line from the imaginary impedance resistance axis (-Z''). The 45° inclined line resembles a higher diffusive resistivity and thus a slower diffusion process of sodium ions into the bulk material of the electrode.[105,127] As a result, the small semicircle for the fresh coin cell and the 45° inclined line from the vertical axis confirm the pseudocapacitive behavior for a speedy surface-controlled Faradic process.[105] Resistance can be arisen due to three factors; the resistance of the electrolyte (R_{el})[117], the charge transfer resistance (R_{ct}), and Warburg resistance (R_w) for the diffusion process. Randles equivalent circuits were used to simulate and numerically analyze the Nyquist plots (Figure 5.30 c, d). The R_{el} can be obtained by the first intersection point of the semicircle with the

real impedance resistance axis (Z'). The R_{el} values for the fresh and cycled coin cells were 8.396 and 9.075 Ω, respectively. The R_{ct} can be determined by the diameter of the semicircle (the smaller is the faster in the charge transport). The fresh coin cell exhibits a lower diffusion resistance (8.078 Ω) unlike the cycled coin cell over 1000 cycles which showed a significant diffusion impedance (422.3 Ω). The R_w in our systems were obtained small to be 0.0743 and 0.00882 Ω for fresh and cycled coin cells respectively due to R_w is always associated with a R_{CT} and double layer capacitance (C).
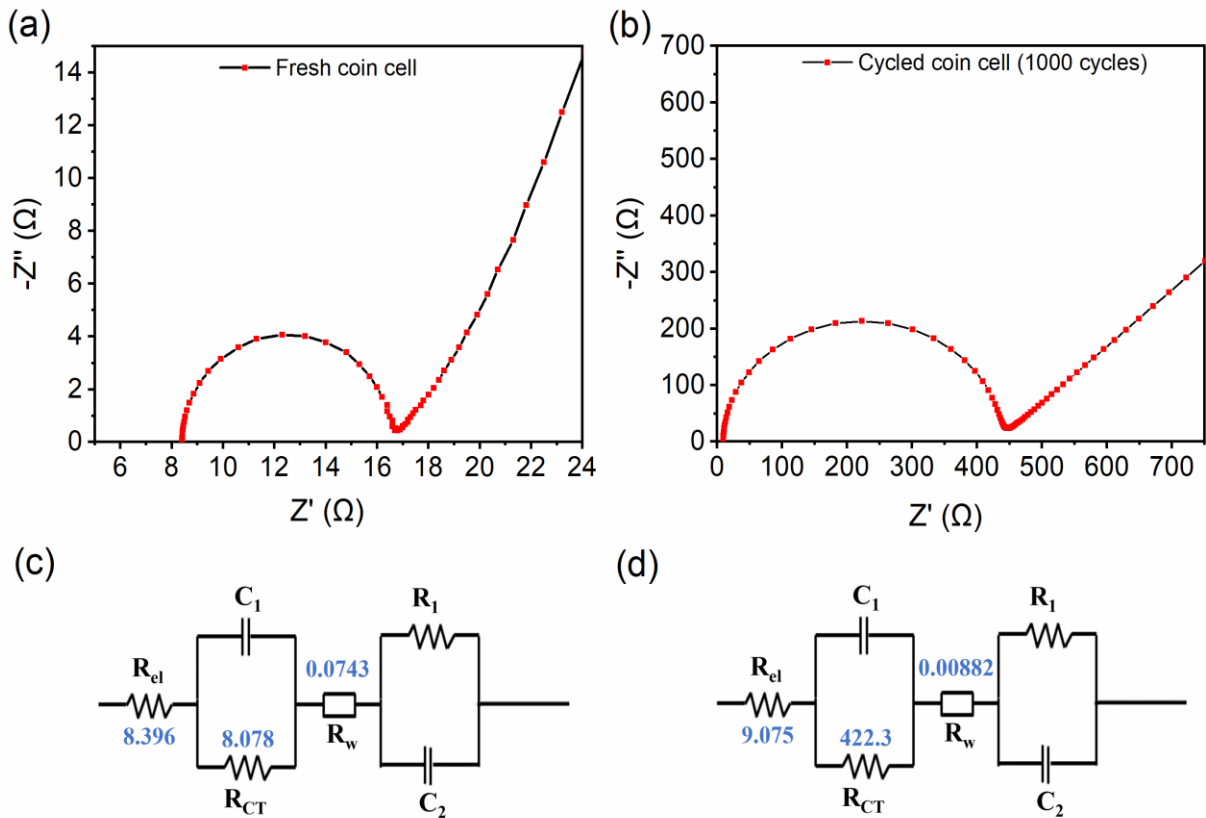
Figure 5.30 Electrochemical impedance spectra for a) battery before cycling and b) after 1000 cycles, c) simple equivalent Randles circuit diagram for the coin cells before cycling, and d) after cycling.

Based on the impedance data generated by Randles equivalent circuits, the total conductivity of the BILP-based electrode was calculated according to the equation

$$\sigma = \frac{t}{R_{tot}\,A}$$

Where σ is the total electrode conductivity, t is the electrode film thickness (Figure 5.31), R_{tot} is the total resistance ($R_{el} + R_{ct} + R_w$), and A is the electrode surface area (1.14 cm^2). The fresh coin cell exhibits a superior conductivity of 7.95 x 10^{-3} S m^{-1} which can be attributed to the small diffusion resistance and swift faradaic charge transfer R_{ct}. on the other hand, the 1000 cycled coin cell showed a lower conductivity of 3.05 x 10^{-4} S m^{-1} due to a slower charge transfer and sluggish ion diffusion built upon cycling.[105]
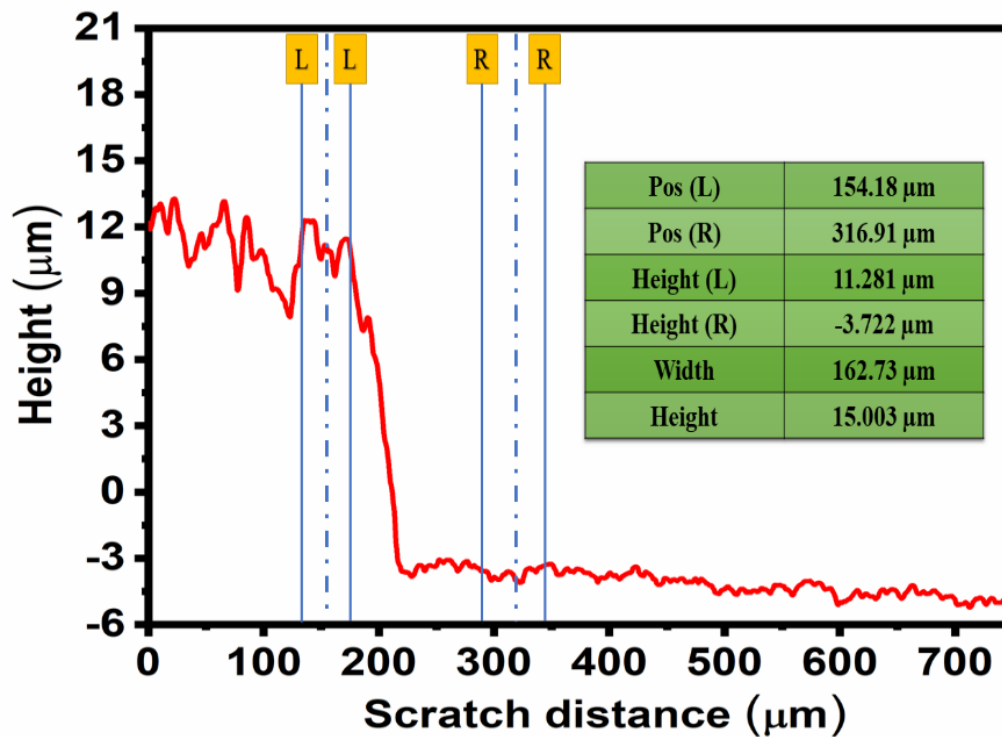
Figure 5.31 Electrode Film thickness measurement (15 µm).

The Aza-BILP based electrode performance was examined by the rate capability and long-term cycling stability. The Aza-BILP rate capability was performed to determine the charge exchange

kinetics in the 2D extended framework during sodiation and de-sodiation process. The electrode showed a stable reversible discharge specific capacity of 362, 311, 249, 196, 136, 104, 50 mA h g^{-1} at current rates of 0.1, 1, 3, 5, 8, 10, and 15 C, respectively. As the current rate was decreased back to 0.1 C, the discharge specific capacity of 365 mA h g^{-1} was reattained with 100% capacity recovery and proves the fast charge exchange kinetics during charge and discharge process (Figure 5.32 a, b). Furthermore, the capacity drop from 0.1 C to 1 C represents 14% only which is significantly low after tenfold current rate increasing. The rate capability outstanding performance might be attributed to the high surface area, high electronic conductivity and the honeycomb-like porous channels of BILP.[19] Charge/discharge hysteresis was clearly observed at 0.1 C because of the Na^+ ion depletion within the pores in the inner regions caused by the lower diffusion rate compared to the outermost areas of the BILP framework. This could restrict the Na^+ ions from being accessible to the aza-active sites.[130] On the other hand, all current rates higher than 0.1 C demonstrated an outstanding reversibility by showing no hysteresis between the charge and discharge processes. The rate capability figure showed the capacity drop at higher current rates which is attributed to the fast Na^+ ion-diffusion and thus lower the chance from reaching up the redox active sites.[128] To this end, we have utilized the impedance data to estimate the diffusion coefficient of Na^+ ions (D_{Na^+}) before (2.62 x 10^{-12} cm^2 s^{-1}) and after being cycled (5.25 x 10^{-14} cm^2 s^{-1}) (Figure 5.33).
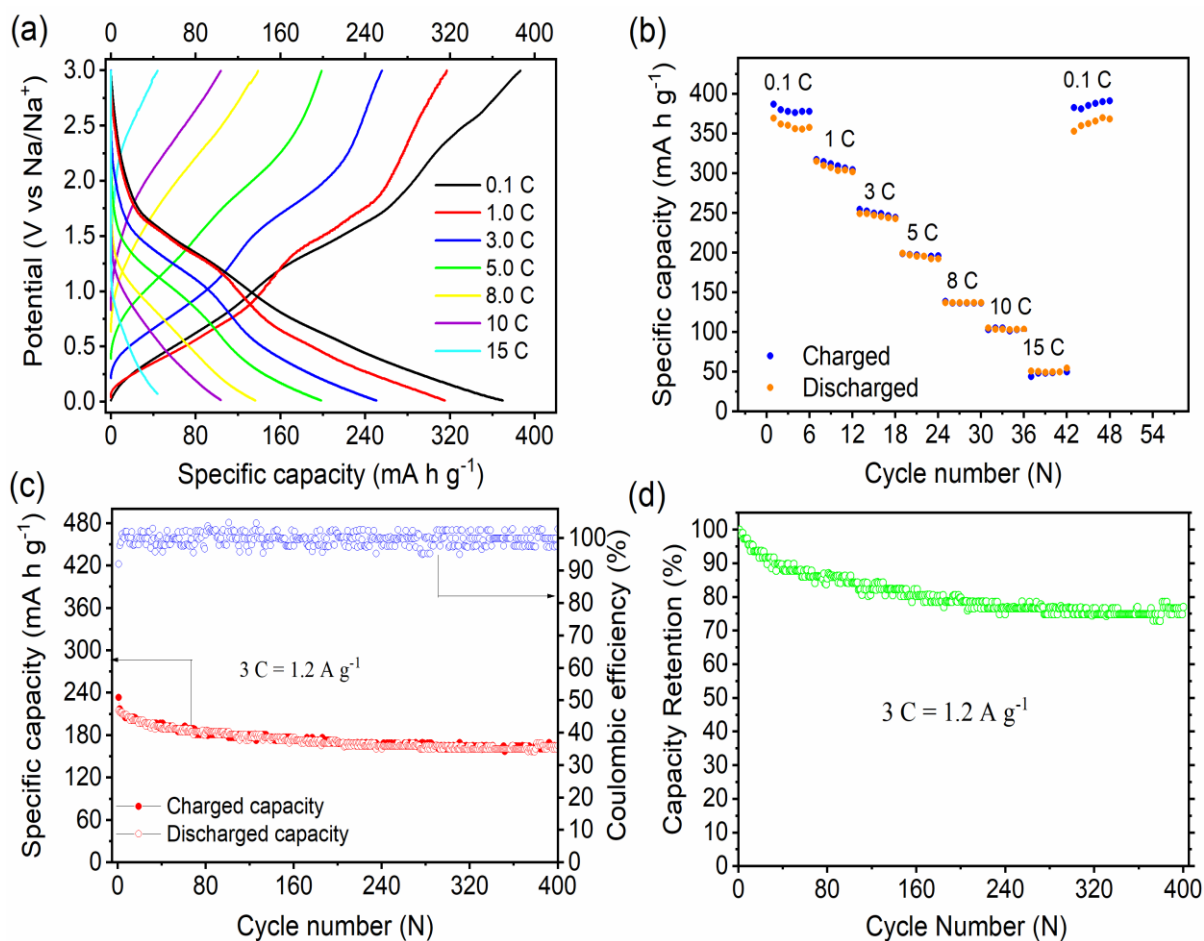
Figure 5.32 (a) Galvanostatic charge/discharge plots (b) Rate capability at different current rates vary from 0.1-15 C (c) Cycle stability and Coulombic efficiency over 400 cycles (d) capacity retention at 3 C over 400 cycles.

The long-term cycling performance of the Aza-BILP based electrode was performed over 400 cycles. The electrode demonstrated excellent stability with an outstanding coulombic efficiency of nearly 100% at 3 C (Figure 5.32 c). Furthermore, the electrode also exhibits a good capacity retention after 400 charge/discharge cycles of ~ 77 %. It is worth mentioning that the most capacity drop happened during the first 100 cycles which represents 70% of the total capacity drop (Figure 5.32 d). The highly π-conjugated and the insolubility nature of the Aza-BILP framework play an essential role in the remarkable cycling stability of the electrode by eliminating the framework

dissolution problems in the electrolyte and thereby decreasing the capacity drop and enhancing the ionic conductivity.[19]
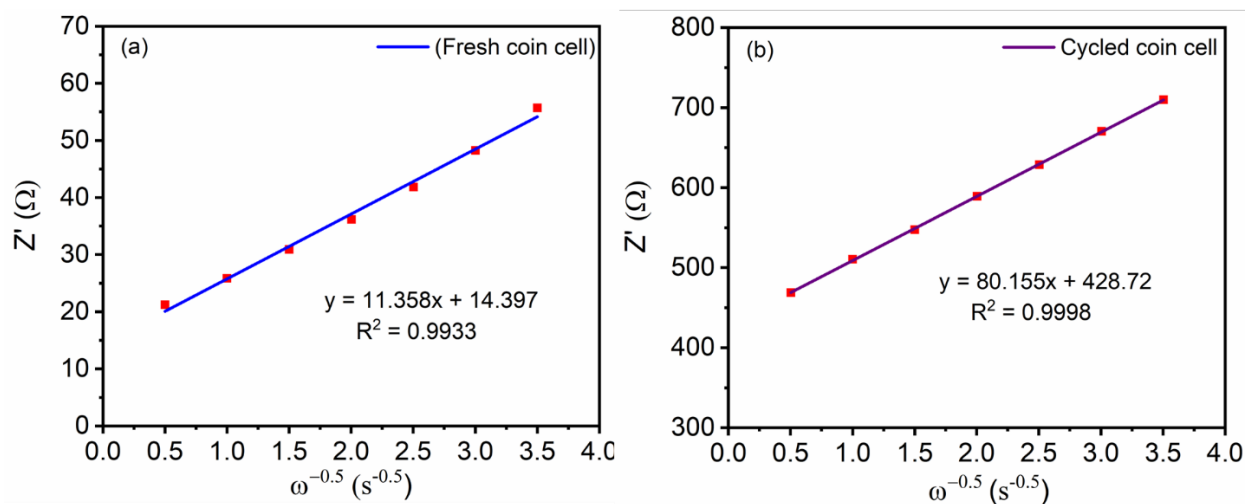
Figure 5.33 The plot of the real impedance resistance, Z′, vs. the reciprocal root square of the lower angular frequencies ($\omega^{-0.5}$) for (a) fresh battery and (b) after being cycled for 1000 cycles.

The redox mechanism (charge/discharge) of BILP-based electrodes was monitored by C 1s XPS and ATR-IR (Figure 5.34) during the sodiation and desodiation processes at three different stages: pristine, charged, and discharged. XPS and IR results exhibit the disappearance of the C=N pyrazine ring band at 286.6 eV and 1246 cm^{-1} respectively, when the electrode was discharged to 0.01 V, indicating the C-N-Na formation (Figure 5.34 b, d). However, the C=N band was reinstated when the electrode was recharged to 3.0 V showing the highly redox reversibility at the aza-centers (Figure 5.34 c). Furthermore, IR results show no contribution of C=C as a redox active site on the overall capacity at which C=C band positions at 1412 and 1600 cm^{-1} stayed intact in all three stages (pristine, charged, and discharged), indicating that the only contributions on the total capacity were by the aza redox active sites (Figure 5.34 d).
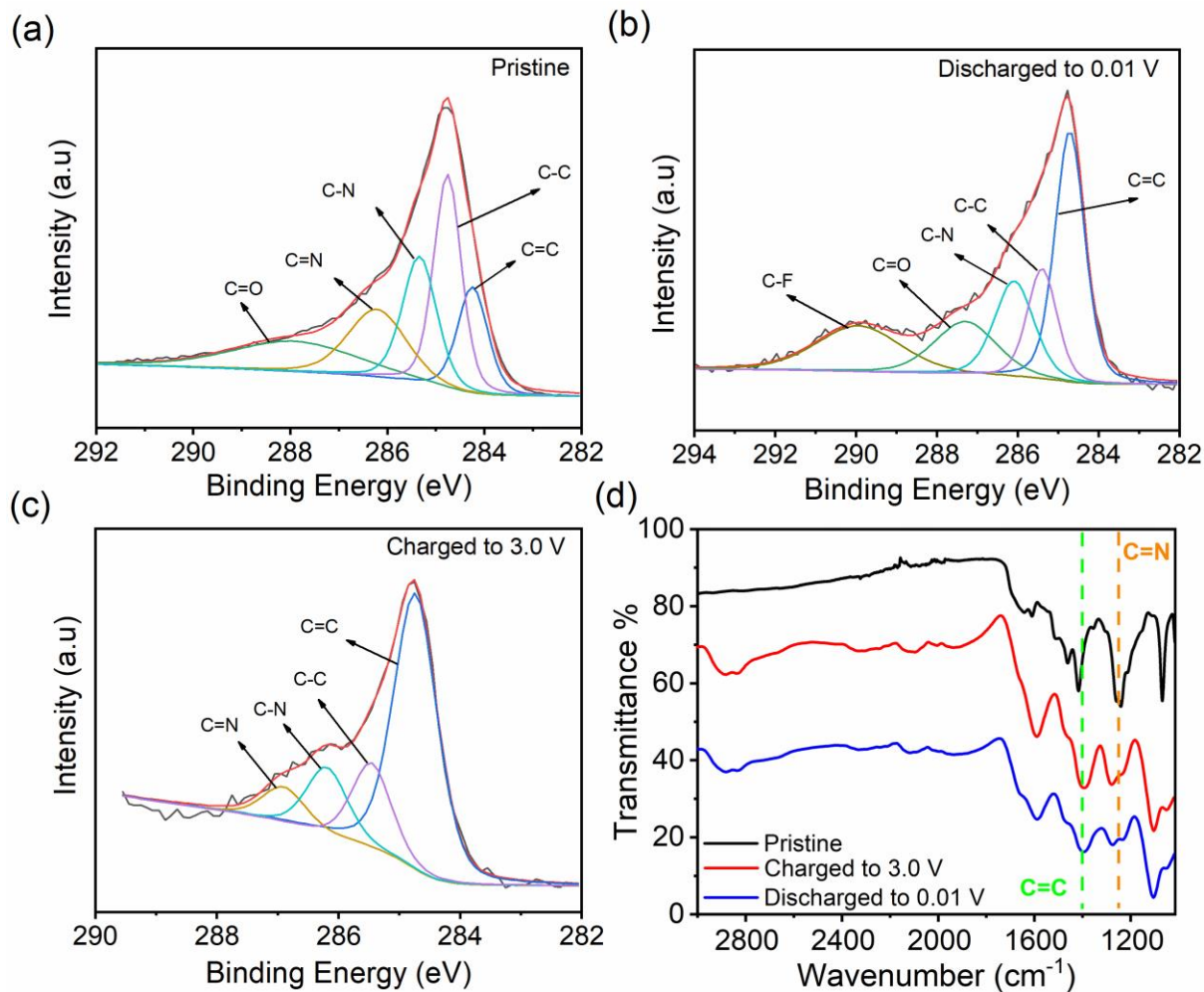
Figure 5.34 Deconvoluted C 1s XPS spectra of the BILP at different stages: (a) pristine, (b) discharge to 0.01 V, (c) charged to 3.0 V, and (d) ATR-IR for sodiation/desodiation mechanism investigation.

Energy density and power density were conducted to investigate the efficiency of the BILP based electrode on the energy storage and the amount of power per unit mass. At a current rate of 0.1 C, the Aza-BILP electrode demonstrated a remarkable energy density of 302 W h kg^{-1} (Figure 5.35 a), which is comparable to the best-performing inorganic and electrodes for SIBs.[39,134,135] Even at a high C rate of 5 C, BILP can still deliver a specific energy of 136 W h kg^{-1}, which corresponds to a remarkable specific power of 682 W kg^{-1} (Figure 5.35 b).
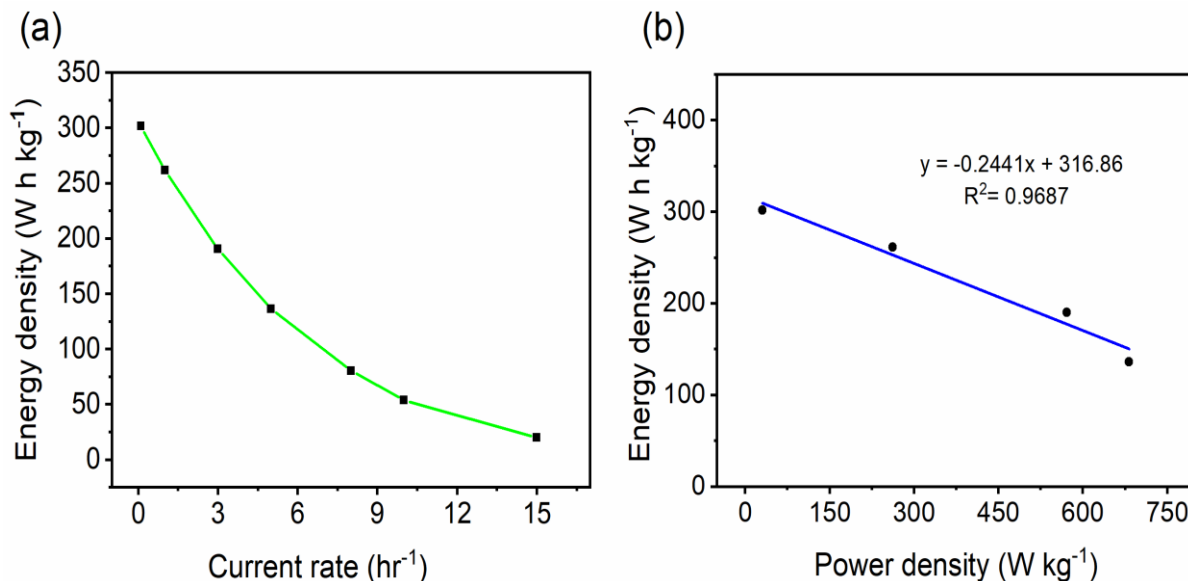
Figure 5.35 (a) Energy density of BILP-based electrode at different current rates of 0.1, 1, 3, 5, 8, 10, and 15 (b) Ragone plot for the 0.1, 1.0, 3.0, and 5.0 C.

5.4. Conclusion

In this work, we have successfully demonstrated the effective use of crystalline porous Aza-BILP in SIBs. The highly porous and π-conjugated nature of the framework facilitates rapid sodium ions diffusion and access to the redox-active aza sites. Aza-BILP based electrode demonstrated an outstanding charge/discharge specific capacity of 387/370 mA h g^{-1} at 0.1 C which contribute of 98.5 % and 94.1 %, respectively of the theoretical capacity of 393 mA h g^{-1} based on nine-electron redox reaction and the repeating unit molecular weight of 615 g/mol. This superior capacity delivery is attributed to the facile sodium ions diffusion into the highly ordered AA stacking system, the rapid surface-controlled Faradic process, and the high density of accessible redox-active sites per repeating unit. The Aza-BILP exhibits a pseudocapacitor like behavior which is essential for gathering both energy and power density in one system. Aza-BILP electrode showed a remarkable energy density of 302 W h kg^{-1} at 0.1 C and an outstanding specific power of 682 W

kg^{-1} at 5.0 C. Furthermore, the battery showed a great rate capability at different current rates from

0.1 to 15 C. Also exhibited very good stability over 400 cycles with a columbic efficiency of 100%.

Chapter 6. Conclusions & Perspectives

By tailoring the chemical composition and metrics of organic building blocks, novel redox properties can be integrated into extended π-conjugated Covalent Organic Frameworks (COFs) to advance electrode materials for rechargeable batteries. In this research, a set of highly crystalline, porous and conjugated 2D COFs was designed, modeled and synthesized for use as a green composite electrode material in rechargeable sodium batteries. Three categories of crystalline organic materials, Schiff bases-based COFs, polyimide-based COFs, and benzimidazole linked COFs were used as cathodic materials to evaluate their Na^+ ion storage capacity in sodium-ion batteries (SIBs). COFs-based cathodes in this work exhibited excellent electrochemical performances such as high specific capacity, excellent rate capability, and cycling stability due to the insoluble nature of the framework in the electrolyte and the high structural order of the conjugated frameworks, unlike small organic materials that dissolve in the electrolyte and eventually disintegrate from the current collector to cause inferior electrochemical performance especially rate capability and long term cycling stability.

Due to the high cost and scarce resources of lithium, sodium was used in a half cell configuration and the coin cells were fabricated and optimized for a competent electrochemical performance to lithium. Besides the lithium cost and limitations, LIBs fall short in sustainability due to the use of the toxic transition metal oxide as a part of the cathode in LIBs. Therefore, utilizing COFs as a green cathodic material of light weight and flexible nature would help in addressing the sustainability issue of LIBs and open the door for a new class of materials for electrode design from more abundant and renewable sources.

The electrochemical energy storage mechanism for the aforementioned active materials in this thesis was determined to be a pseudocapacitive in nature which combines the properties of surface-

controlled process (capacitor behavior) for power density applications and diffusion-controlled process (battery behavior) for energy density applications.

In chapter 3, we demonstrated the exceptional performance of Aza-COF in rechargeable SIBs. Aza-COF is a microporous 2D COF synthesized by a single step polycondensation reaction between hexaketocyclohexane (HKH) and 1,2,4,5-tetraaminobenzene (TAB), which affords phenazine-decorated channels and a theoretical specific capacity of 603 mA h g^{-1} based on six redox active sites per repeating unit. The Aza-COF-based electrode exhibits an exceptional average specific capacity (550 mA h g^{-1}), energy density (492 W h kg^{-1}) at 0.1 C, and power density (1182 W kg^{-1}) at 40 C. The high capacity and energy density are attributed to swift surface-controlled redox processes and rapid sodium-ion diffusion inside the porous electrode. Rate capability studies showed that the battery also performs well at high current rates; 1 C (363 mA h g^{-1}), 5 C (232 mA h g^{-1}), 10 C (161 mA h g^{-1}), and 20 C (103 mA h g^{-1}). In addition, the long-term cycling stability test revealed very good capacity retention (87% at 5 C).

In Chapter 4, we reported the synthesis of a redox-active pyrene-containing polyimide COF (PICOF-1) by linker exchange using an imine-linked COF as a template and demonstrate its performance in sodium-ion batteries (SIBs). The reported synthetic route based on linker exchange mitigates the challenges typically encountered with crystallizing chemically stable polyimide COFs from typical condensation reactions; thus, facilitating their rapid synthesis and purification. Using this approach, PICOF-1 exhibits high crystallinity with very low refinement parameters R_P and R_{WP} of 0.415% and 0.326%, respectively. PICOF-1 has a high Brunauer-Emmette-Teller (BET) surface area of 924 m^2 g^{-1} and well-defined 1D channels of 2.78 x 1.91 nm, which enable fast ion transport and charge transfer, reaching a capacity at 0.1 C of almost nearly as its theoretical capacity and maintaining 99% coulombic efficiency over 175 cycles at 0.3 C. Our study

demonstrates that imine-linked COFs are effective templates for integrating carbonyl-rich polyimide moieties into high-surface COFs to advance electrochemical energy storage applications.

In Chapter 5, the overarching goal of this project was to establish the use of a crystalline redox-active Aza-BILP as highly efficient green electrodes for SIBs. Aza-BILP was synthesized from condensation of aryl-hexamine monomers, and terephthalaldehyde in a glass ampule to afford decorated nine aza bonds (-N=C-) undergo reversible redox reactions with sodium with a theoretical specific capacity of 392 mA h g^{-1}. Furthermore, the crystalline Aza-BILP forms eclipsed AA hexagonal layer stacking with a mesoporous nature and high surface area that facilitates fast ionic mobility and accessibility of the redox-active sites enabling high rate capability at high current rates. Furthermore, Aza-BILP possesses a high surface area and pore diameter of 33 Å, which would accommodate bigger ions for sustainable batteries beyond lithium and sodium (i.e., K^+_+, Mg^{2+}, and Al^{3+}).

The theoretical data on crystalline COFs in the reported projects were obtained by using Materials Studio modeling software. This was a powerful tool to model the eclipsed and staggered conformations, simulate powder-XRD patterns, estimate the theoretical surface areas, and measure the pore size and the interlayer spacing distance (d-spacing) of the COFs. Future work should focus on the post-synthesis modification of COFs and morphology control to enhance the rate capability and long-term stability of SIBs. The presence of reactive sites like the pyrrolic nitrogen in the imidazole ring would help in introducing side chains (mainly ether side chains) inside the pores to increase sodium ions transport rate and enhance the ion mobility, especially at high C rates. However, such modification should not compromise the energy density of COF-based batteries.

References

(1)   Soloveichik, G. L. Battery Technologies for Large-Scale Stationary Energy Storage. *Annu. Rev. Chem. Biomol. Eng.* **2011**, *2* (1), 503–527.

(2)   US Energy Information Administration. International Energy Outlook. (2017). https://www.eia.gov/todayinenergy/detail.php?id=41433 (accessed Apr 5, 2020).

(3)   Li, M.; Lu, J.; Chen, Z.; Amine, K. 30 Years of Lithium-Ion Batteries. *Adv. Mater.* **2018**, *30* (33), 1–24.

(4)   Goodenough, J. B.; Park, K. S. The Li-Ion Rechargeable Battery: A Perspective. *J. Am. Chem. Soc.* **2013**, *135* (4), 1167–1176.

(5)   Xu, J.; Dou, Y.; Wei, Z.; Ma, J.; Deng, Y.; Li, Y.; Liu, H.; Dou, S. Recent Progress in Graphite Intercalation Compounds for Rechargeable Metal (Li, Na, K, Al)-Ion Batteries. *Adv. Sci.* **2017**, *4* (10), 1700146.

(6)   Madian, M.; Eychmüller, A.; Giebeler, L. Current Advances in Tio 2 -Based Nanostructure Electrodes for High Performance Lithium Ion Batteries. *Batteries* **2018**, *4* (1), 7.

(7)   Chen, H.; Armand, M.; Demailly, G.; Dolhem, F.; Poizot, P.; Tarascon, J. M. From Biomass to a Renewable LiXC6O6 Organic Electrode for Sustainable Li-Ion Batteries. *ChemSusChem* **2008**, *1* (4), 348–355.

(8)   Schon, T. B.; McAllister, B. T.; Li, P. F.; Seferos, D. S. The Rise of Organic Electrode Materials for Energy Storage. *Chem. Soc. Rev.* **2016**, *45* (22), 6345–6404.

(9)   Xie, J.; Zhang, Q. Recent Progress in Rechargeable Lithium Batteries with Organic Materials as Promising Electrodes. *J. Mater. Chem. A* **2016**, *4* (19), 7091–7106.

(10) Zhu, Z.; Chen, J. Review—Advanced Carbon-Supported Organic Electrode Materials for Lithium (Sodium)-Ion Batteries. *J. Electrochem. Soc.* **2015**, *162* (14), A2393–A2405.

(11) Muench, S.; Wild, A.; Friebe, C.; Häupler, B.; Janoschka, T.; Schubert, U. S. Polymer-Based Organic Batteries. *Chem. Rev.* **2016**, *116* (16), 9438–9484.

(12) Song, Z.; Zhou, H. Towards Sustainable and Versatile Energy Storage Devices: An Overview of Organic Electrode Materials. *Energy Environ. Sci.* **2013**, *6* (8), 2280–2301.

(13) Liang, Y.; Zhang, P.; Yang, S.; Tao, Z.; Chen, J. Fused Heteroaromatic Organic Compounds for High-Power Electrodes of Rechargeable Lithium Batteries. *Adv. Energy Mater.* **2013**, *3* (5), 600–605.

(14) Zhao, Q.; Guo, C.; Lu, Y.; Liu, L.; Liang, J.; Chen, J. Rechargeable Lithium Batteries with Electrodes of Small Organic Carbonyl Salts and Advanced Electrolytes. *Ind. Eng. Chem. Res.* **2016**, *55* (20), 5795–5804.

(15) Zhang, Y.; Wang, J.; Riduan, S. N. Strategies toward Improving the Performance of Organic Electrodes in Rechargeable Lithium (Sodium) Batteries. *J. Mater. Chem. A* **2016**, *4* (39), 14902–14914.

(16) Larcher, D.; Tarascon, J. M. Towards Greener and More Sustainable Batteries for Electrical Energy Storage. *Nat. Chem.* **2015**, *7* (1), 19–29.

(17) Armand, M.; Grugeon, S.; Vezin, H.; Laruelle, S.; Ribière, P.; Poizot, P.; Tarascon, J. M. Conjugated Dicarboxylate Anodes for Li-Ion Batteries. *Nat. Mater.* **2009**, *8* (2), 120–125.

(18) Gu, S.; Wu, S.; Cao, L.; Li, M.; Qin, N.; Zhu, J.; Wang, Z.; Li, Y.; Li, Z.; Chen, J.; Lu, Z. Tunable Redox Chemistry and Stability of Radical Intermediates in 2D Covalent Organic

Frameworks for High Performance Sodium Ion Batteries. *J. Am. Chem. Soc.* **2019**, *141* (24), 9623–9628.

(19)   Shi, R.; Liu, L.; Lu, Y.; Wang, C.; Li, Y.; Li, L.; Yan, Z.; Chen, J. Nitrogen-Rich Covalent Organic Frameworks with Multiple Carbonyls for High-Performance Sodium Batteries. *Nat. Commun.* **2020**, *11* (1), 178.

(20)   Wang, J.; Lee, Y.; Tee, K.; Riduan, S. N.; Zhang, Y. A Nanoporous Sulfur-Bridged Hexaazatrinaphthylene Framework as an Organic Cathode for Lithium Ion Batteries with Well-Balanced Electrochemical Performance. *Chem. Commun.* **2018**, *54* (55), 7681–7684.

(21)   Castillo-Martínez, E.; Carretero-González, J.; Armand, M. Polymeric Schiff Bases as Low-Voltage Redox Centers for Sodium-Ion Batteries. *Angew. Chemie - Int. Ed.* **2014**, *53* (21), 5341–5345.

(22)   Luo, C.; Xu, G. L.; Ji, X.; Hou, S.; Chen, L.; Wang, F.; Jiang, J.; Chen, Z.; Ren, Y.; Amine, K.; Wang, C. Reversible Redox Chemistry of Azo Compounds for Sodium-Ion Batteries. *Angew. Chemie - Int. Ed.* **2018**, *57* (11), 2879–2883.

(23)   Yao, M.; Kuratani, K.; Kojima, T.; Takeichi, N.; Senoh, H.; Kiyobayashi, T. Indigo Carmine: An Organic Crystal as a Positive-Electrode Material for Rechargeable Sodium Batteries. *Sci. Rep.* **2014**, *4*, 3650.

(24)   Hong, J.; Lee, M.; Lee, B.; Seo, D. H.; Park, C. B.; Kang, K. Biologically Inspired Pteridine Redox Centres for Rechargeable Batteries. *Nat. Commun.* **2014**, *5*, 5335.

(25)   Wang, J.; Chen, C. S.; Zhang, Y. Hexaazatrinaphthylene-Based Porous Organic Polymers as Organic Cathode Materials for Lithium-Ion Batteries. *ACS Sustain. Chem. Eng.* **2018**, *6*

(2), 1772–1779.

(26)   Xu, Y.; Zhou, M.; Lei, Y. Organic Materials for Rechargeable Sodium-Ion Batteries. *Mater. Today* **2018**, *21* (1), 60–78.

(27)   Wang, J.; Tee, K.; Lee, Y.; Riduan, S. N.; Zhang, Y. Hexaazatriphenylene Derivatives/GO Composites as Organic Cathodes for Lithium Ion Batteries. *J. Mater. Chem. A* **2018**, *6* (6), 2752–2757.

(28)   Jaffe, A.; Saldivar Valdes, A.; Karunadasa, H. I. Quinone-Functionalized Carbon Black Cathodes for Lithium Batteries with High Power Densities. *Chem. Mater.* **2015**, *27* (10), 3568–3571.

(29)   Shea, J. J.; Luo, C. Organic Electrode Materials for Metal Ion Batteries. *ACS Appl. Mater. Interfaces* **2020**, *12* (5), 5361–5380.

(30)   Shehab, M. K.; Weeraratne, K. S.; El-Kadri, O. M.; Yadavalli, V. K.; El-Kaderi, H. M. Templated Synthesis of 2D Polyimide Covalent Organic Framework for Rechargeable Sodium-Ion Batteries. *Macromol. Rapid Commun.* **2022**, 2200782.

(31)   Rodríguez-Pérez, I. A.; Yuan, Y.; Bommier, C.; Wang, X.; Ma, L.; Leonard, D. P.; Lerner, M. M.; Carter, R. G.; Wu, T.; Greaney, P. A.; Lu, J.; Ji, X. Mg-Ion Battery Electrode: An Organic Solid's Herringbone Structure Squeezed upon Mg-Ion Insertion. *J. Am. Chem. Soc.* **2017**, *139* (37), 13031–13037.

(32)   Han, X.; Qing, G.; Sun, J.; Sun, T. How Many Lithium Ions Can Be Inserted onto Fused C 6 Aromatic Ring Systems? *Angew. Chemie - Int. Ed.* **2012**, *51* (21), 5147–5151.

(33)   Wang, H. G.; Yuan, S.; Si, Z.; Zhang, X. B. Multi-Ring Aromatic Carbonyl Compounds

Enabling High Capacity and Stable Performance of Sodium-Organic Batteries. *Energy Environ. Sci.* **2015**, *8* (11), 3160–3165.

(34)   Wu, Y.; Zeng, R.; Nan, J.; Shu, D.; Qiu, Y.; Chou, S.-L. Quinone Electrode Materials for Rechargeable Lithium/Sodium Ion Batteries. *Adv. Energy Mater.* **2017**, *7* (24), 1700278.

(35)   Ke, H.; Zhang, Q.; Zhang, X.; Cheng, G.; Sun, Y.; Li, J.; Cheng, H. Hydroquinone-Based Conjugated Schiff Base Polymer as Anode Material for Lithium Ion Batteries. *Mater. Lett.* **2021**, *286*, 129235.

(36)   Lu, Z.; Sui, F.; Miao, Y. E.; Liu, G.; Li, C.; Dong, W.; Cui, J.; Liu, T.; Wu, J.; Yang, C. Polyimide Separators for Rechargeable Batteries. *J. Energy Chem.* **2021**, *58*, 170–197.

(37)   Qin, H.; Song, Z. P.; Zhan, H.; Zhou, Y. H. Aqueous Rechargeable Alkali-Ion Batteries with Polyimide Anode. *J. Power Sources* **2014**, *249*, 367–372.

(38)   Xu, F.; Wang, H.; Lin, J.; Luo, X.; Cao, S. A.; Yang, H. Poly(Anthraquinonyl Imide) as a High Capacity Organic Cathode Material for Na-Ion Batteries. *J. Mater. Chem. A* **2016**, *4* (29), 11491–11497.

(39)   Shehab, M. K.; Weeraratne, K. S.; Huang, T.; Lao, K. U.; El-Kaderi, H. M. Exceptional Sodium-Ion Storage by an Aza-Covalent Organic Framework for High Energy and Power Density Sodium-Ion Batteries. *ACS Appl. Mater. Interfaces* **2021**, *13* (13), 15083–15091.

(40)   Peng, C.; Ning, G. H.; Su, J.; Zhong, G.; Tang, W.; Tian, B.; Su, C.; Yu, Di.; Zu, L.; Yang, J.; Ng, M. F.; Hu, Y. S.; Yang, Y.; Armand, M.; Loh, K. P. Reversible Multi-Electron Redox Chemistry of π-Conjugated N-Containing Heteroaromatic Molecule-Based Organic Cathodes. *Nat. Energy* **2017**, *2,* 17074.

(41)   Song, Z.; Qian, Y.; Zhang, T.; Otani, M.; Zhou, H. Poly(Benzoquinonyl Sulfide) as a High-Energy Organic Cathode for Rechargeable Li and Na Batteries. *Adv. Sci.* **2015**, *2* (9), 1500124.

(42)   Deng, W.; Liang, X.; Wu, X.; Qian, J.; Cao, Y.; Ai, X.; Feng, J.; Yang, H. A Low Cost, All-Organic Na-Ion Battery Based on Polymeric Cathode and Anode. *Sci. Rep.* **2013**, *3* (1), 2671.

(43)   Zhou, M.; Zhu, L.; Cao, Y.; Zhao, R.; Qian, J.; Ai, X.; Yang, H. Fe(CN) 6-4-Doped Polypyrrole: A High-Capacity and High-Rate Cathode Material for Sodium-Ion Batteries. *RSC Adv.* **2012**, *2* (13), 5495–5498.

(44)   Wang, H. G.; Yuan, S.; Ma, D. L.; Huang, X. L.; Meng, F. L.; Zhang, X. B. Tailored Aromatic Carbonyl Derivative Polyimides for High-Power and Long-Cycle Sodium-Organic Batteries. *Adv. Energy Mater.* **2014**, *4* (7), 1301651.

(45)   Zhu, H.; Yin, J.; Zhao, X.; Wang, C.; Yang, X. Humic Acid as Promising Organic Anodes for Lithium/Sodium Ion Batteries. *Chem. Commun.* **2015**, *51* (79), 14708–14711.

(46)   Zhao, R.; Zhu, L.; Cao, Y.; Ai, X.; Yang, H. X. An Aniline-Nitroaniline Copolymer as a High Capacity Cathode for Na-Ion Batteries. *Electrochem. commun.* **2012**, *21* (1), 36–38.

(47)   Zhou, M.; Xiong, Y.; Cao, Y.; Ai, X.; Yang, H. Electroactive Organic Anion-Doped Polypyrrole as a Low Cost and Renewable Cathode for Sodium-Ion Batteries. *J. Polym. Sci. Part B Polym. Phys.* **2013**, *51* (2), 114–118.

(48)   Han, S. C.; Bae, E. G.; Lim, H.; Pyo, M. Non-Crystalline Oligopyrene as a Cathode Material with a High-Voltage Plateau for Sodium Ion Batteries. *J. Power Sources* **2014**, *254*, 73–79.

(49) Shen, Y. F.; Yuan, D. D.; Ai, X. P.; Yang, H. X.; Zhou, M. Poly(Diphenylaminesulfonic Acid Sodium) as a Cation-Exchanging Organic Cathode for Sodium Batteries. *Electrochem. commun.* **2014**, *49*, 5–8.

(50) Banda, H.; Damien, D.; Nagarajan, K.; Hariharan, M.; Shaijumon, M. M. A Polyimide Based All-Organic Sodium Ion Battery. *J. Mater. Chem. A* **2015**, *3* (19), 10453–10458.

(51) Chen, L.; Li, W.; Wang, Y.; Wang, C.; Xia, Y. Polyimide as Anode Electrode Material for Rechargeable Sodium Batteries. *RSC Adv.* **2014**, *4* (48), 25369–25373.

(52) Deng, W.; Shen, Y.; Qian, J.; Yang, H. A Polyimide Anode with High Capacity and Superior Cyclability for Aqueous Na-Ion Batteries. *Chem. Commun.* **2015**, *51* (24), 5097–5099.

(53) Dong, X.; Chen, L.; Liu, J.; Haller, S.; Wang, Y.; Xia, Y. Environmentally-Friendly Aqueous Li (or Na)-Ion Battery with Fast Electrode Kinetics and Super-Long Life. *Sci. Adv.* **2016**, *2* (1), e1501038.

(54) Gu, T.; Zhou, M.; Liu, M.; Wang, K.; Cheng, S.; Jiang, K. A Polyimide-MWCNTs Composite as High Performance Anode for Aqueous Na-Ion Batteries. *RSC Adv.* **2016**, *6* (58), 53319–53323.

(55) Xu, F.; Xia, J.; Shi, W.; Cao, S. A. Sulfonyl-Based Polyimide Cathode for Lithium and Sodium Secondary Batteries: Enhancing the Cycling Performance by the Electrolyte. *Mater. Chem. Phys.* **2016**, *169*, 192–197.

(56) Xu, F.; Xia, J.; Shi, W. Anthraquinone-Based Polyimide Cathodes for Sodium Secondary Batteries. *Electrochem. commun.* **2015**, *60*, 117–120.

(57)   Li, Z.; Zhou, J.; Xu, R.; Liu, S.; Wang, Y.; Li, P.; Wu, W.; Wu, M. Synthesis of Three Dimensional Extended Conjugated Polyimide and Application as Sodium-Ion Battery Anode. *Chem. Eng. J.* **2016**, *287*, 516–522.

(58)   Zhu, L.; Niu, Y.; Cao, Y.; Lei, A.; Ai, X.; Yang, H. N-Type Redox Behaviors of Polybithiophene and Its Implications for Anodic Li and Na Storage Materials. *Electrochim. Acta* **2012**, *78*, 27–31.

(59)   Kim, J. K.; Kim, Y. Y.; Park, S.; Ko, H.; Kim, Y. Y. Encapsulation of Organic Active Materials in Carbon Nanotubes for Application to High-Electrochemical-Performance Sodium Batteries. *Energy Environ. Sci.* **2016**, *9* (4), 1264–1269.

(60)   López-Herraiz, M.; Castillo-Martínez, E.; Carretero-González, J.; Carrasco, J.; Rojo, T.; Armand, M. Oligomeric-Schiff Bases as Negative Electrodes for Sodium Ion Batteries: Unveiling the Nature of Their Active Redox Centers. *Energy Environ. Sci.* **2015**, *8* (11), 3233–3241.

(61)   Sakaushi, K.; Hosono, E.; Nickerl, G.; Gemming, T.; Zhou, H.; Kaskel, S.; Eckert, J. Aromatic Porous-Honeycomb Electrodes for a Sodium-Organic Energy Storage Device. *Nat. Commun.* **2013**, *4* (1), 1485.

(62)   Zhang, S.; Huang, W.; Hu, P.; Huang, C.; Shang, C.; Zhang, C.; Yang, R.; Cui, G. Conjugated Microporous Polymers with Excellent Electrochemical Performance for Lithium and Sodium Storage. *J. Mater. Chem. A* **2015**, *3* (5), 1896–1901.

(63)   Sakaushi, K.; Hosono, E.; Nickerl, G.; Zhou, H.; Kaskel, S.; Eckert, J. Bipolar Porous Polymeric Frameworks for Low-Cost, High-Power, Long-Life All-Organic Energy Storage Devices. *J. Power Sources* **2014**, *245*, 553–556.

137

(64) Sun, T.; Li, Z.; Wang, H.; Bao, D.; Meng, F.; Zhang, X. A Biodegradable Polydopamine-Derived Electrode Material for High-Capacity and Long-Life Lithium-Ion and Sodium-Ion Batteries. *Angew. Chemie Int. Ed.* **2016**, *55* (36), 10662–10666.

(65) Zhou, M.; Li, W.; Gu, T.; Wang, K.; Cheng, S.; Jiang, K. A Sulfonated Polyaniline with High Density and High Rate Na-Storage Performances as a Flexible Organic Cathode for Sodium Ion Batteries. *Chem. Commun.* **2015**, *51* (76), 14354–14356.

(66) Zhu, X.; Zhao, R.; Deng, W.; Ai, X.; Yang, H.; Cao, Y. An All-Solid-State and All-Organic Sodium-Ion Battery Based on Redox-Active Polymers and Plastic Crystal Electrolyte. *Electrochim. Acta* **2015**, *178*, 55–59.

(67) Su, D.; Zhang, J.; Dou, S.; Wang, G. Polypyrrole Hollow Nanospheres: Stable Cathode Materials for Sodium-Ion Batteries. *Chem. Commun.* **2015**, *51* (89), 16092–16095.

(68) Chen, X.; Liu, L.; Yan, Z.; Huang, Z.; Zhou, Q.; Guo, G.; Wang, X. The Excellent Cycling Stability and Superior Rate Capability of Polypyrrole as the Anode Material for Rechargeable Sodium Ion Batteries. *RSC Adv.* **2016**, *6* (3), 2345–2351.

(69) Diercks, C. S.; Yaghi, O. M. The Atom, the Molecule, and the Covalent Organic Framework. *Science* **2017**, *355* (6328), No. eaal 1585.

(70) Côté, A. P.; Benin, A. I.; Ockwig, N. W.; O'Keeffe, M.; Matzger, A. J.; Yaghi, O. M. Chemistry: Porous, Crystalline, Covalent Organic Frameworks. *Science* **2005**, *310* (5751), 1166–1170.

(71) Haldar, S.; Roy, K.; Nandi, S.; Chakraborty, D.; Puthusseri, D.; Gawli, Y.; Ogale, S.; Vaidhyanathan, R. High and Reversible Lithium Ion Storage in Self-Exfoliated Triazole-

Triformyl Phloroglucinol-Based Covalent Organic Nanosheets. *Adv. Energy Mater.* **2018**, *8* (8), 1702170.

(72)   Lei, Z.; Yang, Q.; Xu, Y.; Guo, S.; Sun, W.; Liu, H.; Lv, L. P.; Zhang, Y.; Wang, Y. Boosting Lithium Storage in Covalent Organic Framework via Activation of 14-Electron Redox Chemistry. *Nat. Commun.* **2018**, *9* (1), 576.

(73)   Ashourirad, B.; Arab, P.; Islamoglu, T.; Cychosz, K. A.; Thommes, M.; El-Kaderi, H. M. A Cost-Effective Synthesis of Heteroatom-Doped Porous Carbons as Efficient CO2 Sorbents. *J. Mater. Chem. A* **2016**, *4* (38), 14693–14702.

(74)   Rabbani, M. G.; Sekizkardes, A. K.; El-Kadri, O. M.; Kaafarani, B. R.; El-Kaderi, H. M. Pyrene-Directed Growth of Nanoporous Benzimidazole-Linked Nanofibers and Their Application to Selective CO2 Capture and Separation. *J. Mater. Chem.* **2012**, *22* (48), 25409–25417.

(75)   Fang, Q.; Wang, J.; Gu, S.; Kaspar, R. B.; Zhuang, Z.; Zheng, J.; Guo, H.; Qiu, S.; Yan, Y. 3D Porous Crystalline Polyimide Covalent Organic Frameworks for Drug Delivery. *J. Am. Chem. Soc.* **2015**, *137* (26), 8352–8355.

(76)   Ding, S. Y.; Gao, J.; Wang, Q.; Zhang, Y.; Song, W. G.; Su, C. Y.; Wang, W. Construction of Covalent Organic Framework for Catalysis: Pd/COF-LZU1 in Suzuki-Miyaura Coupling Reaction. *J. Am. Chem. Soc.* **2011**, *133* (49), 19816–19822.

(77)   Mulzer, C. R.; Shen, L.; Bisbey, R. P.; McKone, J. R.; Zhang, N.; Abruña, H. D.; Dichtel, W. R. Superior Charge Storage and Power Density of a Conducting Polymer-Modified Covalent Organic Framework. *ACS Cent. Sci.* **2016**, *2* (9), 667–673.

(78) Deblase, C. R.; Silberstein, K. E.; Truong, T. T.; Abruña, H. D.; Dichtel, W. R. Β-Ketoenamine-Linked Covalent Organic Frameworks Capable of Pseudocapacitive Energy Storage. *J. Am. Chem. Soc.* **2013**, *135* (45), 16821–16824.

(79) Meng, Z.; Aykanat, A.; Mirica, K. A. Proton Conduction in 2D Aza-Fused Covalent Organic Frameworks. *Chem. Mater.* **2019**, *31* (3), 819–825.

(80) Patra, B. C.; Das, S. K.; Ghosh, A.; Raj, A. K.; Moitra, P.; Addicoat, M.; Mitra, S.; Bhaumik, A.; Bhattacharya, S.; Pradhan, A. Covalent Organic Framework Based Microspheres as an Anode Material for Rechargeable Sodium Batteries. *J. Mater. Chem. A* **2018**, *6* (34), 16655–16663.

(81) Weeraratne, K. S.; Alzharani, A. A.; El-Kaderi, H. M. Redox-Active Porous Organic Polymers as Novel Electrode Materials for Green Rechargeable Sodium-Ion Batteries. *ACS Appl. Mater. Interfaces* **2019**, *11* (26), 23520–23526.

(82) Wang, J.; En, J. C. Z.; Riduan, S. N.; Zhang, Y. Nitrogen-Linked Hexaazatrinaphthylene Polymer as Cathode Material in Lithium-Ion Battery. *Chem. - A Eur. J.* **2020**, *26* (12), 2581–2585.

(83) Dunn, B.; Kamath, H.; Tarascon, J. M. Electrical Energy Storage for the Grid: A Battery of Choices. *Science* **2011**, *334* (6058), 928–935.

(84) Parker, J. F.; Chervin, C. N.; Pala, I. R.; Machler, M.; Burz, M. F.; Long, J. W.; Rolison, D. R. Rechargeable Nickel−3D Zinc Batteries: An Energy-Dense, Safer Alternative to Lithium-Ion. *Science* **2017**, *356* (6336), 415−418.

(85) Choi, J. W.; Aurbach, D. Promise and Reality of Post-Lithium-Ion Batteries with High

Energy Densities. *Nat. Rev. Mater.* **2016**, *1*, 16013.

(86)   Kapaev, R. R.; Zhidkov, I. S.; Kurmaev, E. Z.; Stevenson, K. J.; Troshin, P. A. Hexaazatriphenylene-Based Polymer Cathode for Fast and Stable Lithium-, Sodium- And Potassium-Ion Batteries. *J. Mater. Chem. A* **2019**, *7* (39), 22596–22603.

(87)   Kim, Y. J. o.; Wu, W.; Chun, S. E.; Whitacre, J. F.; Bettinger, C. J. Catechol-Mediated Reversible Binding of Multivalent Cations in Eumelanin Half-Cells. *Adv. Mater.* **2014**, *26* (38), 6572–6579.

(88)   Reed, L. D.; Ortiz, S. N.; Xiong, M.; Menke, E. J. A Rechargeable Aluminum-Ion Battery Utilizing a Copper Hexacyanoferrate Cathode in an Organic Electrolyte. *Chem. Commun.* **2015**, *51* (76), 14397–14400.

(89)   Mao, M.; Luo, C.; Pollard, T. P.; Hou, S.; Gao, T.; Fan, X.; Cui, C.; Yue, J.; Tong, Y.; Yang, G.; Deng, T.; Zhang, M.; Ma, J.; Suo, L.; Borodin, O.; Wang, C. A Pyrazine-Based Polymer for Fast-Charge Batteries. *Angew. Chemie - Int. Ed.* **2019**, *58* (49), 17820–17826.

(90)   Geng, K.; He, T.; Liu, R.; Dalapati, S.; Tan, K. T.; Li, Z.; Tao, S.; Gong, Y.; Jiang, Q.; Jiang, D. Covalent Organic Frameworks: Design, Synthesis, and Functions. *Chem. Rev.* **2020**, *120*, 8814-8933.

(91)   Rabbani, M. G.; El-Kaderi, H. M. Synthesis and Characterization of Porous Benzimidazole-Linked Polymers and Their Performance in Small Gas Storage and Selective Uptake. *Chem. Mater.* **2012**, *24* (8), 1511–1517.

(92)   Wang, P. L.; Ding, S. Y.; Zhang, Z. C.; Wang, Z. P.; Wang, W. Constructing Robust Covalent Organic Frameworks via Multicomponent Reactions. *J. Am. Chem. Soc.* **2019**,

141 (45), 18004–18008.

(93)   Das, P.; Mandal, S. K. In-Depth Experimental and Computational Investigations for Remarkable Gas/Vapor Sorption, Selectivity, and Affinity by a Porous Nitrogen-Rich Covalent Organic Framework. *Chem. Mater.* **2019**, *31* (5), 1584–1596.

(94)   Ranjeesh, K. C.; Illathvalappil, R.; Veer, S. D.; Peter, J.; Wakchaure, V. C.; Goudappagouda; Raj, K. V.; Kurungot, S.; Babu, S. S. Imidazole-Linked Crystalline Two-Dimensional Polymer with Ultrahigh Proton-Conductivity. *J. Am. Chem. Soc.* **2019**, *141* (38), 14950–14954.

(95)   Fang, Q.; Zhuang, Z.; Gu, S.; Kaspar, R. B.; Zheng, J.; Wang, J.; Qiu, S.; Yan, Y. Designed Synthesis of Large-Pore Crystalline Polyimide Covalent Organic Frameworks. *Nat. Commun.* **2014**, *5* (1), 4503.

(96)   Maschita, J.; Banerjee, T.; Lotsch, B. V. Direct and Linker-Exchange Alcohol-Assisted Hydrothermal Synthesis of Imide-Linked Covalent Organic Frameworks. *Chem. Mater.* **2022**, *34* (5), 2249–2258.

(97)   Lin, S.; Diercks, C. S.; Zhang, Y. B.; Kornienko, N.; Nichols, E. M.; Zhao, Y.; Paris, A. R.; Kim, D.; Yang, P.; Yaghi, O. M.; Chang, C. J. Covalent Organic Frameworks Comprising Cobalt Porphyrins for Catalytic CO2 Reduction in Water. *Science* **2015**, *349* (6253), 1208–1213.

(98)   Ma, X.; Scott, T. F. Approaches and Challenges in the Synthesis of Three-Dimensional Covalent-Organic Frameworks. *Commun. Chem.* **2018**, *1*, 98.

(99)   Slater, M. D.; Kim, D.; Lee, E.; Johnson, C. S. Sodium-Ion Batteries. *Adv. Funct. Mater.*

2013, *23* (8), 947–958.

(100) Abdelkader, A. A.; Norouzi, N.; Rodene, D. D.; Alzharani, A.; Gupta, R. B.; El-Kadri, H. M. Electrocatalytic Cathodes Based on Cobalt Nanoparticles Supported on Nitrogen-Doped Porous Carbon by Strong Electrostatic Adsorption for Advanced Lithium-Sulfur Batteries. *Energy and Fuels* **2020**, *34* (10), 13038–13047.

(101) Yang, X.; Li, X.; Adair, K.; Zhang, H.; Sun, X. Structural Design of Lithium–Sulfur Batteries: From Fundamental Research to Practical Application. *Electrochem. Energy Rev.* **2018**, *1*, 239‒293.

(102) Choi, K. M.; Jeong, H. M.; Park, J. H.; Zhang, Y. B.; Kang, J. K.; Yaghi, O. M. Supercapacitors of Nanocrystalline Metal-Organic Frameworks. *ACS Nano* **2014**, *8* (7), 7451–7457.

(103) Gogotsi, Y.; Penner, R. M. Energy Storage in Nanomaterials - Capacitive, Pseudocapacitive, or Battery-Like? *ACS Nano* **2018**, *12* (3), 2081–2083.

(104) Shao, Y.; El-Kady, M. F.; Sun, J.; Li, Y.; Zhang, Q.; Zhu, M.; Wang, H.; Dunn, B.; Kaner, R. B. Design and Mechanisms of Asymmetric Supercapacitors. *Chem. Rev.* **2018**, *118* (18), 9233–9280.

(105) Xie, J.; Yang, P.; Wang, Y.; Qi, T.; Lei, Y.; Li, C. M. Puzzles and Confusions in Supercapacitor and Battery: Theory and Solutions. *J. Power Sources* **2018**, *401*, 213–223.

(106) Kim, S.; Choi, H. C. Light-Promoted Synthesis of Highly-Conjugated Crystalline Covalent Organic Framework. *Commun. Chem.* **2019**, *2* (1), 60.

(107) Kim, S.; Lim, H.; Lee, J.; Choi, H. C. Synthesis of a Scalable Two-Dimensional Covalent

Organic Framework by the Photon-Assisted Imine Condensation Reaction on the Water Surface. *Langmuir* **2018**, *34* (30), 8731–8738.

(108) Kim, S.; Park, C.; Lee, M.; Song, I.; Kim, J.; Lee, M.; Jung, J.; Kim, Y.; Lim, H.; Choi, H. C. Rapid Photochemical Synthesis of Sea-Urchin-Shaped Hierarchical Porous COF-5 and Its Lithography-Free Patterned Growth. *Adv. Funct. Mater.* **2017**, *27* (32), 1700925.

(109) Talaie, E.; Bonnick, P.; Sun, X.; Pang, Q.; Liang, X.; Nazar, L. F. Methods and Protocols for Electrochemical Energy Storage Materials Research. *Chem. Mater.* **2017**, *29* (1), 90–105.

(110) Bonnick, P.; Dahn, J. R. A Simple Coin Cell Design for Testing Rechargeable Zinc-Air or Alkaline Battery Systems. *J. Electrochem. Soc.* **2012**, *159* (7), A981–A989.

(111) Chen, X.; Geng, K.; Liu, R.; Tan, K. T.; Gong, Y.; Li, Z.; Tao, S.; Jiang, Q.; Jiang, D. Covalent Organic Frameworks: Chemical Approaches to Designer Structures and Built-In Functions. *Angew. Chemie Int. Ed.* **2020**, *59* (13), 5050–5091.

(112) Wang, Z.; Zhang, S.; Chen, Y.; Zhang, Z.; Ma, S. Covalent Organic Frameworks for Separation Applications. *Chem. Soc. Rev.* **2020**, *49* (3), 708–735.

(113) Zhang, K.; Kirlikovali, K. O.; Varma, R. S.; Jin, Z.; Jang, H. W.; Farha, O. K.; Shokouhimehr, M. Covalent Organic Frameworks: Emerging Organic Solid Materials for Energy and Electrochemical Applications. *ACS Appl. Mater. Interfaces* **2020**, *12*, 27821-27852.

(114) Yusran, Y.; Fang, Q.; Valtchev, V. Electroactive Covalent Organic Frameworks: Design, Synthesis, and Applications. *Adv. Mater.* **2020**, *32* (44), 2002038.

(115) Delmas, C. Sodium and Sodium-Ion Batteries: 50 Years of Research. *Adv. Energy Mater.* **2018**, *8* (17), 1703137.

(116) Wuttke, S. Introduction to Reticular Chemistry. Metal–Organic Frameworks and Covalent Organic Frameworks By Omar M. Yaghi, Markus J. Kalmutzki, and Christian S. Diercks. *Angew. Chemie Int. Ed.* **2019**, *58* (40), 14024.

(117) Kou, Y.; Xu, Y.; Guo, Z.; Jiang, D. Supercapacitive Energy Storage and Electric Power Supply Using an Aza-Fused π-Conjugated Microporous Framework. *Angew. Chemie - Int. Ed.* **2011**, *50* (37), 8753–8757.

(118) Li, X.; Wang, H.; Chen, H.; Zheng, Q.; Zhang, Q.; Mao, H.; Liu, Y.; Cai, S.; Sun, B.; Dun, C.; Gordon, M. P.; Zheng, H.; Reimer, J. A.; Urban, J. J.; Ciston, J.; Tan, T.; Chan, E. M.; Zhang, J.; Liu, Y. Dynamic Covalent Synthesis of Crystalline Porous Graphitic Frameworks. *Chem* **2020**, *6* (4), 933–944.

(119) Verma, P.; Maire, P.; Novák, P. A Review of the Features and Analyses of the Solid Electrolyte Interphase in Li-Ion Batteries. *Electrochim. Acta* **2010**, *55* (22), 6332–6341.

(120) Shao, Y.; Gan, Z.; Epifanovsky, E.; Gilbert, A. T. B.; Wormit, M.; Kussmann, J.; Lange, A. W.; Behn, A.; Deng, J.; Feng, X.; Ghosh, D.; Goldey, M.; Horn, P. R.; Jacobson, L. D.; Kaliman, I.; Khaliullin, R. Z.; Kuš, T.; Landau, A.; Liu, J.; Proynov, E. I.; Rhee, Y. M.; Richard, R. M.; Rohrdanz, M. A.; Steele, R. P.; Sundstrom, E. J.; Woodcock, H. L.; Zimmerman, P. M.; Zuev, D.; Albrecht, B.; Alguire, E.; Austin, B.; Beran, G. J. O.; Bernard, Y. A.; Berquist, E.; Brandhorst, K.; Bravaya, K. B.; Brown, S. T.; Casanova, D.; Chang, C. M.; Chen, Y.; Chien, S. H.; Closser, K. D.; Crittenden, D. L.; Diedenhofen, M.; Distasio, R. A.; Do, H.; Dutoi, A. D.; Edgar, R. G.; Fatehi, S.; Fusti-Molnar, L.; Ghysels, A.;

Golubeva-Zadorozhnaya, A.; Gomes, J.; Hanson-Heine, M. W. D.; Harbach, P. H. P.; Hauser, A. W.; Hohenstein, E. G.; Holden, Z. C.; Jagau, T. C.; Ji, H.; Kaduk, B.; Khistyaev, K.; Kim, J.; Kim, J.; King, R. A.; Klunzinger, P.; Kosenkov, D.; Kowalczyk, T.; Krauter, C. M.; Lao, K. U.; Laurent, A. D.; Lawler, K. V.; Levchenko, S. V.; Lin, C. Y.; Liu, F.; Livshits, E.; Lochan, R. C.; Luenser, A.; Manohar, P.; Manzer, S. F.; Mao, S. P.; Mardirossian, N.; Marenich, A. V.; Maurer, S. A.; Mayhall, N. J.; Neuscamman, E.; Oana, C. M.; Olivares-Amaya, R.; Oneill, D. P.; Parkhill, J. A.; Perrine, T. M.; Peverati, R.; Prociuk, A.; Rehn, D. R.; Rosta, E.; Russ, N. J.; Sharada, S. M.; Sharma, S.; Small, D. W.; Sodt, A.; Stein, T.; Stück, D.; Su, Y. C.; Thom, A. J. W.; Tsuchimochi, T.; Vanovschi, V.; Vogt, L.; Vydrov, O.; Wang, T.; Watson, M. A.; Wenzel, J.; White, A.; Williams, C. F.; Yang, J.; Yeganeh, S.; Yost, S. R.; You, Z. Q.; Zhang, I. Y.; Zhang, X.; Zhao, Y.; Brooks, B. R.; Chan, G. K. L.; Chipman, D. M.; Cramer, C. J.; Goddard, W. A.; Gordon, M. S.; Hehre, W. J.; Klamt, A.; Schaefer, H. F.; Schmidt, M. W.; Sherrill, C. D.; Truhlar, D. G.; Warshel, A.; Xu, X.; Aspuru-Guzik, A.; Baer, R.; Bell, A. T.; Besley, N. A.; Chai, J. Da; Dreuw, A.; Dunietz, B. D.; Furlani, T. R.; Gwaltney, S. R.; Hsu, C. P.; Jung, Y.; Kong, J.; Lambrecht, D. S.; Liang, W.; Ochsenfeld, C.; Rassolov, V. A.; Slipchenko, L. V.; Subotnik, J. E.; Van Voorhis, T.; Herbert, J. M.; Krylov, A. I.; Gill, P. M. W.; Head-Gordon, M. Advances in Molecular Quantum Chemistry Contained in the Q-Chem 4 Program Package. *Mol. Phys.* **2015**, *113* (2), 184–215.

(121) Becke, A. D. Density-Functional Thermochemistry. III. The Role of Exact Exchange. *J. Chem. Phys.* **1993**, *98* (7), 5648–5652.

(122) Stephens, P. J.; Devlin, F. J.; Chabalowski, C. F.; Frisch, M. J. Ab Initio Calculation of Vibrational Absorption and Circular Dichroism Spectra Using Density Functional Force

Fields. *J. Phys. Chem.* **1994**, *98* (45), 11623–11627.

(123) Zhao, Y.; Schultz, N. E.; Truhlar, D. G. Design of Density Functionals by Combining the Method of Constraint Satisfaction with Parametrization for Thermochemistry, Thermochemical Kinetics, and Noncovalent Interactions. *J. Chem. Theory Comput.* **2006**, *2* (2), 364–382.

(124) Marenich, A. V.; Cramer, C. J.; Truhlar, D. G. Universal Solvation Model Based on Solute Electron Density and on a Continuum Model of the Solvent Defined by the Bulk Dielectric Constant and Atomic Surface Tensions. *J. Phys. Chem. B* **2009**, *113* (18), 6378–6396.

(125) Riadigos, C. F.; Iglesias, R.; Rivas, M. A.; Iglesias, T. P. Permittivity and Density of the Systems (Monoglyme, Diglyme, Triglyme, or Tetraglyme + n-Heptane) at Several Temperatures. *J. Chem. Thermodyn.* **2011**, *43* (3), 275–283.

(126) Simon, P.; Gogotsi, Y.; Dunn, B. Where Do Batteries End and Supercapacitors Begin? *Science*. **2014**, *343*, 1210–1211.

(127) Liu, X.; Wen, M.; Zhao, Y.; Dong, Y.; Fan, Q.; Kuang, Q.; Li, Q. Cheese-like Bulk Carbon with Nanoholes Prepared from Egg White as an Anode Material for Lithium and Sodium Ion Batteries. *RSC Adv.* **2016**, *6* (84), 80986–80993.

(128) Wang, S.; Wang, Q.; Shao, P.; Han, Y.; Gao, X.; Ma, L.; Yuan, S.; Ma, X.; Zhou, J.; Feng, X.; Wang, B. Exfoliation of Covalent Organic Frameworks into Few-Layer Redox-Active Nanosheets as Cathode Materials for Lithium-Ion Batteries. *J. Am. Chem. Soc.* **2017**, *139*, 4258–4261.

(129) Vitaku, E.; Gannett, C. N.; Carpenter, K. L.; Shen, L.; Abruña, H. D.; Dichtel, W. R.

Phenazine-Based Covalent Organic Framework Cathode Materials with High Energy and Power Densities. *J. Am. Chem. Soc.* **2020**, *142* (1), 16–20.

(130) Ovejas, V. J.; Cuadras, A. Effects of Cycling on Lithium-Ion Battery Hysteresis and Overvoltage. *Sci. Rep.* **2019**, *9* (1), 14875.

(131) Susi, T.; Pichler, T.; Ayala, P. X-Ray Photoelectron Spectroscopy of Graphitic Carbon Nanomaterials Doped with Heteroatoms. *Beilstein J. Nanotechnol.* **2015**, *6* (1), 177–192.

(132) Brisson, P. Y.; Darmstadt, H.; Fafard, M.; Adnot, A.; Servant, G.; Soucy, G. X-Ray Photoelectron Spectroscopy Study of Sodium Reactions in Carbon Cathode Blocks of Aluminium Oxide Reduction Cells. *Carbon N. Y.* **2006**, *44* (8), 1438–1447.

(133) Jawhari, T.; Roid, A.; Casado, J. Raman Spectroscopic Characterization of Some Commercially Available Carbon Black Materials. *Carbon N. Y.* **1995**, *33* (11), 1561–1565.

(134) Lyu, Y.; Liu, Y.; Yu, Z.-E.; Su, N.; Liu, Y.; Li, W.; Li, Q.; Guo, B.; Liu, B. Recent Advances in High Energy-Density Cathode Materials for Sodium-Ion Batteries. *Sustain. Mater. Technol.* **2019**, *21*, No. e00098.

(135) Yin, X.; Sarkar, S.; Shi, S.; Huang, Q.-A.; Zhao, H.; Yan, L.; Zhao, Y.; Zhang, J. Recent Progress in Advanced Organic Electrode Materials for Sodium-Ion Batteries: Synthesis, Mechanisms, Challenges and Perspectives. *Adv. Funct. Mater.* **2020**, *30* (11), 1908445.

(136) Zhao, Q.; Lu, Y.; Chen, J. Advanced Organic Electrode Materials for Rechargeable Sodium-Ion Batteries. *Adv. Energy Mater.* **2017**, *7* (8), 1601792.

(137) Waller, P. J.; Gándara, F.; Yaghi, O. M. Chemistry of Covalent Organic Frameworks. *Acc. Chem. Res.* **2015**, *48* (12), 3053–3063.

(138) Evans, A. M.; Strauss, M. J.; Corcos, A. R.; Hirani, Z.; Ji, W.; Hamachi, L. S.; Aguilar-Enriquez, X.; Chavez, A. D.; Smith, B. J.; Dichtel, W. R. Two-Dimensional Polymers and Polymerizations. *Chem. Rev.* **2022**, *122* (1), 442–564.

(139) Yang, X.; Gong, L.; Liu, X.; Zhang, P.; Li, B.; Qi, D.; Wang, K.; He, F.; Jiang, J. Mesoporous Polyimide-Linked Covalent Organic Framework with Multiple Redox-Active Sites for High-Performance Cathodic Li Storage. *Angew. Chemie - Int. Ed.* **2022**, *61* (31), No. e202207043.

(140) Liu, W.; Gong, L.; Liu, Z.; Jin, Y.; Pan, H.; Yang, X.; Yu, B.; Li, N.; Qi, D.; Wang, K.; Wang, H.; Jiang, J. Conjugated Three-Dimensional High-Connected Covalent Organic Frameworks for Lithium-Sulfur Batteries. *J. Am. Chem. Soc.* **2022**, *144* (37), 17209–17218.

(141) Kandambeth, S.; Jia, J.; Wu, H.; Kale, V. S.; Parvatkar, P. T.; Czaban-Jóźwiak, J.; Zhou, S.; Xu, X.; Ameur, Z. O.; Abou-Hamad, E.; Emwas, A. H.; Shekhah, O.; Alshareef, H. N.; Eddaoudi, M. Covalent Organic Frameworks as Negative Electrodes for High-Performance Asymmetric Supercapacitors. *Adv. Energy Mater.* **2020**, *10* (38), 2001673.

(142) Ding, H.; Mal, A.; Wang, C. Energy Storage in Covalent Organic Frameworks: From Design Principles to Device Integration. *Chem. Res. Chinese Univ.* **2022**, *38* (2), 356–363.

(143) Qian, C.; Qi, Q. Y.; Jiang, G. F.; Cui, F. Z.; Tian, Y.; Zhao, X. Toward Covalent Organic Frameworks Bearing Three Different Kinds of Pores: The Strategy for Construction and COF-to-COF Transformation via Heterogeneous Linker Exchange. *J. Am. Chem. Soc.* **2017**, *139* (19), 6736–6743.

(144) Zhang, G.; Tsujimoto, M.; Packwood, D.; Duong, N. T.; Nishiyama, Y.; Kadota, K.; Kitagawa, S.; Horike, S. Construction of a Hierarchical Architecture of Covalent Organic

Frameworks via a Postsynthetic Approach. *J. Am. Chem. Soc.* **2018**, *140* (7), 2602–2609.

(145) Waller, P. J.; Alfaraj, Y. S.; Diercks, C. S.; Jarenwattananon, N. N.; Yaghi, O. M. Conversion of Imine to Oxazole and Thiazole Linkages in Covalent Organic Frameworks. *J. Am. Chem. Soc.* **2018**, *140* (29), 9099–9103.

(146) Zhai, Y.; Liu, G.; Jin, F.; Zhang, Y.; Gong, X.; Miao, Z.; Li, J.; Zhang, M.; Cui, Y.; Zhang, L.; Liu, Y.; Zhang, H.; Zhao, Y.; Zeng, Y. Construction of Covalent-Organic Frameworks (COFs) from Amorphous Covalent Organic Polymers via Linkage Replacement. *Angew. Chemie - Int. Ed.* **2019**, *58* (49), 17679–17683.

(147) Miao, Z.; Liu, G.; Cui, Y.; Liu, Z.; Li, J.; Han, F.; Liu, Y.; Sun, X.; Gong, X.; Zhai, Y.; Zhao, Y.; Zeng, Y. A Novel Strategy for the Construction of Covalent Organic Frameworks from Nonporous Covalent Organic Polymers. *Angew. Chemie* **2019**, *131* (15), 4960–4964.

(148) Li, Z.; Ding, X.; Feng, Y.; Feng, W.; Han, B. H. Structural and Dimensional Transformations between Covalent Organic Frameworks via Linker Exchange. *Macromolecules* **2019**, *52* (3), 1257–1265.

(149) Gao, H.; Neale, A. R.; Zhu, Q.; Bahri, M.; Wang, X.; Yang, H.; Xu, Y.; Clowes, R.; Browning, N. D.; Little, M. A.; Hardwick, L. J.; Cooper, A. I. A Pyrene-4,5,9,10-Tetraone-Based Covalent Organic Framework Delivers High Specific Capacity as a Li-Ion Positive Electrode. *J. Am. Chem. Soc.* **2022**, *144* (21), 9434–9442.

(150) Luo, Z.; Liu, L.; Ning, J.; Lei, K.; Lu, Y.; Li, F.; Chen, J. A Microporous Covalent–Organic Framework with Abundant Accessible Carbonyl Groups for Lithium-Ion Batteries. *Angew. Chemie - Int. Ed.* **2018**, *57* (30), 9443–9446.

(151) Wang, A.; Tan, R.; Breakwell, C.; Wei, X.; Fan, Z.; Ye, C.; Malpass-Evans, R.; Liu, T.; Zwijnenburg, M. A.; Jelfs, K. E.; McKeown, N. B.; Chen, J.; Song, Q. Solution-Processable Redox-Active Polymers of Intrinsic Microporosity for Electrochemical Energy Storage. *J. Am. Chem. Soc.* **2022**, *144* (37), 17198–17208.

(152) Bell, V. L.; Aeronautics, N.; Gager, H. Polymers from Isomeric Diamines. **1976**, *14,* 2275–2291.

(153) Duan, H.; Lyu, P.; Liu, J.; Zhao, Y.; Xu, Y. Semiconducting Crystalline Two-Dimensional Polyimide Nanosheets with Superior Sodium Storage Properties. *ACS Nano* **2019**, *13* (2), 2473–2480.

(154) Wang, Z.; Li, Y.; Liu, P.; Qi, Q.; Zhang, F.; Lu, G.; Zhao, X.; Huang, X. Few Layer Covalent Organic Frameworks with Graphene Sheets as Cathode Materials for Lithium-Ion Batteries. *Nanoscale* **2019**, *11* (12), 5330–5335.

(155) Dai, Z.; Mani, U.; Tan, H. T.; Yan, Q. Advanced Cathode Materials for Sodium-Ion Batteries: What Determines Our Choices? *Small Methods* **2017**, *1* (5), 1700098.

(156) Hwang, J. Y.; Myung, S. T.; Sun, Y. K. Sodium-Ion Batteries: Present and Future. *Chem. Soc. Rev.* **2017**, *46*, 3529–3614.

(157) Alzharani, A.; Shehab, M.; Rodene, D.; Ahmed, J.; BAKRY, A.; Kaid, M.; El-Kaderi, H. Surface Modification of Partially Reduced Graphene Oxide for Advanced Electrode Material in Rechargeable Sodium Batteries. *Energy Fuels* **2022**, *36*, 4967–4977.

(158) Auras, F.; Ascherl, L.; Hakimioun, A. H.; Margraf, J. T.; Hanusch, F. C.; Reuter, S.; Bessinger, D.; Döblinger, M.; Hettstedt, C.; Karaghiosoff, K.; Herbert, S.; Knochel, P.;

Clark, T.; Bein, T. Synchronized Offset Stacking: A Concept for Growing Large-Domain and Highly Crystalline 2D Covalent Organic Frameworks. *J. Am. Chem. Soc.* **2016**, *138* (51), 16703–16710.

(159) Jin, S.; Sakurai, T.; Kowalczyk, T.; Dalapati, S.; Xu, F.; Wei, H.; Chen, X.; Gao, J.; Seki, S.; Irle, S.; Jiang, D. Two-Dimensional Tetrathiafulvalene Covalent Organic Frameworks: Towards Latticed Conductive Organic Salts. *Chem. - A Eur. J.* **2014**, *20* (45), 14608–14613.

(160) Meng, Y.; Lin, G.; Ding, H.; Liao, H.; Wang, C. Impregnation of Sulfur into a 2D Pyrene-Based Covalent Organic Framework for High-Rate Lithium-Sulfur Batteries. *J. Mater. Chem. A* **2018**, *6* (35), 17186–17191.

(161) Chen, X.; Huang, N.; Gao, J.; Xu, H.; Xu, F.; Jiang, D. Towards Covalent Organic Frameworks with Predesignable and Aligned Open Docking Sites. *Chem. Commun.* **2014**, *50* (46), 6161–6163.

(162) Gu, S.; Ma, X.; Chen, J.; Hao, R.; Wang, Z.; Qin, N.; Zheng, W.; Gan, Q.; Luo, W.; Li, M.; Li, Z.; Liao, K.; Guo, H.; Liu, G.; Zhang, K.; Lu, Z. Regulating the Radical Intermediates by Conjugated Units in Covalent Organic Frameworks for Optimized Lithium Ion Storage. *J. Energy Chem.* **2022**, *69*, 428–433.

(163) Li, H.; Brédas, J. L. Nanoscrolls Formed from Two-Dimensional Covalent Organic Frameworks. *Chem. Mater.* **2019**, *31* (9), 3265–3273.

(164) Viculis, L. M.; Mack, J. J.; Kaner, R. B. A Chemical Route to Carbon Nanoscrolls. *Science.* **2003**, *299* (5611), 1361.

(165) Gor, G. Y.; Huber, P.; Bernstein, N. Adsorption-Induced Deformation of Nanoporous

Materials - a Review. *Appl. Phys. Rev.* **2017**, *4* (1), 011303.

(166) Chen, Y.; Shi, Z. L.; Wei, L.; Zhou, B.; Tan, J.; Zhou, H. L.; Zhang, Y. B. Guest-Dependent Dynamics in a 3D Covalent Organic Framework. *J. Am. Chem. Soc.* **2019**, *141* (7), 3298–3303.

(167) Yang, D. H.; Yao, Z. Q.; Wu, D.; Zhang, Y. H.; Zhou, Z.; Bu, X. H. Structure-Modulated Crystalline Covalent Organic Frameworks as High-Rate Cathodes for Li-Ion Batteries. *J. Mater. Chem. A* **2016**, *4* (47), 18621–18627.

(168) Yan, Y.; Hao, B.; Wang, D.; Chen, G.; Markweg, E.; Albrecht, A.; Schaaf, P. Understanding the Fast Lithium Storage Performance of Hydrogenated TiO2 Nanoparticles. *J. Mater. Chem. A* **2013**, *1* (46), 14507–14513.

(169) Le, Z.; Liu, F.; Nie, P.; Li, X.; Liu, X.; Bian, Z.; Chen, G.; Bin Wu, H.; Lu, Y. Pseudocapacitive Sodium Storage in Mesoporous Single-Crystal-like TiO2 − Graphene Nanocomposite Enables High-Performance Sodium-Ion Capacitors. *ACS Nano* **2017**, *11*, 2952–2960.

(170) Han, X.; Chang, C.; Yuan, L.; Sun, T.; Sun, J. Aromatic Carbonyl Derivative Polymers as High-Performance Li-Ion Storage Materials. *Adv. Mater.* **2007**, *19* (12), 1616–1621.

(171) Huang, Q.; Loveridge, M. J.; Genieser, R.; Lain, M. J.; Bhagat, R. Electrochemical Evaluation and Phase-Related Impedance Studies on Silicon-Few Layer Graphene (FLG) Composite Electrode Systems. *Sci. Rep.* **2018**, *8* (1), 1386.

(172) Samyn, P.; Schoukens, G.; Verpoort, F.; Van Craenenbroeck, J.; De Baets, P. Friction and Wear Mechanisms of Sintered and Thermoplastic Polyimides under Adhesive Sliding.

Macromol. Mater. Eng. **2007**, *292* (5), 523–556.

(173) Das, S. K.; Roy, S.; Das, A.; Chowdhury, A.; Chatterjee, N.; Bhaumik, A. A Conjugated 2D Covalent Organic Framework as a Drug Delivery Vehicle towards Triple Negative Breast Cancer Malignancy. *Nanoscale Adv.* **2022**, 2313–2320.

(174) Yusran, Y.; Li, H.; Guan, X.; Fang, Q.; Qiu, S. Covalent Organic Frameworks for Catalysis. *EnergyChem* **2020**, *2* (3), 100035.

(175) Jin, S.; Allam, O.; Jang, S. S.; Lee, S. W. Covalent Organic Frameworks: Design and Applications in Electrochemical Energy Storage Devices. *InfoMat* **2022**, *4* (6), 1–35.

(176) Cao, Y.; Wang, M.; Wang, H.; Han, C.; Pan, F.; Sun, J. Covalent Organic Framework for Rechargeable Batteries: Mechanisms and Properties of Ionic Conduction. *Adv. Energy Mater.* **2022**, *12* (20), 2200057.

(177) An, Y.; Tan, S.; Liu, Y.; Zhu, K.; Hu, L.; Rong, Y.; An, Q. Designs and Applications of Multi-Functional Covalent Organic Frameworks in Rechargeable Batteries. *Energy Storage Mater.* **2021**, *41*, 354–379.

(178) Hu, Y.; Dunlap, N.; Wan, S.; Lu, S.; Huang, S.; Sellinger, I.; Ortiz, M.; Jin, Y.; Lee, S. H.; Zhang, W. Crystalline Lithium Imidazolate Covalent Organic Frameworks with High Li-Ion Conductivity. *J. Am. Chem. Soc.* **2019**, *141* (18), 7518–7525.

(179) Dunn, B.; Kamath, H.; Tarascon, J.-M. Electrical Energy Storage for the Grid: A Battery of Choices System Power Ratings, Module Size. *Science*, **2011**, *334* (6058), 928–935.

(180) Parker, J. F.; Chervin, C. N.; Pala, I. R.; Machler, M.; Burz, M. F.; Long, J. W.; Rolison, D. R. Rechargeable Nickel-3D Zinc Batteries: An Energy-Dense, Safer Alternative to Lithium-

Ion. *Science* **2017**, *356* (6336), 415–418.

(181) Zhao, J.; Zhou, M.; Chen, J.; Tao, L.; Zhang, Q.; Li, Z.; Zhong, S.; Fu, H.; Wang, H.; Wu, L. Phthalocyanine-Based Covalent Organic Frameworks as Novel Anode Materials for High-Performance Lithium-Ion/Sodium-Ion Batteries. *Chem. Eng. J.* **2021**, *425*, 131630.

(182) Van Der Jagt, R.; Vasileiadis, A.; Veldhuizen, H.; Shao, P.; Feng, X.; Ganapathy, S.; Habisreutinger, N. C.; Van Der Veen, M. A.; Wang, C.; Wagemaker, M.; Van Der Zwaag, S.; Nagai, A. Synthesis and Structure-Property Relationships of Polyimide Covalent Organic Frameworks for Carbon Dioxide Capture and (Aqueous) Sodium-Ion Batteries. *Chem. Mater.* **2021**, *33* (3), 818–833.

(183) Zhang, Q.; Wei, H.; Wang, L.; Wang, J.; Fan, L.; Ding, H.; Lei, J.; Yu, X.; Lu, B. Accessible COF-Based Functional Materials for Potassium-Ion Batteries and Aluminum Batteries. *ACS Appl. Mater. Interfaces* **2019**, *11* (47), 44352–44359.

(184) Yang, X.; Gong, L.; Wang, K.; Ma, S.; Liu, W.; Li, B.; Li, N.; Pan, H.; Chen, X.; Wang, H.; Liu, J.; Jiang, J. Ionothermal Synthesis of Fully Conjugated Covalent Organic Frameworks for High-Capacity and Ultra-stable Potassium-Ion Battery. *Adv. Mater.* **2022**, *34,* 2207245.

(185) Sun, R.; Hou, S.; Luo, C.; Ji, X.; Wang, L.; Mai, L.; Wang, C. A Covalent Organic Framework for Fast-Charge and Durable Rechargeable Mg Storage. *Nano Lett.* **2020**, *20* (5), 3880–3888.

(186) Shi, Y.; Peng, L.; Ding, Y.; Zhao, Y.; Yu, G. Nanostructured Conductive Polymers for Advanced Energy Storage. *Chem. Soc. Rev.* **2015**, *44* (19), 6684–6696.

(187) Chen, J. M.; Duan, H.; Kong, Y.; Tian, B.; Ning, G. H.; Li, D. Improving Lithium-Sulfur Batteries' Performance via Inverse Vulcanization of Vinylene-Linked Covalent Organic Frameworks. *Energy and Fuels* **2022**, *36* (11), 5998–6004.

(188) Mi, Z.; Yang, P.; Wang, R.; Unruangsri, J.; Yang, W.; Wang, C.; Guo, J. Stable Radical Cation-Containing Covalent Organic Frameworks Exhibiting Remarkable Structure-Enhanced Photothermal Conversion. *J. Am. Chem. Soc.* **2019**, *141* (36), 14433–14442.

(189) Yaghi, O. M.; Kalmutzki, M. J.; Diercks, C. S. Introduction to Reticular Chemistry Metal Organic Frameworks and Covalent Organic. Wiley-VCH: Weinheim, 2019.

(190) Shang, X.; Li, X.; Xi, N.; Zhai, Y.; Zhang, J.; Xu, X. Theory and Experiment: Recognition Properties of Chemosensor Containing Ruthenium(II) System in Water Solution. *Sensors Actuators, B Chem.* **2011**, *160* (1), 1112–1119.

(191) Shang, X. F.; Lin, H.; Lin, H. K. The Synthesis and Recognition Properties of Colorimetric Fluoride Receptors Bearing Sulfonamide. *J. Fluor. Chem.* **2007**, *128* (5), 530–534.

(192) Kleineweischede, A.; Mattay, J. Synthesis of Amino- and Bis(Bromomethyl)-Substitued Bi- and Tetradentate N-Heteroaromatic Ligands: Building Blocks for Pyrazino-Functionalized Fullerene Dyads. *European J. Org. Chem.* **2006**, No. 4, 947–957.

(193) Skujins, S.; Webb, G. A. Spectroscopic and Structural Studies of Some Oxocarbon Condensation Products—III. *Tetrahedron* **1969**, *25* (17), 3955–3960.

(194) Kim, S. Synthesis of Dimensional Organic Networks as Energy Materials. *Graduate School of UNIST*, **2019**, 1–112.

(195) Zhang, X.; Lu, J.; Zhang, J. Porosity Enhancement of Carbazolic Porous Organic

Frameworks Using Dendritic Building Blocks for Gas Storage and Separation. *Chem. Mater.* **2014**, *26* (13), 4023–4029.

(196) Patel, H. A.; Yavuz, C. T. Noninvasive Functionalization of Polymers of Intrinsic Microporosity for Enhanced CO2capture. *Chem. Commun.* **2012**, *48* (80), 9989–9991.

(197) Winter, M.; Brodd, R. J. What Are Batteries, Fuel Cells, and Supercapacitors? *Chem. Rev.* **2004**, *104* (10), 4245–4269.

(198) Eftekhari, A.; Fan, Z. Ordered Mesoporous Carbon and Its Applications for Electrochemical Energy Storage and Conversion. *Mater. Chem. Front.* **2017**, *1* (6), 1001–1027.